UNIVERSITAT POLITÈCNICA DE CATALUNYA
BARCELONATECH

Escola Superior d'Enginyeries Industrial, Aeroespacial i Audiovisual de Terrassa

DEGREE:

Master's degree in Aerospace Engineering (Màster universitari en Enginyeria Aeronàutica)

STUDENT:

Jordi Luque Barcons

TITLE OF THE THESIS:

Symmetry-preserving discretization of the incompressible form of the Navier-Stokes equations under turbulent conditions. LES simulation of a turbulent channel flow

DIRECTOR:

Carlos-David Pérez-Segarra

CO-DIRECTOR:

Francesc-Xavier Trias

CALL:

Fall 2021

Content of the document - **REPORT**

Contents

List of Figures

List of Tables

List of Algorithms

Honor declaration

I declare that,

The work in this Master's Thesis is completely my own work. No part of this Thesis is taken from other people's work without giving them credit. All references have been clearly cited.

I am authorised to make use of the information provided by the "Centre Tecnològic de Transferència de Calor" (CTTC).

I understand that an infringement of this declaration leaves me subject to the foreseen disciplinary actions by the "Universitat Politècnica de Catalunya - Barcelona TECH".

Luque Barcons, Jordi, 28^{th} September 2021

Title of the thesis: Symmetry-preserving discretization of the incompressible form of the Navier-Stokes equations under turbulent conditions. LES simulation of a turbulent channel flow

Abstract

The incompressible form of the Navier-Stokes equations (conservation of mass, momentum and energy) is solved by applying a second-order symmetry-preserving spatial discretization which allows to preserve the symmetry of the operators. The physics behind turbulent flows and how those can be modelled is studied, considering both the RANS equations and the LES model. The Taylor-Green vortex problem is solved with no model and compared with the results of van Rees et al. [4], obtaining very good agreement regarding the time evolution of the volume-averaged kinetic energy, but higher discrepancies in the time evolution of the kinetic energy dissipation rate. Additionally, DNS results for a turbulent channel flow at $Re_\tau = 180$ are obtained with coarse meshes. The same problem is also solved by applying the Smagorinsky, S3PR and Vreman's LES models. DNS results obtained with a 32^3 mesh show relatively good agreement with the reference results of Moser et al. [5], while LES simulations employing the S3PR and Vreman's model allow to improve the results in the buffer-layer region.

1 Introduction

1.1 Aim of the thesis

The aim of this thesis is the elaboration, validation and verification of C++ codes and the necessary tools that allow to solve the incompressible form of the Navier-Stokes equations under turbulent regime. The objective is to understand the physics behind turbulent flows and how those can be modelled by applying a symmetry-preserving discretization of the equations, which will be properly verified too. Additionally, different LES models to tackle the turbulence closure problem must be programmed and applied to relatively coarse meshes. The comparison with different turbulence models will be assessed by solving the well-known benchmark problem of the turbulent channel flow.

1.2 Background and Justification

Computational fluid dynamics (CFD), has become an essential tool for the industrial and aerospace industries, as it allows to model and analyse a wide variety of problems that involve fluid flows, heat transfer and chemical reactions. CFD was integrated by the aerospace industry during the 1960s. However, it was not until the 90s when the availability of much more economically-affordable high-performance computers and the improvements on the interfaces of the CFD codes; allowed CFD codes to enter into other industrial sectors and fields, such as aerodynamics, hydrodynamics, turbomachinery design, chemical process engineering, external and internal environment of buildings, hydrology and oceanography, meteorology, biomedicine,... [6] With the reduction in the relative computation cost over the years, the majority of the preliminary designs of the aerospace industry are carried-out through CFD, while wind tunnel testing is only used to fine-tune the final design, which allows to decrease the overall costs during the design stage. Moreover, CFD allows to visualise and study detailed flow-field structures that are very difficult to capture through wind tunnel tests.

Nevertheless, there are important drawbacks that need to be addressed when considering the use of computational fluid dynamics. Numerous sources of errors are present when using CFD. Incorrect domain dimensions and inadequate grid designs are important sources of errors which are usually problem-dependent and can only be eliminated by performing a grid dependence study, which increases the time and cost of the overall study. Due to the equations being discretised in space and time, three major sources of numerical errors arise [6]:

- **Roundoff errors:** Those errors appear due to the representation of real numbers with a finite number of significant digits (i.e, the machine accuracy). These errors can be controlled by carefully arranging floating-point arithmetic operations, avoiding subtraction of very similar size numbers, or addition of numbers of very different size.
- **Iterative convergence errors:** Which appear due to the fact that the iteration sequence of computations is stopped when the solution is sufficiently close to the final one.
- **Discretisation errors:** Errors that appear in the temporal and spatial derivatives in the rates of change, fluxes, sources and sink terms when those are approximated from discrete values. Those can be minimised either by refining the mesh used (which increases considerably the computation time) or by using higher-order schemes.

Another group of uncertainties or errors are the input uncertainties, which are those associated with the differences that exist between the real fluid and the fluid characteristics defined for the CFD simulation. This could be further classified into:

- **Domain geometry:** Differences between the CAD model used for the simulation and the real geometry. Those differences could be due to differences in the surface roughness, manufacturing tolerances of the real object,...
- **Boundary conditions:** It is the contribution which is associated to the uncertainties introduced in the process of defining the boundary conditions, which might only be approximately true.
- **Fluid properties:** Differences between the fluid properties considered, which are usually assumed to be constant, and the real ones, which depend to a greater or less extend on the local value of the parameters of the flow.

Another set of uncertainties are introduced when semi-empirical submodels are needed to simulate more complex flow phenomena such as combustion or turbulence. Those models usually contain adjustable constants that are empirically derived for certain cases, and those constants are then extrapolated beyond the range of the experiments and used for other flow configurations, introducing an error.

Finally, and perhaps the biggest drawback of CFD, is the fact that the computational cost of a DNS simulation of turbulent flows grows with the Reynolds number to Re^3. This implies that a direct numerical simulation of the flow over an Airbus A380, whose Reynolds number is about $Re = 10^8$, has a computational complexity of about 10^{24} operations. Considering the main super computer of the Barcelona Supercomputing Center, the *Marenostrum 4*, with a speed of 13.9 petaFLOPS [8], the simulation would have a complexity of about $7.2 \cdot 10^7 s \approx 2.3$ years. As it can be seen, this computation time is not feasible for a real engineering case, which means that DNS simulations can only be performed, in practice, for very low Reynolds numbers cases. Consequently, turbulence modelling is a must for reducing computation time when the Reynolds number increases. For real practice engineering problems, average flow quantities are usually enough for design purposes, and thus, RANS equations are widely used, commonly through eddy viscosity models. However, with the improvement in performance of nowadays computers, Large Eddy Simulation (LES) is becoming more popular, as it allows to obtain time-dependent flow properties in contrast with RANS models.

1.3 Scope

The scope of the thesis is to get a better understanding of turbulent flows, the physics behind them and how they can be studied from a physical and statistical point of view. The aim is the development of a 3D staggered CFD code with a symmetry-preserving discretisation, and based on a classical Fractional Step projection method, that can be used to simulate simple 3D flows. To get a better insight into the turbulence phenomena, different LES models based on the eddy viscosity assumption are programmed and compared.

1.4 Requirements

The basic requirements to properly develop the thesis are the development of the $C++$ codes and all the other necessary tools to solve the incompressible form of the Navier-Stokes equations (conservation of mass, momentum and energy), by applying a symmetry-preserving spatial discretization. The postprocess of all the computations is done with *Paraview* and *Matlab*, in order to get the plots and graphs to proof the proper functioning of the developed codes.

2 Previous study

2.1 The Navier-Stokes equations

The Navier-Stokes equations are a set of coupled non-linear partial differential equations that describe the motion of a fluid. These set of equations are formed by one time-dependent conservation of mass equation, three time-dependent conservation of momentum equations, one for each velocity component in the x, y and z directions, and an additional time-dependent conservation of energy equation. The wanted unknowns of these equations are typically the three velocity components (u, v and w), the thermodynamic pressure p and the temperature T. However, other unknowns are also involved in the equations, such as the density ρ, the enthalpy h (or internal energy u), the fluid viscosity μ and the thermal conductivity k. Consequently, a total number of 9 unknowns are usually present, meaning that four extra state relations are needed [9].

2.1.1 Conservation of mass

The equation of mass can be written, in tensorial form, as:

$$\frac{\partial \rho}{\partial t} + \frac{\partial (\rho u_i)}{\partial x_i} = 0 \tag{2.1}$$

Or written in vector form:

$$\frac{\partial \rho}{\partial t} + \nabla \cdot (\rho \mathbf{v}) = 0 \tag{2.2}$$

The previous expression can be written as:

$$\frac{\partial \rho}{\partial t} + \rho \nabla \cdot \mathbf{v} + \mathbf{v} \cdot \nabla \rho = 0 \rightarrow \frac{D\rho}{Dt} + \rho \nabla \cdot \mathbf{v} = 0 \tag{2.3}$$

It can clearly be seen that, if the flow is incompressible, the previous expression reduces to:

$$\nabla \cdot \mathbf{v} = 0 \tag{2.4}$$

2.1.2 Conservation of momentum

The conservation of momentum equation is simply Newton's second law, which expresses the proportionality between the applied force per unit volume on a fluid particle and the resulting acceleration per unit volume of the fluid element:

$$\rho \frac{D\mathbf{v}}{Dt} = \mathbf{f_{body}} + \mathbf{f_{surface}} \tag{2.5}$$

It is important to note that an Eulerian description has been used to express the acceleration term through the material derivative of the velocity. Additionally, it must be mentioned that, even though the density appears outside the derivative, it has not been assumed constant density. It is just the result of considering the conservation of mass equation. Moreover, the force term has been divided into a body force term ($\mathbf{f_{body}}$) and a surface force term ($\mathbf{f_{surface}}$), both per unit of volume. The latter are the stresses applied on the sides of the fluid element, which can

be represented by a symmetric stress tensor. Substituting those into the previous expression one gets:

$$\rho \frac{D\mathbf{v}}{Dt} = \nabla \cdot \boldsymbol{\sigma} + \mathbf{f_{body}} \tag{2.6}$$

The stress terms can be expressed using a deformation-rate law, such as the one for a Newtonian fluid.

2.1.2.1 Deformation law for a Newtonian fluid

The simplest model for the viscous stresses is a linear variation of those with the strain rate. Stokes (1845) proposed three main considerations regarding this stress law, which is satisfied by all gases and most common fluids [9]:

1. The fluid is a continuous medium. Its stress tensor σ_{ij} is a linear function of the strain rates ϵ_{ij}
2. The fluid is isotropic
3. When the strain rates are zero (i.e, the fluid is at rest), the deformation law must reduce to the hydrostatic pressure condition, $\sigma_{ij} = -p\delta_{ij}$

If the principal axes are chosen to express the deformation law, which are the same axes for the stresses and for the strain-rate tensors according to condition 2, the deformation law would read:

$$\begin{pmatrix} \sigma_{11} \\ \sigma_{22} \\ \sigma_{33} \end{pmatrix} = \begin{pmatrix} -p & 0 & 0 \\ 0 & -p & 0 \\ 0 & 0 & -p \end{pmatrix} + \begin{pmatrix} a_1 & a_2 & a_3 \\ b_1 & b_2 & b_3 \\ c_1 & c_2 & c_3 \end{pmatrix} \begin{pmatrix} \epsilon_{11} \\ \epsilon_{22} \\ \epsilon_{33} \end{pmatrix} \tag{2.7}$$

In which the terms $-p$ in the first diagonal matrix have been added to satisfy the hydrostatic condition. However to satisfy fluid isotropy the coefficients a_2 and a_3 must be equal. In a similar manner, $b_1 = b_3$ and $c_1 = c_2$. Additionally, the diagonal terms must also be equal, which means that $a_1 = b_2 = c_3$, and the matrix must be symmetric. This means that equation 2.7 can be written as:

$$\begin{pmatrix} \sigma_{11} \\ \sigma_{22} \\ \sigma_{33} \end{pmatrix} = \begin{pmatrix} -p & 0 & 0 \\ 0 & -p & 0 \\ 0 & 0 & -p \end{pmatrix} + \begin{pmatrix} k & a_1 & a_1 \\ a_1 & k & a_1 \\ a_1 & a_1 & k \end{pmatrix} \begin{pmatrix} \epsilon_{11} \\ \epsilon_{22} \\ \epsilon_{33} \end{pmatrix} \tag{2.8}$$

However, if stresses are expressed according to some arbitrary axes x, y and z and not with respect to the principal axes x_1, y_1 and z_1, a transformation law is required. Let the x axis have direction cosines l_1, m_1 and n_1, the y axis have direction cosines l_2, m_2 and n_2, and the z axis have direction cosines l_3, m_3 and n_3. According to those direction cosines, the transformation rule between the stresses in the principal axes reference frame and an arbitrary set of axes reads:

$$\begin{pmatrix} \sigma_{xx} & \sigma_{xy} & \sigma_{xz} \\ \sigma_{yx} & \sigma_{yy} & \sigma_{yz} \\ \sigma_{zx} & \sigma_{zy} & \sigma_{zz} \end{pmatrix} = \begin{pmatrix} l_1 & m_1 & n_1 \\ l_2 & m_2 & n_2 \\ l_3 & m_3 & n_3 \end{pmatrix} \begin{pmatrix} \sigma_{11} & 0 & 0 \\ 0 & \sigma_{22} & 0 \\ 0 & 0 & \sigma_{33} \end{pmatrix} \begin{pmatrix} l_1 & l_2 & l_3 \\ m_1 & m_2 & m_3 \\ n_1 & n_2 & n_3 \end{pmatrix} \tag{2.9}$$

And the same transformation can be applied to the strain rates:

$$\begin{pmatrix} \epsilon_{xx} & \epsilon_{xy} & \epsilon_{xz} \\ \epsilon_{yx} & \epsilon_{yy} & \epsilon_{yz} \\ \epsilon_{zx} & \epsilon_{zy} & \epsilon_{zz} \end{pmatrix} = \begin{pmatrix} l_1 & m_1 & n_1 \\ l_2 & m_2 & n_2 \\ l_3 & m_3 & n_3 \end{pmatrix} \begin{pmatrix} \epsilon_{11} & 0 & 0 \\ 0 & \epsilon_{22} & 0 \\ 0 & 0 & \epsilon_{33} \end{pmatrix} \begin{pmatrix} l_1 & l_2 & l_3 \\ m_1 & m_2 & m_3 \\ n_1 & n_2 & n_3 \end{pmatrix} \tag{2.10}$$

σ_{11}, σ_{22} and σ_{33} can be eliminated from 2.9 by using the principal axis deformation law 2.8, equations 2.10 and the fact that $l_i^2 + m_i^2 + n_i^2 = 1$, leading to:

$$\begin{pmatrix} \sigma_{xx} & \sigma_{xy} & \sigma_{xz} \\ \sigma_{yx} & \sigma_{yy} & \sigma_{yz} \\ \sigma_{zx} & \sigma_{zy} & \sigma_{zz} \end{pmatrix} = \begin{pmatrix} -p & 0 & 0 \\ 0 & -p & 0 \\ 0 & 0 & -p \end{pmatrix} + K \begin{pmatrix} \epsilon_{xx} & \epsilon_{xy} & \epsilon_{xz} \\ \epsilon_{yx} & \epsilon_{yy} & \epsilon_{yz} \\ \epsilon_{zx} & \epsilon_{zy} & \epsilon_{zz} \end{pmatrix} + a_1 \begin{pmatrix} div\mathbf{v} & 0 & 0 \\ 0 & div\mathbf{v} & 0 \\ 0 & 0 & div\mathbf{v} \end{pmatrix} \tag{2.11}$$

Where $K = k - a_1$. The coefficients K and a_1 can be empirically found by comparing the previous expression with the shear flow between parallel plates. It is then observed that the linear coefficient K is equal to twice the ordinary coefficient of viscosity $K = 2\mu$, while the coefficient a_1 is independent of μ and it is typically called the second coefficient of viscosity, and called Lamé's coefficient in linear elasticity or the coefficient of bulk's viscosity λ.

Equation 2.11 can be rewritten in a single deformation law as:

$$\sigma_{ij} = -p\delta_{ij} + \tau_{ij} = -p\delta_{ij} + \mu \left(\frac{\partial u_i}{\partial x_j} + \frac{\partial u_j}{\partial x_i} \right) + \delta_{ij}\lambda div\mathbf{v} \tag{2.12}$$

Where $\tau_{ij} = \mu \left(\frac{\partial u_i}{\partial x_j} + \frac{\partial u_j}{\partial x_i} \right) + \delta_{ij}\lambda div\mathbf{v}$ is the deviatoric part of the stress tensor. It is important to notice that the previous stress law is generic and valid for either compressible and incompressible fluids. If the fluid is incompressible, $div\mathbf{v}$ vanishes from the stress law and the bulk's viscosity coefficient λ disappears from the Newtonian law, leading to the following expression:

$$\sigma_{ij} = -p\delta_{ij} + \mu \left(\frac{\partial u_i}{\partial x_j} + \frac{\partial u_j}{\partial x_i} \right) \tag{2.13}$$

With the deformation law for a Newtonian fluid derived, the conservation of momentum equations can be written as a single vector equation by using the indicial notation:

$$\rho \frac{D\mathbf{v}}{Dt} = -\nabla p + \frac{\partial}{\partial x_j} \left[\mu \left(\frac{\partial u_i}{\partial x_j} + \frac{\partial u_j}{\partial x_i} \right) + \delta_{ij}\lambda div\mathbf{v} \right] + \mathbf{f_{body}} \tag{2.14}$$

2.1.3 Conservation of energy equation

For the conservation of energy equation, the first law of thermodynamics is considered:

$$dE_t = dQ + dW \tag{2.15}$$

Where Q is the heat added to the system, while W is the work done on the system, both per unit of volume. E_t includes the total energy of the system, hence internal energy, kinetic energy and potential energy, per unit of volume. However, it is also possible to express the potential energy as a body force which does work on the fluid particle as it moves. To do so, an extra term needs to be added to the energy equation which includes the effects of a source of energy per unit

of volume and time ($\mathbf{f_{body}} \cdot \mathbf{v}$), where $\mathbf{f_{body}}$ is a body force per unit of volume. Consequently, the time rate of change of the internal energy plus kinetic energy per unit volume ($E = u + e_k$, where u is the internal energy per unit of mass and $e_k = 1/2(u^2 + v^2 + w^2)$ is the kinetic energy per unit of mass) can be written using an Eulerian description as follows:

$$\rho \frac{DE}{Dt} = \frac{DQ}{Dt} + \frac{DW}{Dt} + \mathbf{f_{body}} \cdot \mathbf{v} \tag{2.16}$$

The only thing remaining is to express DQ/Dt and DW/Dt in terms of the properties of the fluid. The total rate of heat added to the fluid particle per unit volume can be expressed as:

$$\frac{DQ}{Dt} = -\frac{\partial \dot{q}_x}{\partial x} - \frac{\partial \dot{q}_y}{\partial y} - \frac{\partial \dot{q}_z}{\partial z} \tag{2.17}$$

Next, the rate of work done to the fluid element by the surface forces is equal to the product of the force with the velocity component in the direction of the force. Thus, the net rate of work done on the fluid element per unit volume can be expressed as:

$$\frac{DW}{Dt} = \frac{\partial}{\partial x}(u\sigma_{xx} + v\sigma_{xy} + w\sigma_{xz}) + \frac{\partial}{\partial y}(u\sigma_{yx} + v\sigma_{yy} + w\sigma_{yz}) + \frac{\partial}{\partial z}(u\sigma_{zx} + v\sigma_{zy} + w\sigma_{zz}) \tag{2.18}$$

The previous expression can be written as:

$$\frac{DW}{Dt} = \nabla \cdot (\boldsymbol{\sigma} \mathbf{v}) \tag{2.19}$$

As done before, the stress tensor can be split into an hydrostatic and a deviatoric part, which allows to rewrite the previous expression as:

$$\begin{aligned} \frac{DW}{Dt} = -\left(\frac{\partial(pu)}{\partial x} + \frac{\partial(pv)}{\partial y} + \frac{\partial(pw)}{\partial z}\right) + \frac{\partial}{\partial x}(u\tau_{xx} + v\tau_{xy} + w\tau_{xz}) + \\ \frac{\partial}{\partial y}(u\tau_{yx} + v\tau_{yy} + w\tau_{yz}) + \frac{\partial}{\partial z}(u\tau_{zx} + v\tau_{zy} + w\tau_{zz}) \end{aligned} \tag{2.20}$$

In summary, combining expressions 2.16, 2.17 and 2.20, the conservation of energy equation reads:

$$\begin{aligned} \rho \frac{DE}{Dt} = -\left(\frac{\partial \dot{q}_x}{\partial x} + \frac{\partial \dot{q}_y}{\partial y} + \frac{\partial \dot{q}_z}{\partial z}\right) \\ -\left(\frac{\partial(pu)}{\partial x} + \frac{\partial(pv)}{\partial y} + \frac{\partial(pw)}{\partial z}\right) + \frac{\partial}{\partial x}(u\tau_{xx} + v\tau_{xy} + w\tau_{xz}) + \\ \frac{\partial}{\partial y}(u\tau_{yx} + v\tau_{yy} + w\tau_{yz}) + \frac{\partial}{\partial z}(u\tau_{zx} + v\tau_{zy} + w\tau_{zz}) + \mathbf{f_{body}} \cdot \mathbf{v} \end{aligned} \tag{2.21}$$

Nevertheless, it is usually more common to extract the changes of the kinetic energy to get an equation for internal energy u or temperature T. To do so, expression 2.19 can be decomposed into:

$$\nabla \cdot (\boldsymbol{\sigma} \mathbf{v}) = \mathbf{v} \cdot (\nabla \cdot \boldsymbol{\sigma}) + \sigma_{ij} \frac{\partial u_i}{\partial x_j} \tag{2.22}$$

The first term on the right-hand-side is directly related to the momentum equation according to equation 2.6:

$$\nabla \cdot \boldsymbol{\sigma} = \rho \frac{D\mathbf{v}}{Dt} - \mathbf{f_{body}} \tag{2.23}$$

Thus:

$$\mathbf{v} \cdot (\nabla \cdot \boldsymbol{\sigma}) = \rho \mathbf{v} \frac{D\mathbf{v}}{Dt} - \mathbf{v} \cdot \mathbf{f_{body}} = \rho \frac{De_k}{Dt} - \mathbf{v} \cdot \mathbf{f_{body}} \tag{2.24}$$

Which is exactly equal to the potential and kinetic energy terms. Thus, by substituting equation 2.24 into equation 2.22, and the latter into equation 2.21, the kinetic and potential energy terms vanish, yielding an equation for the conservation of internal energy:

$$\rho \frac{D_u}{Dt} = -\left(\frac{\partial \dot{q_x}}{\partial x} + \frac{\partial \dot{q_y}}{\partial y} + \frac{\partial \dot{q_z}}{\partial z} \right) + \sigma_{ij} \frac{\partial u_i}{\partial x_j} \tag{2.25}$$

As usual, the stress tensor can be split into an hydrostatic and a deviatoric part, yielding:

$$\rho \frac{Du}{Dt} = -\left(\frac{\partial \dot{q_x}}{\partial x} + \frac{\partial \dot{q_y}}{\partial y} + \frac{\partial \dot{q_z}}{\partial z} \right) + \tau_{ij} \frac{\partial u_i}{\partial x_j} - p \nabla \cdot \mathbf{v} \tag{2.26}$$

From the continuity equation 2.3, the divergence of the velocity field can be expressed as:

$$\nabla \cdot \mathbf{v} = -\frac{1}{\rho} \frac{D\rho}{Dt} \tag{2.27}$$

Which can be used to rewrite the term $p \nabla \cdot \mathbf{v}$ of equation 2.26:

$$p \nabla \cdot \mathbf{v} = -\frac{p}{\rho} \frac{D\rho}{Dt} = \rho \frac{D}{Dt} \left(\frac{p}{\rho} \right) - \frac{Dp}{Dt} \tag{2.28}$$

Combining the previous expression with equation 2.26, one gets:

$$\rho \frac{D}{Dt} \left(u + \frac{p}{\rho} \right) = \frac{Dp}{Dt} - \nabla \cdot \dot{\boldsymbol{q}} + \tau_{ij} \frac{\partial u_i}{\partial x_j} \tag{2.29}$$

Recalling the definition of enthalpy $h = u + \frac{p}{\rho}$, the previous expression can be written as:

$$\rho \frac{Dh}{Dt} = \frac{Dp}{Dt} - \nabla \cdot \dot{\boldsymbol{q}} + \Phi \tag{2.30}$$

Where Φ is usually called the dissipation function, given by the following expression for a newtonian fluid:

$$\begin{aligned} \Phi = \mu \Bigg[& 2 \left(\frac{\partial u}{\partial x} \right)^2 + 2 \left(\frac{\partial v}{\partial y} \right)^2 + 2 \left(\frac{\partial w}{\partial z} \right)^2 + \left(\frac{\partial v}{\partial x} + \frac{\partial u}{\partial y} \right)^2 \\ & + \left(\frac{\partial w}{\partial y} + \frac{\partial v}{\partial z} \right)^2 + \left(\frac{\partial u}{\partial z} + \frac{\partial w}{\partial x} \right)^2 \Bigg] + \lambda \left(\frac{\partial u}{\partial x} + \frac{\partial v}{\partial y} + \frac{\partial w}{\partial z} \right)^2 \end{aligned} \tag{2.31}$$

However, it is usually common to use Fourier's law of heat conduction to relate the heat fluxes to the local temperature gradient:

$$\rho\frac{Dh}{Dt} = \frac{Dp}{Dt} + div(k\nabla T) + \Phi \tag{2.32}$$

Equation 2.32 can be modified to get a temperature equation. Recalling the thermodynamic identity:

$$dh = C_p dT + (1 - \beta T)\frac{dp}{\rho} \tag{2.33}$$

The enthalpy equation can be written as:

$$\rho C_p\frac{DT}{Dt} = \beta T\frac{Dp}{Dt} + div(k\nabla T) + \Phi \tag{2.34}$$

At the limit of low-velocity or incompressible flow, the previous equation reduces to:

$$\rho C_p\frac{DT}{Dt} \approx div(k\nabla T) \tag{2.35}$$

And finally, considering constant thermal conductivity, a more familiar equation can be obtained:

$$\rho C_p\frac{DT}{Dt} \approx k\nabla^2 T \tag{2.36}$$

2.1.4 Summary of the basic equations

In summary, the the equations of conservation of mass, momentum and energy derived previously are shown below:

$$\frac{\partial\rho}{\partial t} + \nabla\cdot(\rho\mathbf{v}) = 0 \tag{2.37}$$

$$\rho\frac{D\mathbf{v}}{Dt} = -\nabla p + \frac{\partial}{\partial x_j}\left[\mu\left(\frac{\partial u_i}{\partial x_j} + \frac{\partial u_j}{\partial x_i}\right) + \delta_{ij}\lambda div\mathbf{v}\right] + \mathbf{f_{body}} \tag{2.38}$$

$$\rho\frac{Dh}{Dt} = \frac{Dp}{Dt} + div(k\nabla T) + \Phi \tag{2.39}$$

As mentioned previously, a set of 5 equations has been found, involving 9 variables: u, v, w, p, T, ρ, μ, h and k. Consequently, 4 state relations are used to close the system:

$$\rho = \rho(p, T) \tag{2.40}$$
$$\mu = \mu(p, T) \tag{2.41}$$
$$h = h(p, T) \tag{2.42}$$
$$k = k(p, T) \tag{2.43}$$

Finally, it is important to mention that the equations found are fairly general, as the only assumptions made are:

- The fluid forms a (mathematical) continuum
- The fluid particles are assumed to be in thermodynamic equilibrium
- The heat conduction follows Fourier's law
- There are no internal heat sources
- Newtonian fluid is assumed

2.1.5 Non-dimensional form of the Navier-Stokes equations

It is common to express the Navier-Stokes equations in terms of non-dimensional parameters. To do so, the following dimensionless variables (denoted with an asterisk as a superscript) are defined:

$$\mathbf{v}^* = \mathbf{v}/U \tag{2.44}$$
$$t^* = \frac{t}{L/U} \tag{2.45}$$
$$p^* = \frac{p}{\rho_0 U^2} \tag{2.46}$$
$$\rho^* = \rho/\rho_0 \tag{2.47}$$
$$\mathbf{r}^* = \mathbf{r}/L \tag{2.48}$$
$$T^* = T/T_0 \tag{2.49}$$

Where $\mathbf{r} = (x, y, z)$; U is a characteristic velocity, L is a characteristic length, ρ_0 is a reference density and T_0 is a reference temperature, all of them problem-dependent. Substituting all the previous relations into equations 2.37, 2.38 and 2.39 one obtains:

$$\frac{\partial \rho^*}{\partial t^*} + \nabla^*(\rho^* \mathbf{v}^*) = 0 \tag{2.50}$$

$$\rho^* \frac{D\mathbf{v}^*}{Dt^*} = -\nabla^* p^* + \frac{\partial}{\partial x_j^*}\left[\left(\frac{\mu}{L\rho_0 U}\right)\left(\frac{\partial u_i^*}{\partial x_j^*} + \frac{\partial u_j^*}{\partial x_i^*}\right) + \delta_{ij}\left(\frac{\lambda}{L\rho_0 U}\right) div^* \mathbf{v}^*\right] + \mathbf{f_{body}}^* \tag{2.51}$$

$$\begin{aligned} \rho^* \frac{DT^*}{Dt^*} = \left(\frac{\beta U^2}{C_p}\right) T^* \frac{Dp^*}{Dt^*} + div^*\left(\left(\frac{k}{C_p \mu}\right)\left(\frac{\mu}{L\rho_0 U}\right)\nabla^* T^*\right) + \\ \left(\frac{\mu U}{L\rho_0 C_p T_0}\right)\left[2\left(\frac{\partial u^*}{\partial x^*}\right)^2 + 2\left(\frac{\partial v^*}{\partial y^*}\right)^2 + 2\left(\frac{\partial w^*}{\partial z^*}\right)^2 + \left(\frac{\partial v^*}{\partial x^*} + \frac{\partial u^*}{\partial y^*}\right)^2 \right. \\ \left. + \left(\frac{\partial w^*}{\partial y^*} + \frac{\partial v^*}{\partial z^*}\right)^2 + \left(\frac{\partial u^*}{\partial z^*} + \frac{\partial w^*}{\partial x^*}\right)^2\right] + \left(\frac{\lambda U}{L\rho_0 C_p T_0}\right)\left(\frac{\partial u^*}{\partial x^*} + \frac{\partial v^*}{\partial y^*} + \frac{\partial w^*}{\partial z^*}\right)^2 \end{aligned} \tag{2.52}$$

As it can be seen, numerous non-dimensional parameters have appeared in the dimensionless equations. The most relevant ones are briefly summarised below:

2.1.5.1 Non-dimensional parameters

- Reynolds number:

  The Reynolds number describes the ratio between inertial forces and viscous forces:

$$Re = \frac{\rho_0 L U}{\mu} \tag{2.53}$$

  The Reynolds number is an important dimensionless parameter to predict the onset of turbulent flow, but also in engineering purposes to achieve dynamic similitude of different fluid flows. As it can be seen in the dimensionless equations above, the inverse of the Reynolds number can be found in the conservation of momentum equation multiplying the non-dimensional diffusive term, and in the conservation of energy equation multiplying the gradient of the temperature. Consequently, it is clear that a high Reynolds number reduces the importance of the diffusive transport of both momentum and temperature over the convective transport, being the latter the dominant. For flows with low Reynolds number, the opposite behaviour is observed.

- Prandtl number:

  The Prandtl number expresses the ratio of momentum diffusivity to thermal diffusivity [10]:

$$Pr = \frac{\nu}{\alpha} = \frac{\mu/\rho}{k/(C_p \rho)} = \frac{C_p \mu}{k} \tag{2.54}$$

  As it can be seen, the inverse of the Prandtl number is present in the energy equation multiplying the gradient of the non-dimensional temperature, multiplying the inverse of the Reynolds number. A small Prandtl number indicates that the thermal diffusivity dominates, while a large one indicates a domination of the momentum diffusivity. Additionally, it is a very useful parameter to relate the relative thickness of the momentum and thermal boundary layers. When the Prandtl number is small, the thermal boundary layer is much thicker than the velocity boundary layer. When the Prandtl number is large, the opposite is observed.

- Péclet number:

  The Péclet number is a non-dimensional number that expresses the ratio between the advective transport rate of a certain physical quantity, to the diffusive transport rate of the same quantity [11].

$$Pe = \frac{\text{advective transport rate}}{\text{diffusive transport rate}} \tag{2.55}$$

  It is a very important parameter for the study of the transport phenomena in a continuum. If the physical quantity of study is the transport of certain species or mass transfer, the

Péclet number is just the product of the Reynolds number with the Schmidt number. On the other hand, the thermal Péclet number is equivalent to the product of the Reynolds number and the Prandtl number. The inverse of this product, and thus, the inverse of the thermal Péclet number, can be found in the conservation of energy equation, with its physical meaning becoming clear. A large Péclet number implies a longer diffusion time than the time it takes for convective transport. Consequently, the latter is the dominant transport mechanism. If the Péclet number is small, the opposite behaviour is observed.

- Grashof number:

The Grashof number is a non-dimensional number that expresses the ratio between the buoyancy forces and the viscous forces acting on a fluid particle [12].

$$Gr = \frac{g\beta(T - T_0)L^3}{\nu^2} \tag{2.56}$$

It can be understood as an analogous parameter to the Reynolds number but in natural convection flows. Its value can be used to determine if transition to turbulent flow will occur or not, as its onset happens for a certain critical Grashof number.

The ratio of the Grashof number to the Reynolds number squared (the Richardson number (R_i)), is a useful parameter to determine if natural convection or forced convection will occur. A Richardson number much larger than unity implies that natural convection is dominant, while a value much smaller than 1 implies that force convection dominates.

- Rayleigh number:

The Rayleight number is a non-dimensional number that describes the ratio of the time scale of the diffusive thermal transport, to the time scale for the convective thermal transport.

$$Ra = \frac{\rho\beta(T - T_0)L^3 g}{\nu\alpha} \tag{2.57}$$

Being the ratio between a diffusive and a convective time scales, the Rayleigh number is a type of Péclet number. From its definition, it can be easily computed as the product between the Grashof number and the Prandtl number.

- Nusselt number:
The Nusselt number is a non-dimensional number that expresses the ratio of convective heat transfer at a boundary in a fluid, to conductive heat transfer:

$$Nu = \frac{hL}{k} \tag{2.58}$$

Where h is the convective heat transfer coefficient and should not be confused with the enthalpy of the fluid. The Nusselt number is closely related to the Rayleigh number to determine if heat transfer is mainly due to conduction or due to convection. A value of unity implies a heat transfer by pure conduction, while higher values might be found for laminar flow (usually in the range of $1 < Nu < 10$) and turbulent flow (for $100 < Nu < 1000$) [13]. For free convection, the Nusselt number is typically a function of the Rayleigh number and the Prandtl number, while for forced convection it is usually a function of the Reynolds number and the Prandtl number. A large variety of empirical correlations can be found in various references for different geometries.

2.2 Finite Difference Method vs Finite Volume Method vs Finite Element Method

There are different approaches when trying to numerically solve the Navier-Stokes equations. The most well-known ones are the Finite Difference Method, the Finite Volume Method and the Finite Element Method. Each of them has its advantages and its drawbacks. In this section, a brief description of those is given to get a general insight of them:

2.2.1 Finite Difference Method (FDM)

The basic idea behind the Finite Difference Method is to replace the partial derivatives of the governing equations i.e, equations 2.37, 2.38 and 2.39; in differential form, with finite differences of the value of interest at various points in space and time, by using an appropriate Taylor expansion series of the desired order. With the partial derivatives expressed in a discrete manner, a discretised set of governing equations is obtained, which are evaluated at those fixed spatial and temporal grid points (the mesh nodes).

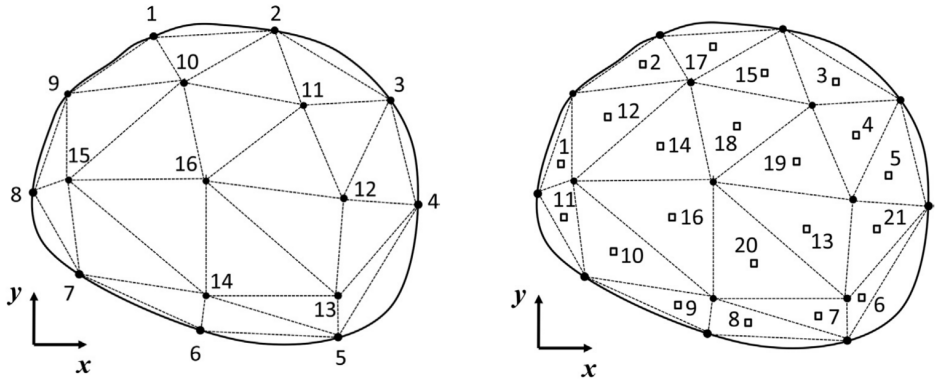

Figure 1: Finite Element mesh or Finite Difference mesh (left) and Finite Volume Mesh (right) [1]

2.2.2 Finite Volume Method (FVM)

In the Finite Volume Method, the domain is divided into a set of computational domains called cells or control volumes. The edges of those cells are known as the faces, while the vertices are the

nodes, which are equivalent to the nodes used in the FDM. However, in the FVM,the information is stored at the cells' centroids, rather than at the nodes. The governing equations are integrated at each control volume, and the volume integrals are converted into surface integrals by applying the Gauss divergence theorem. Consequently, the governing equations are not solved directly and rather, a weak form is solved. One of the biggest advantages of the FVM over the FDM or FEM is that, by obtaining surface integrals over the control volume faces, the finite volume equations are, in essence, flux balance equations of the governing PDE's. This is specially useful in those fields in which the PDEs represent conservation laws, such as in CFD, as mass, momentum and energy are conserved by definition.

2.2.3 Finite Element Method (FEM)

The Finite Element Method is a method for solving PDEs based on the principle of variation of parameters [1]. In a similar way to the FVM formulation, it also determines the weak form solution of the governing equations. However, in this case, the governing PDE's are first multiplied by a test function, and then integrated over the whole domain. The domain is also discretised into a set of elements (the finite elements) similar to the ones used for the FDM shown in figure 1. The test function and the solution in each of the elements is described by a linear combination of interpolation functions or shape functions. This linear combination allows to find the values of interest at non-nodal points of the domain, by interpolating the nodal values, which are the unknowns of the problem. The shape functions, thus, allow to describe how the field variables vary within the finite element. Due to the fact that both the test function and the solution are expressed through this linear combination, a linear system of algebraic equation can be obtained, which is used to solve for the values at the nodal points and, through the shape function, the values at any point inside the domain. This method, although being really useful, is not very used for fluid dynamics applications. Rather, it is extensively applied to the fields of stress and structural analysis.

2.2.4 Summary of FDM and FVM

Being the Finite Volume Method and the Finite Difference Method the two most common approaches to solve the PDEs of the governing equations of fluid dynamics, their advantages and drawbacks should be briefly described. As already outlined previously, the FDM solves the governing equations in its differential (original) form, obtaining a solution known as the strong form solution. The differential operators are computed by using the values of interest at fixed interconnected nodes inside the domain and at its boundaries. On the other hand, the FVM uses a set of control volumes in which the integral of the governing equations is computed. Consequently, the solution obtained is known as the weak form solution, as it corresponds to the solution of the integral form of the PDEs. Nevertheless, both methods need the use of a method to approximate derivatives in a discrete way, which is typically done through a Taylor expansion series of the desired order. Consequently, the truncation errors produced in the FVM and FDM are comparable, which implies that the error produced by a finite difference scheme is comparable to the one produced by a finite volume scheme of the same order.

However, one of the biggest differences between both methods is the way boundary conditions are treated. In the FDM, nodes are also located at the boundaries of the domain. This implies that Dirichlet boundary conditions can be directly imposed to the boundary node. However, the

governing equation can not be satisfied at the boundary, as it would lead to an overspecification of the problem. On the other hand, when Neumann boundary conditions are imposed, both the boundary condition and the governing equation can be imposed at this node, giving much better accuracy than only applying the boundary condition [1]. On the other hand, in the FVM there is typically any node applied directly on the domain boundaries. This implies that the boundary conditions are directly applied to the cell faces. This is perhaps the biggest difference between both methods, because it means that in the FVM, the governing equation is always satisfied in the whole computational domain regardless of its shape, discretization or type of boundary conditions. On the other hand, for the FDM, the fraction of the domain in which the governing equation is satisfied heavily depends on the mesh used and type of boundary conditions applied. Due to this, both methods exhibit really different behaviour regarding its global conservation properties. In the FDM, as the governing equation is partially satisfied inside the domain depending on the mesh used, the global conservation is also mesh-dependent. On the other hand, in the FVM local and global conservation is assured. Another additional advantage of the FVM over the FDM is found in problems in which material discontinuities are present. Being the FVM an integral method, those discontinuities can be treated with ease, while the FDM encounters problems.

Consequently, given all the differences outlined between both methods and the advantages of the FVM over the FDM, the former is chosen to be used for the development of this thesis.

3 Symmetry-preserving discretization

The conservative nature of the Navier-Stokes equations is really dependent on the symmetry of the differential operators used.

In order to analyse the conservation and stability properties, the finite-volume discretization of the Navier-Stokes equations (neglecting the conservation of energy equation) in matrix-vector notation can be written as:

$$\boldsymbol{\Omega}_0 \frac{\mathrm{d}\boldsymbol{u}_h}{\mathrm{d}t} + \boldsymbol{C}_0(\boldsymbol{u}_h)\boldsymbol{u}_h = \boldsymbol{D}_0\boldsymbol{u}_h - \boldsymbol{\Omega}_0\boldsymbol{G}_0\mathbf{p}_h \tag{3.1}$$

$$\mathbf{M}_0\mathbf{u}_h = 0 \tag{3.2}$$

where $\mathbf{p}_h = (p_1, p_2, ..., p_n)^* \in \mathbb{R}^n$ is the cell-centered pressure field, $\mathbf{u}_h \in \mathbb{R}^{3n}$ is the staggered velocity fields, and n is the number of control volumes used. $\mathbf{u}_h$ is defined as a column vector arranged as $\mathbf{u}_h = (\mathbf{u}_1, \mathbf{u}_2, \mathbf{u}_3)^*$, where $\mathbf{u}_i = ((u_i)_1, (u_i)_2, ...(u_i)_n)^*$ are the vectors containing the velocity component of each control volume corresponding to the i^{th} spatial direction. The matrix $\mathbf{\Omega_h} \in \mathbb{R}^{3n\times 3n}$ is a diagonal matrix containing the size of each control volume, while $\mathbf{C}_0(\mathbf{u}_h) \in \mathbb{R}^{3n\times 3n}$ and $\mathbf{D}_0 \in \mathbb{R}^{3n\times 3n}$ represent the convective and diffusive operators respectively. By defining the discrete inner product between $\mathbf{a}$ and $\mathbf{b}$ as:

$$\langle \boldsymbol{a}, \boldsymbol{b} \rangle = \boldsymbol{a}^* \Omega \boldsymbol{b} \tag{3.3}$$

The discrete kinetic energy is then given by $\|\boldsymbol{u}_h\|^2 \equiv \boldsymbol{u}_h^* \Omega \boldsymbol{u}_h$. The temporal evolution of the discrete kinetic energy can be obtained by left-multiplying equation (3.1) by $\mathbf{u_h}^*$and summing the resulting expression with its transpose:

$$\frac{\mathrm{d}}{\mathrm{d}t}\|\boldsymbol{u}_h\|^2 = -\boldsymbol{u}_h^*\left(\boldsymbol{C}_0\left(\boldsymbol{u}_h\right) + \boldsymbol{C}_0^*\left(\boldsymbol{u}_h\right)\right)\boldsymbol{u}_h - \boldsymbol{u}_h^*\left(\boldsymbol{D}_0 + \boldsymbol{D}_0^*\right)\boldsymbol{u}_h - \boldsymbol{u}_h^*\Omega\boldsymbol{G}_0\boldsymbol{p}_h - \boldsymbol{p}_h^*\boldsymbol{G}_0^*\Omega^*\boldsymbol{u}_h \tag{3.4}$$

If no diffusion is present, $\mathbf{D}_0 = 0$ and the global kinetic energy reduces to:

$$\frac{\mathrm{d}}{\mathrm{d}t}\|\boldsymbol{u}_h\|^2 = -\boldsymbol{u}_h^*\left(\boldsymbol{C}_0\left(\boldsymbol{u}_h\right) + \boldsymbol{C}_0^*\left(\boldsymbol{u}_h\right)\right)\boldsymbol{u}_h - \boldsymbol{u}_h^*\Omega\boldsymbol{G}_0\boldsymbol{p}_h - \boldsymbol{p}_h^*\boldsymbol{G}_0^*\Omega^*\boldsymbol{u}_h \tag{3.5}$$

Which implies that kinetic energy is conserved if both the convective and pressure terms vanish in the discretized kinetic energy equation, i.e:

$$\boldsymbol{u}_h^*\left(\boldsymbol{C}_0\left(\boldsymbol{u}_h\right) + \boldsymbol{C}_0^*\left(\boldsymbol{u}_h\right)\right)\boldsymbol{u}_h = 0 \tag{3.6}$$

$$\boldsymbol{u}_h^*\Omega\boldsymbol{G}_0\boldsymbol{p}_h + \boldsymbol{p}_h^*\boldsymbol{G}_0^*\Omega^*\boldsymbol{u}_h = 0 \tag{3.7}$$

Equation 3.6 is satisfied if and only if $\mathbf{C}_0(\mathbf{u}_h) = -\mathbf{C}_0^*(\mathbf{u}_h)$ (i.e, the convective operator is skew-symmetric). Moreover, to make sure that the contribution of the pressure term vanishes, the negative transpose of the discrete gradient operator can be defined to be equal to the divergence operator. If those conditions apply, the global kinetic energy (when diffusion effects are present) is reduced to:

$$\frac{\mathrm{d}}{\mathrm{d}t}\left\|\boldsymbol{u}_h\right\|^2 = -\boldsymbol{u}_h^*\left(\boldsymbol{D}_0 + \boldsymbol{D}_0^*\right)\boldsymbol{u}_h \leqslant 0 \tag{3.8}$$

The inequality appears due to the fact that the diffusive term must be dissipative. This implies that the matrix $(\boldsymbol{D}_0 + \boldsymbol{D}_0^*)$ must be positive-definite. However, even though it is not strictly necessary [14], $\mathbf{D}_0$ is assumed to be not only positive-definite but also symmetric, like the continuous operator, $-\Delta$.

As a result, when it comes to the spatial discretization of the equations, the previous constraints need to be taken into account in order to preserve the global kinetic energy. In the following subsections, a second order spatial discretization of the different operators is presented and illustrated with a two-dimensional mesh using staggered control volumes for the velocity computation, as the extension to 3D is straightforward.

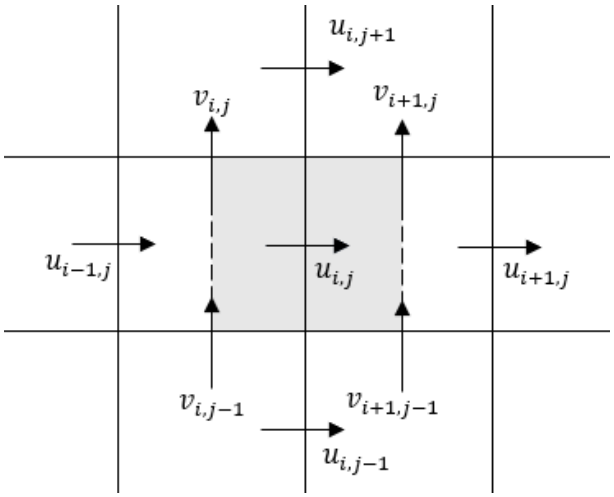

Figure 2: 2D representation of the velocity control volume staggered in the x direction ($\Omega_{i+1/2,j}$)

3.1 Discretization of the convective operator

Recalling the Reynold's transport theorem for a function f of x and t:

$$\frac{d}{dt}\int_\Omega f dV = \int_\Omega \frac{\partial f}{\partial t} dV + \int_{\partial\Omega} f\mathbf{u}\cdot\mathbf{n} dS \tag{3.9}$$

Where Ω is an arbitrary part of the fluid domain (in this case the control volume) at a particular instant t. If the function f is equal to the velocity, the momentum transport equation is obtained. The spatial discretization of this equation in the region $\Omega_{i+1/2,j}$ reads the following, according to figure 2:

$$\left|\Omega_{i+1/2,j}\right|\frac{\mathrm{d}u_{i,j}}{\mathrm{d}t} + (\dot{m}_e)_{sx}u_{i+1/2,j} + (\dot{m}_n)_{sx}u_{i,j+1/2} - (\dot{m}_w)_{sx}u_{i-1/2,j} - (\dot{m}_s)_{sx}u_{i,j-1/2} \tag{3.10}$$

Where $(\dot{m}_e)_{sx}$, $(\dot{m}_w)_{sx}$, $(\dot{m}_n)_{sx}$ and $(\dot{m}_s)_{sx}$ are the massflows through the east, west, north and south control volume faces, respectively, in which the subscript $_{sx}$ indicates that the mass fluxes

are computed in the mesh staggered in the x direction. $u_{i+1/2,j}$, $u_{i-1/2,j}$, $u_{i,j+1/2}$ and $u_{i,j-1/2}$ are the convected velocities through the east, west, north and south faces, respectively. At this point, a question arises regarding the computation of the convected velocities at the cell faces in order to assure that the convected-operator is skew-symmetric. To study this, a general interpolation rule for the velocities at the cell faces is considered:

$$u_{i+1/2,j} = (1-\omega_{i,j})u_{i+1,j} + \omega_{i,j}u_{i,j} \tag{3.11}$$

Where $\omega_{i,j}$ is a coefficient dependent on the control volume size. By substituting this interpolation rule into equation 3.10, the following is obtained:

$$\begin{aligned}\left|\Omega_{i+1/2,j}\right| \frac{\mathrm{d}u_{i,j}}{\mathrm{d}t} &+ (\dot{m}_e)_{sx}(1-\omega_{i,j})u_{i+1,j} + (\dot{m}_e)_{sx}\omega_{i,j}u_{i,j} + (\dot{m}_n)_{sx}(1-\omega_{i,j})u_{i,j+1} + (\dot{m}_n)_{sx}\omega_{i,j}u_{i,j} \\ &-(\dot{m}_w)_{sx}(1-\omega_{i,j})u_{i-1,j} - (\dot{m}_w)_{sx}\omega_{i,j}u_{i,j} - (\dot{m}_s)_{sx}(1-\omega_{i,j})u_{i,j-1} - (\dot{m}_s)_{sx}\omega_{i,j}u_{i,j}\end{aligned} \tag{3.12}$$

In equation 3.12, it can be observed how the coefficient of $u_{i+1,j}$ is equal to $(\dot{m}_e)_{sx}(1-\omega_{i,j})$, while the coefficient of the term $u_{i,j}$ of the control volume on the right of the one in figure 2, would be $-\omega_{i,j}(\dot{m}_e)_{sx}$. For skew-symmetry, both coefficients should be equal but with opposite signs, hence:

$$(1-\omega_{i,j})(\dot{m}_e)_{sx} = \omega_{i,j}(\dot{m}_e)_{sx} \tag{3.13}$$

which is only satisfied if $\omega_{i,j} = 1/2$, and hence, independent of the grid size. Additionally, the elements of the diagonal of the convective operator should be equal to zero. The diagonal coefficient of expression 3.12 is given by:

$$\frac{1}{2}((\dot{m}_e)_{sx} + (\dot{m}_n)_{sx} - (\dot{m}_w)_{sx} - (\dot{m}_s)_{sx}) \tag{3.14}$$

Which is equal to the net mass flux through the faces of the control volume, and hence, equal to zero due to mass conservation. The respective mass flow rates are a function of the discrete velocity vector $\mathbf{u}_h$. In summary, the following spatial-discretization for the x-component of the convective term is obtained:

$$\begin{aligned}\left|\Omega_{i+1/2,j}\right| \frac{\mathrm{d}u_{i,j}}{\mathrm{d}t} &+ \frac{1}{2}((\dot{m}_e)_{sx} + (\dot{m}_n)_{sx} - (\dot{m}_w)_{sx} - (\dot{m}_s)_{sx})u_{ij} + \frac{1}{2}(\dot{m}_e)_{sx}u_{i+1,j} + \\ &\frac{1}{2}(\dot{m}_n)_{sx}u_{i,j+1} - \frac{1}{2}(\dot{m}_w)_{sx}u_{i-1,j} - \frac{1}{2}(\dot{m}_s)_{sx}u_{i,j-1}\end{aligned} \tag{3.15}$$

While the extension to the other two dimensions is analogous and straightforward, allowing to express the convective operator in matrix form: $\mathbf{C}_0(\mathbf{u}_h)$.

3.2 Discretization of the gradient and divergence operators

As already stated, the mass fluxes need to be expressed in terms of the discrete velocity vector $\mathbf{u}_h$. Hence, the coefficients of the convective operator become a function of $\mathbf{u}_h$ as well (i.e $\mathbf{C}_0(\mathbf{u}_h)$).

Considering a main pressure control volume as the one sketched in figure 3, the integral of the divergence of the velocity can be computed as:

$$\int_{\Omega} \nabla \cdot \mathbf{v} = \int_{\partial\Omega} \mathbf{v} \cdot \mathbf{n} dS \tag{3.16}$$

In which the Gauss theorem has been applied.

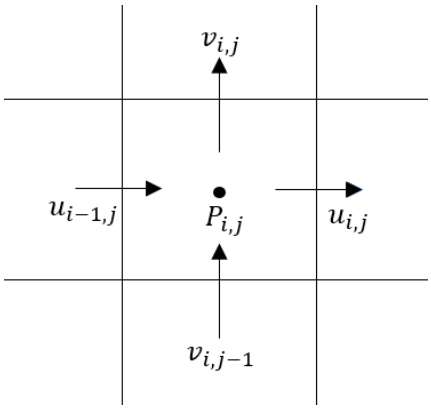

Figure 3: 2D representation of the main control volume ($\Omega_{i,j}$)

By applying the mid-point rule to approximate the integral 3.16, the conservation of mass yields:

$$\begin{aligned} (\dot{m}_e)_c + (\dot{m}_n)_c - (\dot{m}_w)_c - (\dot{m}_s)_c = \\ (y_j - y_{j-1})u_{i,j} - (y_j - y_{j-1})u_{i-1,j} + (x_i - x_{i-1})v_{i,j} - (x_i - x_{i-1})v_{i,j-1} \end{aligned} \tag{3.17}$$

In which the mass fluxes with the subscript $_c$ represent the massflows computed through the boundaries of the main cell-centered control volume. By rewriting the previous expression in matrix form taking into account all the control volumes of the domain, equation 3.17 can be written as $\mathbf{M}_0\mathbf{u}_h$, in which the coefficient matrix $\mathbf{M}_0$ represents the discretization of the divergence operator, integrated over the control volumes. The right-hand side of equation

$$\mathbf{M}_0\mathbf{u}_h = 0 \tag{3.18}$$

represents the net mass flux through the boundaries of the computational domain. For periodic boundary conditions or closed systems, the right-hand side is equal to zero.

For the discretization of the gradient operator, the symmetry relation:

$$\langle \nabla p, \mathbf{v} \rangle = -\langle p, \nabla \cdot \mathbf{v} \rangle \tag{3.19}$$

is used, yielding the following operator property: $\nabla^* = -\nabla$, which states that the continuous gradient operator equals the negative of the transpose of the divergence. If $\mathbf{p}_h$ denotes the discrete pressure and $\mathbf{G}_0\mathbf{p}_h$ the discrete pressure gradient, the relation 3.19:

$$(\boldsymbol{G}_0\boldsymbol{p}_h)^* \, \boldsymbol{\Omega}\boldsymbol{u}_h = \boldsymbol{p}_h^* \boldsymbol{G}_0^* \boldsymbol{\Omega}\boldsymbol{u}_h = -\boldsymbol{p}_h^* \boldsymbol{M}_0 \boldsymbol{u}_h \tag{3.20}$$

holds if $\mathbf{G}_0 = -\boldsymbol{\Omega}^{-1}\mathbf{M}_0^*$

3.3 Discretization of the diffusive operator

The diffusive operator can be computed as the product of the divergence and a gradient operator. In short, the diffusive operator can be written as:

$$\frac{1}{Re}\nabla \cdot \nabla \tag{3.21}$$

However, due to the fact that staggered grids are used, the approximation $\frac{1}{Re}\mathbf{M}_0\mathbf{\Omega}_0^{-1}\mathbf{M}_0^*$ cannot be used. Therefore, the matrices $\mathbf{M}_0^u$, $\mathbf{M}_0^v$ and $\mathbf{M}_0^w$ need to be derived, which stand for the discrete integration of the divergence operators over the staggered meshes in the x, y and z directions, respectively. In this case, the $\mathbf{M}_0^u$ operator would be applied to the function in the grid staggered in the x direction, while the operator $\mathbf{M}_0^v$ would be applied to the staggered grid in the y direction. Considering the discretization in the mesh staggered in x, like the one shown in figure 2, the diffusive flux through the faces of the control volume $\Omega_{i+1/2,j}$ of $u_{i.j}$ would read:

$$\begin{aligned} &\frac{1}{Re}\frac{u_{i+1,j}-u_{i,j}}{x_{i+1}-x_i}(y_j-y_{j-1}) - \frac{1}{Re}\frac{u_{i,j}-u_{i-1,j}}{x_i-x_{i-1}}(y_j-y_{j-1}) + \\ &\frac{1}{Re}\frac{u_{i,j+1}-u_{i,j}}{y_{j+1/2}-y_{j-1/2}}(x_{i+1/2}-x_{i-1/2}) - \frac{1}{Re}\frac{u_{i,j}-u_{i,j-1}}{y_{j-1/2}-y_{j-3/2}}(x_{i+1/2}-x_{i-1/2}) \end{aligned} \tag{3.22}$$

Which could be written in matrix form as $\mathbf{D}_0^u\mathbf{u}_h$. The process to compute the diffusive flux through the faces of the control volumes for the staggered meshes in the y and z direction is analogous and those could also be written in matrix form as $\mathbf{D}_0^v\mathbf{u}_h$ and $\mathbf{D}_0^w\mathbf{u}_h$ respectively. In summary, the discretization of the diffusive term in the Navier-Stokes equations becomes $\mathbf{D}_0\mathbf{u}_h$, where $\mathbf{D}_0 = diag(\mathbf{D}_0^u, \mathbf{D}_0^v, \mathbf{D}_0^w)$.

Finally, before presenting the verification of the symmetry-preserving scheme implemented, it is important to mention that the scheme presented is second-order accurate. However, higher-order schemes could be derived (see for instance [15]).

3.4 Fractional Step Method

The basis behind the Fractional Step Method, which is used to solve the incompressible form of the Navier-Stokes equations, is the well-known Helmholtz-Hodge theorem:

Theorem: *Given a vector field $\boldsymbol{\omega}$ defined in a bounded domain $\Omega \subseteq R^n$ for $n = 2, 3$, with a smooth boundary $\partial\Omega$, the vector field can be uniquely decomposed in the following form:*

$$\boldsymbol{\omega} = \boldsymbol{u} + \nabla\varphi \tag{3.23}$$

Where φ is a scalar field over Ω and $\boldsymbol{u}$ is a vector field of Ω that satisfies the following constraints:

- $\nabla \cdot \boldsymbol{u} = 0$
- $\boldsymbol{u} \cdot \boldsymbol{n} = 0$ *over* $\partial\Omega$

This theorem can be easily proved given the following considerations. Considering the divergence of the product of a vector field with a scalar quantity and its decomposition:

$$\nabla \cdot (\mathbf{u}\varphi) = (\nabla \cdot \mathbf{u})\varphi + \mathbf{u} \cdot (\nabla\varphi) \tag{3.24}$$

The decomposition yields, for a divergence-free vector field:

$$\nabla \cdot (\mathbf{u}\varphi) = \mathbf{u} \cdot (\nabla\varphi) \tag{3.25}$$

If the previous equality is used to compute the scalar product between the vector field $\mathbf{u}$ and $\nabla\varphi$ in the region Ω, and applying the divergence theorem:

$$\int_\Omega \nabla\varphi \cdot \mathbf{u}\mathbf{d}\Omega = \int_\Omega \nabla \cdot (\varphi\mathbf{u})\mathbf{d}\Omega = \int_{\partial\Omega} (\varphi\mathbf{u}) \cdot \mathbf{n}dS = 0 \tag{3.26}$$

Which is equal to zero, given that the fluxes through the domain boundaries are null according to the constraints previously defined. Consequently, it is clear that the vector fields $\mathbf{u}$ and $\nabla\varphi$ are orthogonal. However, the unicity of the decomposition is still to be proved. To do so, two different decompositions can be considered:

$$\omega = \mathbf{u_1} + \nabla\varphi_1 = \mathbf{u_2} + \nabla\varphi_2 \tag{3.27}$$

Rearranging terms:

$$\mathbf{u_1} - \mathbf{u_2} + \nabla(\varphi_1 - \varphi_2) = 0 \tag{3.28}$$

At this point, considering the scalar product of expression 3.28 with $(\mathbf{u_1} - \mathbf{u_2})$, it is clear that:

$$\int_\Omega \left[\|\mathbf{u}_1 - \mathbf{u}_2\|^2 + (\mathbf{u}_1 - \mathbf{u}_2) \cdot \nabla (\varphi_1 - \varphi_2) \right] \mathbf{d}\Omega = \int_\Omega ||\mathbf{u_1} - \mathbf{u_2}||^2 \mathbf{d}\boldsymbol{\Omega} = 0 \tag{3.29}$$

Therefore, according to equation 3.29, it is evident that, given the orthogonality relation:

$$\mathbf{u_1} = \mathbf{u_2} \tag{3.30}$$

$$\nabla\varphi_1 = \nabla\varphi_2 \rightarrow \varphi_1 = \varphi_2 + \text{constant} \tag{3.31}$$

Proving that the decomposition, depicted in the following figure, is unique.

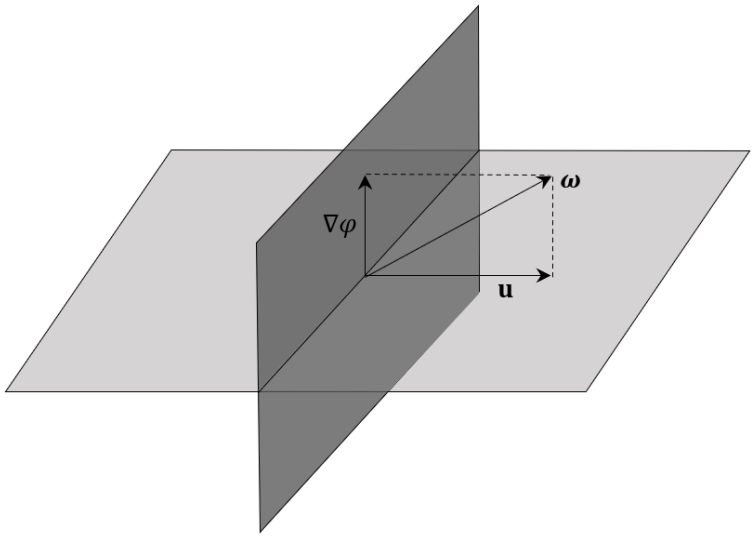

Figure 4: Helmholtz-Hodge decomposition

By recalling the discretised Navier-Stokes equations 3.1 and 3.2, the Helmholtz-Hodge theorem can be used to express the equations in terms of a predicted velocity (non-divergent free). Afterwards, the equations can be projected into a subspace with null divergence. However, equations need to be discretised in time beforehand. The continuity equation can be integrated implicitly:

$$\mathbf{M}_0 \mathbf{u}_h^{n+1} = 0 \tag{3.32}$$

Next, the transient term of the momentum equation can be discretised using a second order central difference scheme:

$$\left.\frac{\mathrm{d}\boldsymbol{u}_h}{\mathrm{d}t}\right|^{n+1/2} \approx \frac{\boldsymbol{u}_h^{n+1} - \boldsymbol{u}_h^n}{\Delta t} + \mathcal{O}(\Delta t^2) \tag{3.33}$$

While the convective and diffusive terms are grouped and discretised using a fully explicit second order Adams-Bashforth scheme:

$$\boldsymbol{R}(\boldsymbol{u}_h)^{n+1/2} \approx 3/2\boldsymbol{R}(\boldsymbol{u}_h)^n - 1/2\boldsymbol{R}(\boldsymbol{u}_h)^{n-1} + \mathcal{O}(\Delta t^2) \tag{3.34}$$

Where $\boldsymbol{R}(\boldsymbol{u}_h) = \boldsymbol{\Omega}^{-1}(-\boldsymbol{C}_0(\boldsymbol{u}_h)\boldsymbol{u}_h + \boldsymbol{D}_0\boldsymbol{u}_h)$. And finally, the pressure gradient term is integrated using a first order backward Euler scheme. By taking this into consideration, the discretised momentum equation reads:

$$\frac{\boldsymbol{u}_h^{n+1} - \boldsymbol{u}_h^n}{\Delta t} = 3/2\boldsymbol{R}(\boldsymbol{u}_h)^n - 1/2\boldsymbol{R}(\boldsymbol{u}_h)^{n-1} + \boldsymbol{\Omega}_0^{-1}\boldsymbol{M}_0^*\boldsymbol{p}_h^{n+1} \tag{3.35}$$

By introducing the following unique decomposition thanks to the Helmholtz-Hodge theorem, a predicted velocity can be obtained:

$$\boldsymbol{u}_h^p = \boldsymbol{u}_h^n + \Delta t \left(3/2\boldsymbol{R}(\boldsymbol{u}_h)^n - 1/2\boldsymbol{R}(\boldsymbol{u}_h)^{n-1}\right) \tag{3.36}$$

Which is then used to find the discretised velocity field at the current time step.

$$\boldsymbol{u}_h^{n+1} = \boldsymbol{u}_h^p + \Delta t \boldsymbol{\Omega}_0^{-1} \boldsymbol{M}_0^* \boldsymbol{p}_h^{n+1} \tag{3.37}$$

At this point, by applying the divergence operator to each side of the previous equation, providing that $\mathbf{M}_0 \mathbf{u}_h^{n+1} = 0$, a Poisson equation for the pressure can be obtained:

$$\boldsymbol{M}_0 \boldsymbol{\Omega}_0^{-1} \boldsymbol{M}_0^* \boldsymbol{p}_h^{n+1} = -\frac{1}{\Delta t} \boldsymbol{M}_0 \boldsymbol{u}_h^p \tag{3.38}$$

In summary, the steps followed to solve for the discrete velocity and pressure fields at each time step are summarised below:

1. Evaluation of the term $\boldsymbol{R}(\boldsymbol{u}_h)^n$ and $\boldsymbol{R}(\boldsymbol{u}_h)^{n-1}$
2. Evaluation of the predicted velocity with equation 3.36
3. Solving for the pressure with equation 3.38
4. Solving for the velocity at the current time step $n+1$ with equation 3.37

To get a better insight of the fractional step method approach, a visual representation of it is shown in the following figure:

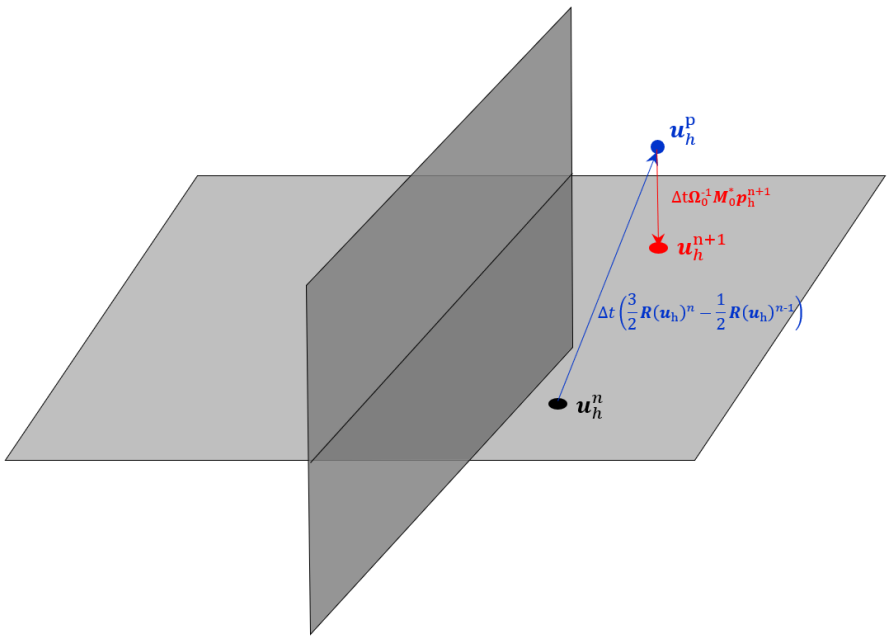

Figure 5: Projection Method representation

As depicted in figure 5, the predicted velocity obtained is a solution of the Navier-Stokes equations without taking into account the incompressibility constraint. Consequently, it is a non divergence-free space. The pressure gradient can be understood as the minimum perturbation

that forces the predictor velocity to be incompressible [16]. In other words, the pressure gradient term projects the predicted velocity to a divergent-free space, as depicted above.

Finally, one last comment needs to be made regarding the computation of the time-step used. The Courant-Friedrichs-Lewy condition is used, as it is a condition for numerical stability that states that, during a certain time-step, the information of the flow, either transported due to diffusion or convection, should only travel to adjacent nodes [17]:

3.4.1 Linear Solvers

In order to solve the Poisson equation, different linear solvers can be considered. In this thesis, the Successive over-relaxation solver (henceforth SOR) and the Conjugate gradient (henceforth CG) were considered. In this section, they are briefly described and their algorithm is shown in pseudocode format. Nevertheless, other solvers such as Jacobi, Gauss-Seidel or Tri-diagonal matrix line-by-line could also be used.

3.4.1.1 Successive over-relaxation solver (SOR)

The successive over-relaxation is an extrapolation of the Gauss-Seidel solver for linear systems of equations, but allowing faster convergence. It uses a weighted average between the previous iterated value and the current one. Considering a system of equations in matrix format:

$$A\boldsymbol{x} = \boldsymbol{b} \tag{3.39}$$

Where A is the coefficients matrix and $\mathbf{x}$ is the vector of unknowns. Matrix A can be decomposed into a diagonal matrix D, one strictly lower triangular matrix L and one strictly upper triangular matrix U, such that:

$$A = D + L + U \tag{3.40}$$

The system of linear equations can be written then as:

$$(D + \omega L)\boldsymbol{x} = \omega\boldsymbol{b} - [\omega U + (\omega - 1)D]\,\boldsymbol{x} \tag{3.41}$$

Where ω is a relaxation factor. The method solves for the new value of the variable $\boldsymbol{x}$ by using the previous iterated value on the right hand side of the equation [18]:

$$\boldsymbol{x}^{k+1} = (D + \omega L)^{-1}(\omega\boldsymbol{b} - [\omega U + (\omega - 1)D]\,\boldsymbol{x}^k) \tag{3.42}$$

Being $\boldsymbol{x}^k$ and $\boldsymbol{x}^{k+1}$ the current and the next approximation of $\boldsymbol{x}$ respectively. Finally, by taking advantage of the fact that the matrix $(D + \omega L)$ is triangular, the unknowns can be computed sequentially as:

$$x_i^{k+1} = (1 - \omega)x_i^k + \frac{\omega}{a_{ii}}\left(b_i - \sum_{j<i} a_{ij}x_j^{k+1} - \sum_{j>i} a_{ij}x_j^k\right), \quad i = 1, 2, ..., n \tag{3.43}$$

The traditional Gauss-Seidel iterative solver is recovered if the relaxation factor ω is set to one. The pseudocode of the SOR algorithm is shown below:

Algorithm 1: Successive Over Relaxation (SOR)

Inputs: A, $\boldsymbol{b}$, ω, δ, $n \leftarrow \text{length}(\boldsymbol{b})$;
Outputs: $\boldsymbol{\phi}$;
Choose an initial estimation ϕ of the solution;
$\varepsilon \leftarrow |A\boldsymbol{\phi} - \boldsymbol{b}|$;
while $\varepsilon > \delta$ **do**
  for $i \leftarrow 1$ **to** n **do**
    $x_i = (1-\omega)\phi_i + \frac{\omega}{a_{ii}}\left(b_i - \sum_{j<i} a_{ij}x_j - \sum_{j>i} a_{ij}\phi_j\right)$
  end
  $\varepsilon \leftarrow \max(|\boldsymbol{\phi} - \boldsymbol{x}|)$;
  $\boldsymbol{\phi} \leftarrow \boldsymbol{x}$;
end

3.4.1.2 Conjugate gradient

The conjugate gradient method is an iterative method that allows to find the solution of a linear system of equations, whose matrix is positive-definite. A good starting point for getting a better understanding of the method is by considering the minimization of the quadratic test function:

$$\phi(\boldsymbol{x}) = \frac{1}{2}\boldsymbol{x}^T A\boldsymbol{x} - \boldsymbol{x}^T\boldsymbol{b} \tag{3.44}$$

Where the vectors $\boldsymbol{x}$ and $\boldsymbol{b} \in \mathbb{R}^n$, and $A \in \mathbb{R}^{n\times n}$, is a matrix which is assumed to be symmetric positive definite (SPD). The minimizer of the previous quadratic function is just the point in which its gradient becomes null, i.e:

$$\nabla\phi(\boldsymbol{x}^*) = A\boldsymbol{x}^* - \boldsymbol{b} = 0 \rightarrow A\boldsymbol{x}^* = \boldsymbol{b} \tag{3.45}$$

Which clearly shows that the solution $\boldsymbol{x}^*$ that solves the system of equations $A\boldsymbol{x} = \boldsymbol{b}$, is also the same solution that minimizes the quadratic function $\phi(\boldsymbol{x})$. Once this is clear, line search methods can be used to iteratively find the minimum of the function. Those methods are based on an iterative procedure given by [19]:

$$\boldsymbol{x}_{k+1} = \boldsymbol{x}_k + \alpha_k\boldsymbol{p}_k \tag{3.46}$$

The idea is to choose an initial position of the function $\boldsymbol{x}_0$ and at each step, move in the search direction $\boldsymbol{p}_k$ a certain step length α_k in order to minimize the function, i.e: $\phi(\boldsymbol{x}_{k+1}) < \phi(\boldsymbol{x}_k)$. Now, suppose that a set of vectors $\boldsymbol{P} = (\boldsymbol{p}_1, \boldsymbol{p}_2, ..., \boldsymbol{p}_n)$, is a set of n mutually conjugate vectors with respect to A, which means that $\boldsymbol{p}_i^T A\boldsymbol{p}_j = 0$ for all $i \neq j$. This means that this n set of vectors P span the whole space $\mathbb{R}^n$. Therefore, the solution $\boldsymbol{x}^*$ that minimizes the function of interest can be expressed as a linear combination of those vectors:

$$\boldsymbol{x}^* = \sum_{i=1}^{n} \alpha_i\boldsymbol{p}_i \rightarrow A\boldsymbol{x}^* = \sum_{i=1}^{n} \alpha_i A\boldsymbol{p}_i \tag{3.47}$$

And by left-multiplying the previous expression by $\boldsymbol{p}_k^T$, one gets:

$$\boldsymbol{p}_k^T A\boldsymbol{x}^* = \sum_{i=1}^{n} \alpha_i \boldsymbol{p}_k^T A\boldsymbol{p}_i \rightarrow \alpha_k = \frac{\boldsymbol{p}_k^T \boldsymbol{b}}{\boldsymbol{p}_k^T A\boldsymbol{p}_k} \tag{3.48}$$

Consequently, the only thing remaining is to find the set of n conjugate directions that allow to compute the coefficients α_k. The first search direction that could be considered could be equal to the negative of the gradient of the function at the first initial guessed solution $\boldsymbol{x}_0$, which, according to equation 3.45, is equal to its residual, i.e:

$$\boldsymbol{r}_0 = \boldsymbol{b} - A\boldsymbol{x}_0 \tag{3.49}$$

And the other vectors of the basis need to be in conjugate directions to the previous. This could be enforced by constructing the next search direction from the current residual and all the previous searched directions. By removing any projection of the current residual in the previous conjugate vector one gets:

$$\boldsymbol{p}_k = \boldsymbol{r}_k - \sum_{i<k} \frac{\boldsymbol{p}_i^T A\boldsymbol{r}_k}{\boldsymbol{p}_i^T A\boldsymbol{p}_i} \boldsymbol{p}_i \tag{3.50}$$

β_{ik} is the projector operator of $\boldsymbol{r}_k$ on $\boldsymbol{p}_i$:

$$\beta_{ik} = \frac{\boldsymbol{p}_i^T A\boldsymbol{r}_k}{\boldsymbol{p}_i^T A\boldsymbol{p}_i} \tag{3.51}$$

However, the search for conjugate directions can be much simplified by considering that it can be easily proved that any residual $\boldsymbol{r}_k$ is orthogonal to all the previous search directions ($\boldsymbol{p}_j^T \boldsymbol{r}_k = 0 \quad \forall \quad \boldsymbol{p}_j \quad j \leqslant k$). As a result, given that the search directions form a basis and the residuals are orthogonal to them, the residuals must also form a basis. Hence, any residual must be orthogonal to the previous ones. According to this, it is clear that:

$$\boldsymbol{r}_{k+1}^T \boldsymbol{r}_k = 0 \rightarrow (\boldsymbol{b} - A\boldsymbol{x}_{k+1})^T \boldsymbol{r}_k = 0 \tag{3.52}$$

And by introducing equation 3.46 into equation 3.52 and rearranging terms, another expression for the step length α_k can be obtained:

$$\alpha_k = \frac{\boldsymbol{r}_k^T \boldsymbol{r}_k}{\boldsymbol{p}_k^T A\boldsymbol{p}_k} \tag{3.53}$$

By making use of the fact that residuals can be used as an orthogonal basis, another expression for the projector β_{ik} can also be obtained [20]. By modifying equation 3.46, it is clear that:

$$\boldsymbol{r}_{k+1} = \boldsymbol{r}_k - \alpha_k A\boldsymbol{p}_k \tag{3.54}$$

By pre-multiplying the previous expression by $\boldsymbol{r}_j^T$, and making use of equations 3.51 and 3.53, the following expression can be found:

$$\beta_{k,j} = \frac{-\boldsymbol{r}_j^T \boldsymbol{r}_{k+1} + \boldsymbol{r}_j^T \boldsymbol{r}_k}{\boldsymbol{r}_k^T \boldsymbol{r}_k} \tag{3.55}$$

Which is a useful expression for $k < j$ in equation 3.50. However, given the orthogonality of the residuals, the previous expression is non-zero only when $j = k + 1$, and thus:

$$\beta_{kk+1} = -\frac{\boldsymbol{r}_{k+1}^T \boldsymbol{r}_{k+1}}{\boldsymbol{r}_k^T \boldsymbol{r}_k^T} \tag{3.56}$$

Combining all this together, the final algorithm is obtained and outlined below:

Algorithm 2: Conjugate Gradient (CG)

Inputs: A, $\boldsymbol{b}$, ω, δ, $n \leftarrow \text{length}(\boldsymbol{b})$;
Outputs: $\boldsymbol{x}$;
Choose an initial estimation $\boldsymbol{x_0}$ of the solution;
$\boldsymbol{r}_0 \leftarrow \boldsymbol{b} - A\boldsymbol{x_0}$;
$\boldsymbol{p}_0 \leftarrow \boldsymbol{r}_0$;
$k \leftarrow 0$;
while $max(|\boldsymbol{r}|) > \delta$ **do**
    $\alpha_k \leftarrow \frac{\boldsymbol{r}_k^T \boldsymbol{r}_k}{\boldsymbol{p}_k^T A \boldsymbol{p}_k}$;
    $\boldsymbol{x}_{k+1} \leftarrow \boldsymbol{x}_k + \alpha_k \boldsymbol{p}_k$;
    $\boldsymbol{r}_{k+1} \leftarrow \boldsymbol{r}_k - \alpha_k A \boldsymbol{p}_k$;
    $\beta_k \leftarrow \frac{\boldsymbol{r}_{k+1}^T \boldsymbol{r}_{k+1}}{\boldsymbol{r}_k^T \boldsymbol{r}_k}$;
    $\boldsymbol{p}_{k+1} \leftarrow \boldsymbol{r}_{k+1} + \beta_k \boldsymbol{p}_k$;
    $k \leftarrow k + 1$;
end

3.5 Verification of the symmetry-preserving scheme

In order to verify the correct implementation of the symmetry-preserving spatial discretization scheme, the correct behaviour of the operators needs to be checked. This implies that the convective operator must be skew-symmetric and the diffusive operator must be positive defined (and symmetric for convenience). Finally, mass conservation is also checked using the divergence operator previously shown. These verifications are done considering a lid-driven cavity problem with the following boundary conditions:

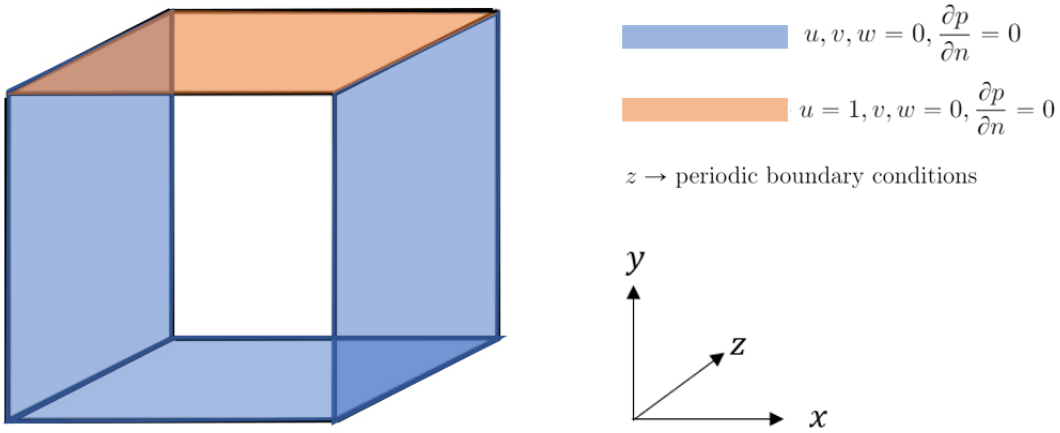

Figure 6: Problem schematization of the driven-cavity problem

On the top wall, a non-slip moving lid is considered, with known tangential velocity. On the left, right and bottom walls, non-slip walls are considered, while on the z direction, periodic boundary conditions are imposed. The behaviour of the operators is checked during the first 200 time-iterations of the problem for a Reynolds number of $Re = 1000$.

First of all, it must be checked the skew-symmetry of the convective term. To do so, it is known that, for a skew-symmetric operator $\boldsymbol{C}_0$:

$$\boldsymbol{a} \cdot \boldsymbol{C}_0 \boldsymbol{b} = (\boldsymbol{a} \cdot \boldsymbol{C}_0 \boldsymbol{b})^* = \boldsymbol{b} \cdot \boldsymbol{C}_0^* \boldsymbol{a} = -\boldsymbol{b} \cdot \boldsymbol{C}_0 \boldsymbol{a} \tag{3.57}$$

Where $\boldsymbol{a}$ and $\boldsymbol{b}$ are two random vectors $\in \mathbb{R}^{3n}$. However, the convective operator must satisfy mass conservation, that is why the velocity field found at each time iteration is used to build the operator $\boldsymbol{C}_0(\boldsymbol{u}_h)$. In this case, if $\boldsymbol{a} = \boldsymbol{b} = \boldsymbol{u}_h$, then it is clear that $\boldsymbol{u}_h \cdot \boldsymbol{C}_0 (\boldsymbol{u}_h) \boldsymbol{u}_h = 0$. This operation is checked during the first 200 time iterations of the lid-driven cavity problem previously described. The absolute value of the result is shown in the following figure:

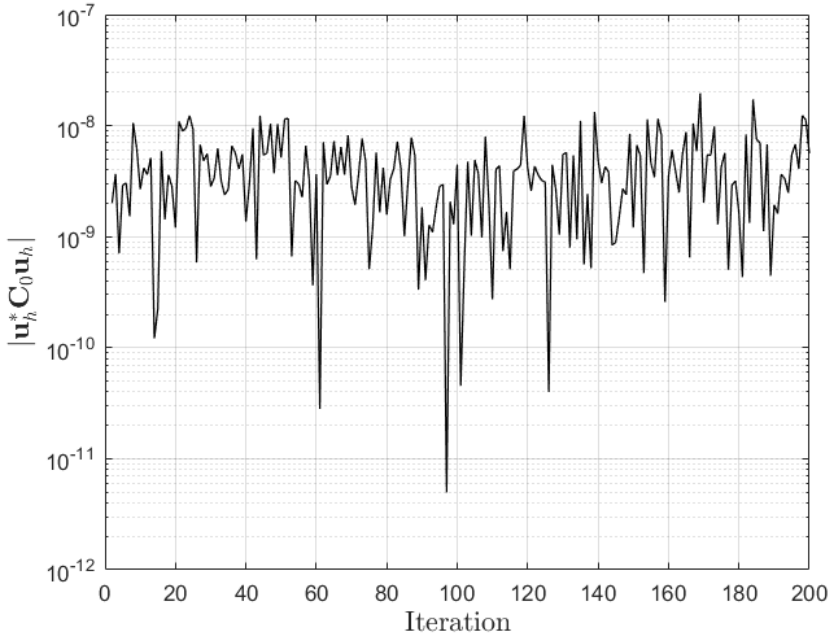

Figure 7: Results of the skew-symmetry test for the convective operator during the first 200 time iterations of the lid-driven cavity problem for $Re = 1000$

As it can be seen, the average value obtained during all the iterations tested is of $4.3e-09$, proving the correct discretization of the convective operator.

The next step is to check the symmetry of the diffusive operator. To do so, it is known that for a symmetric operator $\boldsymbol{D}_0$:

$$\boldsymbol{a_0} \cdot \boldsymbol{D}_0 \boldsymbol{b_0} = (\boldsymbol{a} \cdot \boldsymbol{D}_0 \boldsymbol{b_0})^* = \boldsymbol{b} \cdot \boldsymbol{D}_0^* \boldsymbol{a_0} = \boldsymbol{b_0} \cdot \boldsymbol{D}_0 \boldsymbol{a_0} \tag{3.58}$$

Where $\boldsymbol{a_0}$ and $\boldsymbol{b_0}$ are to random vectors $\in \mathbb{R}^{3n}$. In this case, the operator $\boldsymbol{D}_0$ would be the diffusive operator, which, unlike the convective operator, does not have to satisfy mass conservation or any other constraint. The diffusive operator is distributed into three minor operators, one for each staggered mesh, according to $\boldsymbol{D}_0 = diag(\boldsymbol{D}_0^u, \boldsymbol{D}_0^v, \boldsymbol{D}_0^w)$. According to this, to check the symmetry of the diffusive operator, the following operation is computed, which should give a value of 0:

$$\boldsymbol{a}^* \boldsymbol{D}_0^u \boldsymbol{u} - \boldsymbol{u}^* \boldsymbol{D}_0^u \boldsymbol{a} + \boldsymbol{b}^* \boldsymbol{D}_0^v \boldsymbol{v} - \boldsymbol{v}^* \boldsymbol{D}_0^v \boldsymbol{b} + \boldsymbol{c}^* \boldsymbol{D}_0^w \boldsymbol{w} - \boldsymbol{w}^* \boldsymbol{D}_0^w \boldsymbol{c} \tag{3.59}$$

Where $\boldsymbol{a}$, $\boldsymbol{b}$ and $\boldsymbol{c}$ are three random generated vectors $\in \mathbb{R}^n$, while $\boldsymbol{u}$, $\boldsymbol{v}$ and $\boldsymbol{w}$ are the x, y and z components of the velocity field. The absolute value of expression 3.59 is graphed during the first 200 time iterations of the lid-driven cavity problem, obtaining a mean value of 2.95e-15, proving that the operator is symmetric and thus, correctly discretized.

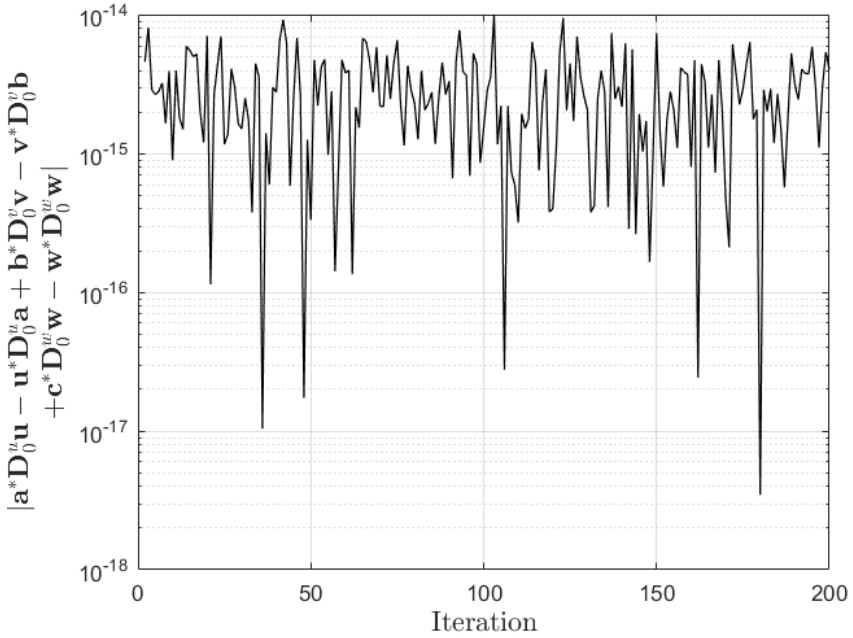

Figure 8: Results of the symmetry test for the diffusive operator during the first 200 time iterations of the lid-driven cavity problem for $Re = 1000$

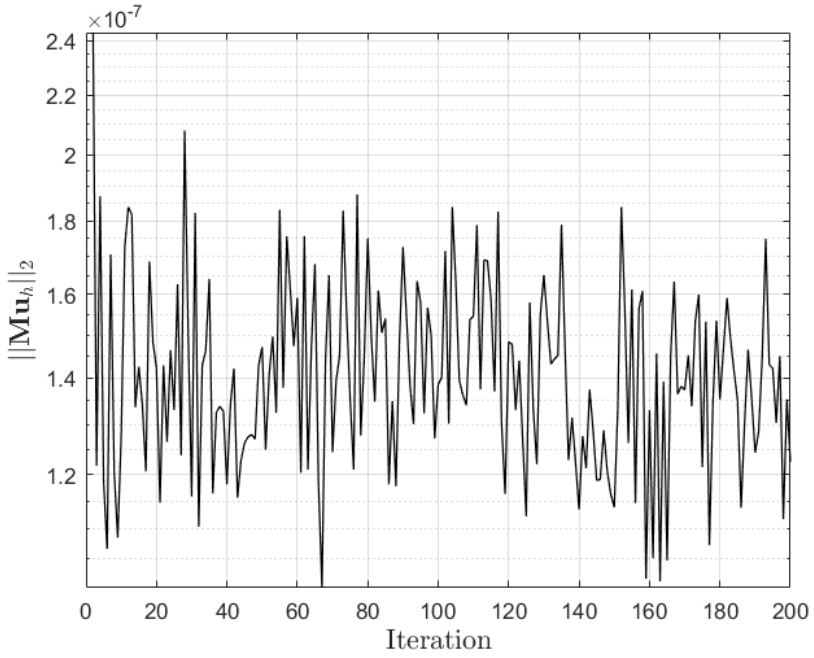

Figure 9: Results of the test for the divergence operator during the first 200 time iterations of the lid-driven cavity problem for $Re = 1000$

Finally, the last operator that needs to be checked is the divergence operator by checking mass conservation. The operator is applied to the main grid, like the one sketched in figure 3, giving the following expression, which should also be very close to 0:

$$\boldsymbol{M}_0 \boldsymbol{u}_h \tag{3.60}$$

In this case, the result is a vector giving the net mass flux through each control volume. In order to quantify the result, the L2 norm is applied to the result vector of expression 3.60 during the first 200 time iterations of the problem, obtaining a mean value of 1.4e-07 as shown in figure 9, which again proves the correct discretization of the divergence operator.

4 Energy cascade

Richardson (1922), firstly introduced the idea of the energy cascade in turbulent flows. In his concept, he considered turbulence to be composed of eddies of different sizes. The concept behind his idea is that kinetic energy is introduced at the largest scales of the flow (i.e largest eddies). Largest eddies are unstable, and thus, they break up, transferring energy to smaller eddies (by inviscid processes), whose, at the same time, also break up into smaller ones. At sufficiently smaller scales, molecular viscosity becomes dominant, and energy is dissipated due to viscous dissipation [21]. This process can be easily visualised in the following figure:

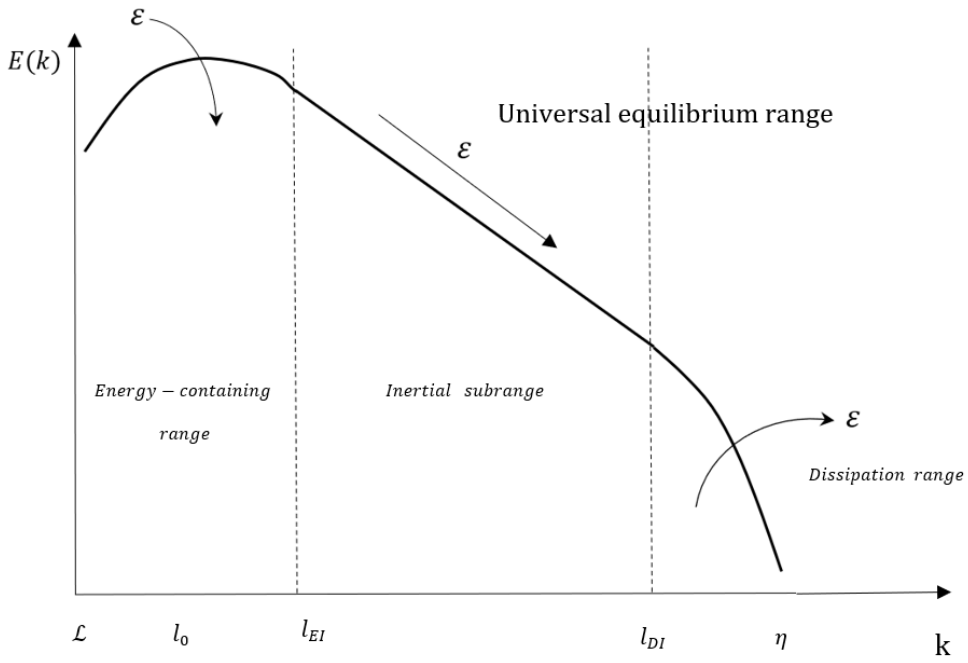

Figure 10: Energy cascade concept

In figure 10, the energy spectrum of the different turbulent scales is plotted. As it can be easily seen, at low wave-numbers energy is introduced into the system. Through the inertial range, energy is transported from larger eddies (lower wave-numbers), to smaller eddies (higher wave-numbers), until, eventually, energy is dissipated at sufficiently small scales. The largest eddies are characterised by the lengthscale l_0, which is comparable to the flow scale $\mathcal{L}$, and with characteristic velocity $u_0 \equiv u(l_0)$, which is similar to the reference velocity $\mathcal{U}$; having a Reynolds number of $Re_0 \equiv u_0 l_0/\nu$, which is large enough so that the direct effect of viscosity is negligible. Those largest eddies have energy of order u_0^2 and timescale $\tau_0 = l_0/u_0$. Consequently, the rate of energy dissipation (ε) is supposed to scale as $u_0^2/\tau_0 = u_0^3/l_0$, which is independent of the viscosity ν (only for high Reynolds numbers).

However, some aspects still need to be considered, such as determining the size of the smallest eddies that are responsible for dissipating the energy. This and other questions are answered

through three hypotheses stated by Kolmogorov.

4.1 Kolmogorov's hypothesis of local isotropy

The first hypothesis states that larger scales of the flow are anisotropic and affected by the boundary conditions of the flow. However, as energy is transferred to lower scales in a chaotic manner, the directional biases of the large eddies is lost, resulting in smaller scales of the turbulent flow being statistically isotropic, and, in a sense, universal. Kolmogorov introduced the lengthscale l_{EI}, which is the limit between the large (and anisotropic) eddies ($l > l_{EI}$), and the smaller (and isotropic) ones ($l < l_{EI}$).

4.2 Kolmogorov's first similarity hypothesis

With Kolmogorov's hypothesis of local isotropy, there is still to be determined the parameters on which the universal state ($l < l_{EI}$) depends. The hypothesis is that the important parameters are the rate at which the smaller scales receive energy from the larger scales (τ_{EI}) and the kinematic viscosity (ν). The dissipation rate ε can be considered to be nearly equal to the energy transfer rate τ_{EI}. Consequently, for turbulent flows with high enough Reynolds number, smaller turbulent scales which $l < l_{EI}$ have statisticals with universal form which are only determined by ν and ε. Given those two parameters, unique length, velocity and time scales can be computed (i.e, Kolmogorov's scales), for the universal equilibrium range:

$$\eta \equiv (\nu^3/\varepsilon)^{1/4} \tag{4.1}$$

$$u_\eta \equiv (\varepsilon\nu)^{1/4} \tag{4.2}$$

$$\tau_\eta = (\nu/\varepsilon)^{1/2} \tag{4.3}$$

It is straightforward to prove that, the Reynolds number based on Kolmogorov's scales is:

$$\frac{\eta u_n}{\nu} = 1 \tag{4.4}$$

which is consistent with the fact that dissipation is effective only for low Reynolds numbers. Consequently, the kinematic viscosity is equal to $\nu = u_\eta \eta$. Additionally, the dissipation rate is given by:

$$\varepsilon = \nu(u_\eta/\eta)^2 = \nu/\tau_\eta^2 \tag{4.5}$$

The ratio between the smallest and largest scales can be easily found. As the dissipation rate is given by:

$$\varepsilon = \frac{u_0^3}{l_0} = \frac{u_\eta^3}{\eta} \rightarrow \left(\frac{u_0}{u_\eta}\right)^3 = \frac{l_0}{\eta} \tag{4.6}$$

By the definition of the Reynolds number and, remembering that $\nu = \eta u_\eta$:

$$Re = \frac{u_0 l_0}{\nu} = \frac{l_0}{\eta}\frac{u_0}{u_\eta} = \left(\frac{u_0}{u_\eta}\right)^4 \tag{4.7}$$

Consequently, the relation between the velocity of the smaller and the larger scales can be written as:

$$\frac{u_\eta}{u_0} = Re^{-1/4} \tag{4.8}$$

The ratio between the size of the smallest eddies and the largest one can be computed as:

$$\frac{\eta}{l_0} = \frac{u_0}{u_\eta}\frac{1}{Re} = \left(\frac{u_\eta}{u_0}\right)^3 = Re^{-3/4} \tag{4.9}$$

And finally, the relation between the time scales can be computed as:

$$\frac{\tau_\eta}{\tau_0} = \frac{\eta/u_\eta}{l_0/u_0} = \frac{\eta}{l_0}\frac{u_0}{u_\eta} = Re^{-1/2} \tag{4.10}$$

4.3 Kolmogorov's second similarity hypothesis

In the second similarity hypothesis proposed, Kolmogorov states that there is a range of turbulent scales l, that are much smaller compared to the reference dimension l_0, yet a lot larger than the Kolmogorov's length scale η ($l_0 \gg l \gg \eta$). In this range, turbulent structures are big enough and with a high Reynolds number $lu(l)/\nu$, which implies that they are still not affected by viscosity. This range, which is called the inertial subrange, is characterised by a universal form, solely determined by the energy dissipation rate ε, and independent of the kinematic viscosity ν. The inertial subrange starts at a characteristic lengthscale of l_{EI}, which determines the start of the universal equilibrium range and the inertial subrange; and ends at a lengthscale l_{DI}, which determines the start of the dissipation range.

The lengthscale, timescale and velocity scale can not be created solely with the energy dissipation rate ε. Hence, an eddy size l inside the inertial subrange needs to be considered as well to define those scales:

$$u(l) = (\varepsilon l)^{1/3} = u_\eta(l/\eta)^{1/3} \sim u_0(l/l_0)^{1/3} \tag{4.11}$$

$$\tau(l) = (l^2/\varepsilon)^{1/3} = \tau_\eta(l/\eta)^{2/3} \sim \tau_0(l/l_0)^{2/3} \tag{4.12}$$

It can be easily seen that both the velocity and time scales $u(l)$ and $\tau(l)$ decrease as l decreases. An important parameter in the energy cascade concept is the rate at which energy is being transferred from eddies with a characteristic size larger than l to smaller eddies with size smaller than l - denoted by $\tau(l)$. Considering that the transfer of energy is mainly due to eddies of a characteristic size l, then it becomes clear that $\tau(l)$ is of the order of $u(l)^2/\tau(l)$. But, according to equations 4.11 and 4.12, it can be seen that $\tau(l)$ for l inside the inertial subrange, is independent of l as:

$$u(l)^2/\tau(l) = \varepsilon \tag{4.13}$$

The inertial subrange, dissipation range, and the total energy spectrum of turbulent flows can be easily understood by examining figuer 10.

4.4 Energy spectrum

An important statistic in turbulence is the two-point correlation, which allows to obtain information regarding the spatial structure of a random field:

$$\boldsymbol{R_{ij}}(\boldsymbol{r}, \boldsymbol{x}, t) \equiv \langle u_i(\boldsymbol{x}, t) u_j(\boldsymbol{x} + \boldsymbol{r}, t) \rangle \tag{4.14}$$

If homogeneous turbulence is considered, the two-point correlation is then independent of $\boldsymbol{x}$, and the information can be expressed by using the wavenumber spectrum. With this, the velocity spectrum tensor $\Phi_{ij}(\boldsymbol{k}, t)$ can be defined as the Fourier transform of the two-point correlation [21]:

$$\boldsymbol{\Phi_{ij}}(\boldsymbol{k}, t) = \frac{1}{(2\pi)^3} \iiint_{-\infty}^{\infty} e^{-i\boldsymbol{k}\cdot\boldsymbol{r}} \boldsymbol{R_{ij}}(\boldsymbol{r}, t) \mathrm{d}\boldsymbol{r} \tag{4.15}$$

And the inverse Fourier transform can be defined as:

$$\boldsymbol{R_{ij}}(\boldsymbol{r}, t) = \iiint_{-\infty}^{\infty} e^{i\boldsymbol{k}\cdot\boldsymbol{r}} \boldsymbol{\Phi_{ij}}(\boldsymbol{k}, t) \mathrm{d}\boldsymbol{k} \tag{4.16}$$

It is clear that, by setting $\boldsymbol{r} = \boldsymbol{0}$, the velocity spectrum tensor term $\boldsymbol{\Phi_{ij}}(\boldsymbol{k}, t)$ is equal to the the contribution to the covariance $\langle u_i u_j \rangle$ that the velocity modes with wavenumber $\boldsymbol{k}$ have. However, another parameter of importance is the energy spectrum function, which can be computed as:

$$E(k, t) \equiv \iiint_{-\infty}^{\infty} \frac{1}{2} \boldsymbol{\Phi_{ii}}(\boldsymbol{k}, t) \delta(|\boldsymbol{k}| - k) d\boldsymbol{k} \tag{4.17}$$

This can be interpreted as the velocity spectrum tensor $\Phi_{ij}(\boldsymbol{k}, t)$ without accounting for all the directional information. By integrating $E(k, t)$ over all scalar wavenumber, one gets:

$$\int_0^{\infty} E(k, t) dk = \frac{1}{2} R_{ii}(0, t) = \frac{1}{2} \langle u_i u_i \rangle \tag{4.18}$$

Which is equal to the turbulent kinetic energy of all modes with $k < |\boldsymbol{k}| < k + dk$. With all of this, it is still to be determined how the turbulent kinetic energy is distributed among the eddies with different sizes. This can be done by using simple dimensional analysis:

$$[k] = [L^{-1}] \quad [\varepsilon] = [L^2 T^{-3}] \quad [E_T] = [L^2 T^{-2}] \quad [E(k)] = [L^3 T^{-2}] \tag{4.19}$$

Given that in the inertial subrange will only be a function of ε and k, it is clear that:

$$E(k) \propto \varepsilon^a k^b \tag{4.20}$$

And according to the dimensional analysis previously done:

$$[L^3 T^{-2}] \propto [L^2 T^{-3}]^a [L^{-1}]^b \rightarrow [L^3 T^{-2}] \propto [L^{2a-b} T^{-3a}] \tag{4.21}$$

Yielding $a = 2/3$ and $b = -5/3$. Which allows to write the energy spectrum equation for the inertial subrange part as:

$$E(k) = C_k \varepsilon^{2/3} k^{-5/3} \tag{4.22}$$

Where C_k is the universal Kolmogorov constant.

5 Mean flow equations

Given the chaotic nature of the Navier-Stokes equations in turbulent regime, it is common to tackle the problem by averaging the equations and resolving for time-averaged values. Due to the fact that variables in turbulent flows need to be treated as random variables, certain definitions need to be given beforehand.

5.1 Statistical description of turbulent flows

Let U be a random variable that is a function of space and time, $(U(x,t))$, either velocity, pressure, temperature,... whose cummulative distribution function (F), is defined as the probability that a variable has to be less than a value V. For instance, the following equation expresses the probability (P), that the variable u is smaller than V:

$$F(V) = P(u < V) \tag{5.1}$$

The cummulative distribution function satisfies three properties:

$$F(-\infty) = 0 \tag{5.2}$$

$$F(\infty) = 1 \tag{5.3}$$

$$F(V_b) \geqslant F(V_a) \quad for \quad V_b > V_a \tag{5.4}$$

The probability density function can be easily defined as the derivative of the cummulative distribution function:

$$f(V) \equiv \frac{dF(V)}{dV} \tag{5.5}$$

Which has the following properties:

$$f(V) \geqslant 0 \tag{5.6}$$

$$\int_{-\infty}^{\infty} f(V)dV = 1 \tag{5.7}$$

$$f(-\infty) = f(\infty) = 0 \tag{5.8}$$

With the previous definition, the probability that a random variables lays between a certain interval is equal to the integral of the probability density function over that interval:

$$P\{V_a \leqslant U < V_b\} = F(V_b) - F(V_a) = \int_{V_a}^{V_b} f(V)dV \tag{5.9}$$

The mean or expectation of a random variable U, that could be any measurable variable in turbulent flow, can be computed as:

$$\langle U \rangle \equiv \int_{\infty}^{\infty} V f(V) dV \tag{5.10}$$

The fluctuation (u') in the random variable U is easily defined as:

$$u' \equiv U - \langle U \rangle \tag{5.11}$$

The variance of the variable U is defined as the mean of the fluctuations squared:

$$var(U) \equiv \langle u'^2 \rangle = \int_{-\infty}^{\infty} (V - \langle U \rangle)^2 f(V) dV \tag{5.12}$$

While the standard deviation is defined as the square root of the variance:

$$sdev(U) = \langle u'^2 \rangle^{1/2} \tag{5.13}$$

Two random variables can be either studied separately or together to see if there is any relation between both. If the latter is done, the cummulative distribution function of the joint random variables is defined according to:

$$F_{12}(V_1, V_2) \equiv P(U_1 < V_1, U_2 < V_2) \tag{5.14}$$

The joint probability density function is defined by:

$$f_{12}(V_1, V_2) \equiv \frac{\partial^2}{\partial V_1 \partial V_2} F_{12}(V_1, V_2) \tag{5.15}$$

The joint variability of two random variables can be computed with the covariance:

$$\operatorname{cov}(U_1, U_2) =< u_1' u_2' >= \int_{-\infty}^{\infty} \int_{-\infty}^{\infty} (V_1 - \langle U_1 \rangle)(V_2 - \langle U_2 \rangle) f_{12}(V_1, V_2) dV_1 dV_2 \tag{5.16}$$

And the correlation coefficient can be easily computed as:

$$\begin{aligned} &\rho_{12} \equiv \frac{\langle u_1' u_2' \rangle}{\sqrt{\langle u_1'^2 \rangle \langle u_2'^2 \rangle}} \\ &-1 \leqslant \rho_{12} \leqslant 1 \end{aligned} \tag{5.17}$$

All the previous statistics have been computed based on the probability density function. However, this function is not known for the computation of turbulent flows. Thus, the mean or expected variable of the velocity, pressure, temperature,... can not be evaluated with expression 5.10. An option to estimate the mean value and any other statistics could be to set a large number of experiments under identical conditions (i.e, an ensemble), and average the results obtained (i.e, an ensemble average):

$$\langle U \rangle_N \equiv \frac{1}{N} \sum_{i=1}^{N} U^i(t) \tag{5.18}$$

It can be easily proved that

$$\langle \langle U \rangle_N \rangle = \langle U \rangle \tag{5.19}$$

Additionally, according to the definition of the ensemble average, it is straightforward to show that the operation of differentiation and integration commute with the operation of ensemble averaging, i.e:

$$\left\langle \frac{\partial U}{\partial t} \right\rangle_N = \frac{\partial \langle U \rangle_N}{\partial t} \tag{5.20}$$

$$\left\langle \int_a^b U dt \right\rangle_N = \int_a^b \langle U \rangle_N dt \tag{5.21}$$

Being the previous equalities valid not only for time-dependant variables, but also for spatial-dependent ones. Nevertheless, it is clar that this approach is not feasible to compute the statistics of turbulent flows, as each simulation can be extremely time-consuming. To solve this problem, we can make use of the definition of statistically stationary flows (SS) and statistically homogeneous flows (SH). In a statistically stationary flow, all statistics are invariant with respect to a time shift.

An example of a statistically stationary flow can be found in figure 11.

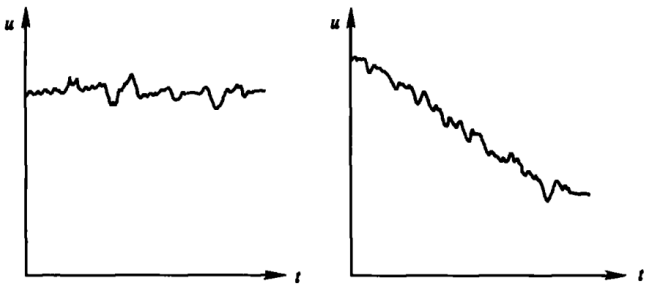

Figure 11: Example of a statistically stationary time series (left) and a statistically nonstationary time series (right). Extracted from [2]

It is clear how the time series on the left shows a statistically stationary time series, in contrast with the time series on the right of figure 11. In statistically homogeneous flows, the statistics are invariant with respect to a position shift in any direction. If the flow field is statistically stationary, its mean value is a function of the position x and can be easily computed as:

$$\langle U(t,x) \rangle_T = \frac{1}{\Delta t} \int_{t_0}^{t_0+\Delta t} U(t')dt' \tag{5.22}$$

If the flow field is statistically homogeneous, its mean or expected value is a scalar function of time:

$$\langle U(t,x) \rangle_V = \frac{1}{V} \int_V U(x,t)dv \tag{5.23}$$

Nevertheless, statistically homogeneous flows are not common in engineering problems.

5.2 Reynolds-Averaged Navier-Stokes equations

Fully turbulent flows can be very difficult and time-consuming to solve, as there is a large amount of length and time scales to be resolved, as it has been previously seen. Nevertheless, in engineering there is usually not much interest in resolving all the flow scales, but rather, in finding the mean flow properties such as mean velocity or temperature. Consequently, by time-averaging the Navier-Stokes equations, the mean flow properties can be obtained.

Recalling the general form of the incompressible Navier-Stokes equations (momentum and mass conservation), neglecting body forces and assuming a Newtonian fluid with constant viscosity:

$$\rho\left(\frac{\partial u_i}{\partial t}+\frac{\partial}{\partial x_j}\left(u_i u_j\right)\right)=-\frac{\partial p}{\partial x_i}+\mu\frac{\partial^2 u_i}{\partial x_j \partial x_j} \tag{5.24}$$

$$\frac{\partial u_i}{\partial x_i}=0 \tag{5.25}$$

The dependent variables (velocity and pressure) are decomposed into their mean and fluctuating part:

$$u_i=\langle u_i\rangle+u_i' \tag{5.26}$$

$$p=\langle p\rangle+p' \tag{5.27}$$

Considering the following properties of the average operator on two random variables ψ and ϕ:

- The average of the fluctuations is zero:
  $\langle\phi\rangle=\langle\langle\phi\rangle+\phi'\rangle=\langle\phi\rangle+\langle\phi'\rangle\rightarrow\langle\phi'\rangle=0$
- Average of the product of two random variables:
  $\langle\psi\phi\rangle=\langle(\langle\phi\rangle+\phi')(\langle\psi\rangle+\psi')\rangle=\langle\langle\phi\rangle\langle\psi\rangle+\langle\phi\rangle\psi'+\phi'\langle\psi\rangle+\phi'\psi'\rangle=\langle\phi\rangle\langle\psi\rangle+\langle\phi'\psi'\rangle$
- Commutation with the operation of differentiation (as previously shown):
  $\left\langle\frac{\partial\phi}{\partial t}\right\rangle=\frac{\partial\langle\phi\rangle}{\partial t}\quad\left\langle\frac{\partial\phi}{\partial x_i}\right\rangle=\frac{\partial\langle\phi\rangle}{\partial x_i}$

Substituting equations 5.26 and 5.27 into 5.24 and 5.25 one gets:

$$\frac{\partial\langle u_i\rangle}{\partial x_i}=0 \tag{5.28}$$

$$\rho\left(\frac{\partial\langle u_i\rangle}{\partial t}+\frac{\partial}{\partial x_j}(\langle u_i u_j\rangle)\right)=-\frac{\partial\langle p\rangle}{\partial x_i}+\mu\frac{\partial^2\langle u_i\rangle}{\partial x_j\partial x_j} \tag{5.29}$$

As it can be seen, the continuity equation shows a null divergence of the mean velocity field. The averaged momentum equation is basically the same but accounting for mean values, except for the convective term, which needs to be considered separately:

$$\langle u_i u_j \rangle = \langle (\langle u_i \rangle + u_i')(\langle u_j \rangle + u_j') \rangle = \langle \langle u_i \rangle \langle u_j \rangle \rangle + \langle \langle u_i \rangle u_j' \rangle + \langle u_i' \langle u_j \rangle \rangle + \langle u_i' u_j' \rangle = \langle u_i \rangle \langle u_j \rangle + \langle u_i' u_j' \rangle \tag{5.30}$$

Which, substituting into the previous equations, yields the following:

$$\rho \left(\frac{\partial \langle u_i \rangle}{\partial t} + \frac{\partial}{\partial x_j} (\langle u_i \rangle \langle u_j \rangle) \right) = -\frac{\partial \langle p \rangle}{\partial x_i} + \mu \frac{\partial^2 \langle u_i \rangle}{\partial x_j \partial x_j} - \rho \frac{\partial}{\partial x_j} (\langle u_i' u_j' \rangle) \tag{5.31}$$

The averaged momentum equation can be re-written by expressing the convective term in non-conservative form, and replacing the term $\tau_{ij}^R = -\rho \langle u_i' u_j' \rangle$. With this, the RANS equations are obtained:

$$\frac{\partial \langle u_i \rangle}{\partial x_i} = 0 \tag{5.32}$$

$$\rho \left(\frac{\partial \langle u_i \rangle}{\partial t} + \langle u_j \rangle \frac{\partial \langle u_i \rangle}{\partial x_j} \right) = -\frac{\partial \langle p \rangle}{\partial x_i} + \mu \frac{\partial^2 \langle u_i \rangle}{\partial x_j \partial x_j} + \frac{\partial \tau_{ij}^R}{\partial x_j} \tag{5.33}$$

The term τ_{ij}^R is known as the Reynolds-stress term, which is added up to the mean stresses to account for the turbulent fluctuations. This is a symmetric, positive semi-definite matrix, whose diagonal components are the normal stresses, and the off-diagonal terms are shear stresses:

$$\tau_{ij}^R = -\rho \begin{bmatrix} \langle u'^2 \rangle & \langle u'v' \rangle & \langle u'w' \rangle \\ \langle v'u' \rangle & \langle v'^2 \rangle & \langle v'w' \rangle \\ \langle w'u' \rangle & \langle wv'^2 \rangle & \langle w'^2 \rangle \end{bmatrix} \tag{5.34}$$

The system of equations 5.32 and 5.33 is not a closed system, due to the fact there are a total of 10 unknowns: the three components of the mean velocity $\langle u_i \rangle$, the mean pressure $\langle p \rangle$, and six additional Reynolds stress terms $\langle u'^2 \rangle$, $\langle v'^2 \rangle$, $\langle w'^2 \rangle$, $\langle u'v' \rangle$, $\langle u'w' \rangle$ and $\langle v'u' \rangle$; but only 4 equations. Consequently, the closure of the problem consists on expressing the six extra additional Reynolds stress components as a function of the mean velocity components and/or any other variables.

5.3 Classical turbulence models

As stated previously, in order to close the problem, turbulence models are needed to express the Reynolds stress terms in the RANS equations. In general, it is seek an accurate, yet simple and computationally economical to run turbulence model. RANS turbulence models are typically classified depending on the number of extra transport equations that need to be solved to find the unknowns needed to solve the problem:

No. of extra transport equations	Turbulence model
Zero	Mixing length model
One	Spalart-Allmaras
Two	$k-\varepsilon$ $k-\omega$ Algebraic stress model
Seven	Reynolds stress model

Table 1: Classical Turbulence models according to the number of extra transport equations needed

5.3.1 Eddy-viscosity model

In 1877, Joseph Valentin Boussinesq tackled the closure problem by introducing the concept of eddy viscosity. Boussinesq assumed, that given the similarity between the Reynolds stress term and the the stresses caused by viscosity effects, the former should be proportional to the mean velocity gradients. Given the fact that turbulent stresses increase when mean rate of deformation also increase [6], Boussinesq stated that the Reynolds stress term should be proportional to the mean strain rate:

$$\tau_{ij}^{R} = -\rho\langle u_i' u_j' \rangle = \mu_t \left(\frac{\partial \langle u_i \rangle}{\partial x_j} + \frac{\partial \langle u_j \rangle}{\partial x_i} \right) \tag{5.35}$$

In which a proportionality constant μ_t has been used. Nevertheless, the previous expression is not consistent and thus, should be corrected due to the following. Given the definition of the turbulent kinetic energy $k(x,t)$:

$$k \equiv \frac{1}{2}\langle u_i' u_i' \rangle = \frac{1}{2}(\langle u'^2 \rangle + \langle v'^2 \rangle + \langle w'^2 \rangle) \tag{5.36}$$

It is clear that the sum of the normal turbulent stresses should give:

$$-\rho(\langle u'^2 \rangle + \langle v'^2 \rangle + \langle w'^2 \rangle) = -2\rho k \tag{5.37}$$

However, according to the proposed relation 5.35, the sum of the normal turbulent stresses gives a different result:

$$-2\rho k \neq 2\mu_t \left(\frac{\partial \langle u \rangle}{\partial x} + \frac{\partial \langle v \rangle}{\partial y} + \frac{\partial \langle w \rangle}{\partial z} \right) \tag{5.38}$$

Which is equal to 0 for incompressible flow. Consequently, to correct expression 5.35, 1/3 of the error is subtracted from each of the normal components, i.e:

$$-\rho\langle u'^2 \rangle = 2\mu_t \left(\frac{\partial \langle u \rangle}{\partial x} - \frac{1}{3}\left(\frac{\partial \langle u \rangle}{\partial x} + \frac{\partial \langle v \rangle}{\partial y} + \frac{\partial \langle w \rangle}{\partial z} \right) \right) - \frac{1}{3}(2\rho k) \tag{5.39}$$

$$-\rho\langle v'^2 \rangle = 2\mu_t \left(\frac{\partial \langle v \rangle}{\partial y} - \frac{1}{3}\left(\frac{\partial \langle u \rangle}{\partial x} + \frac{\partial \langle v \rangle}{\partial y} + \frac{\partial \langle w \rangle}{\partial z} \right) \right) - \frac{1}{3}(2\rho k) \tag{5.40}$$

$$-\rho\langle w'^2\rangle = 2\mu_t\left(\frac{\partial\langle w\rangle}{\partial z} - \frac{1}{3}\left(\frac{\partial\langle u\rangle}{\partial x} + \frac{\partial\langle v\rangle}{\partial y} + \frac{\partial\langle w\rangle}{\partial z}\right)\right) - \frac{1}{3}(2\rho k) \tag{5.41}$$

Consequently, the final Boussinesq approximation can be written in a more compact form as:

$$\tau_{ij}^R = -\rho\langle u_i' u_j'\rangle = \mu_t\left(\frac{\partial\langle u_i\rangle}{\partial x_j} + \frac{\partial\langle u_j\rangle}{\partial x_i} - \frac{2}{3}\frac{\partial\langle u_k\rangle}{\partial x_k}\delta_{ij}\right) - \frac{2}{3}\rho k\delta_{ij} \tag{5.42}$$

Which reduces to the following for incompressible flow:

$$\tau_{ij}^R = -\rho\langle u_i' u_j'\rangle = \mu_t\left(\frac{\partial\langle u_i\rangle}{\partial x_j} + \frac{\partial\langle u_j\rangle}{\partial x_i}\right) - \frac{2}{3}\rho k\delta_{ij} \tag{5.43}$$

Finally, substituting the incompressible form of the Boussinesq approximation in equation 5.33, the following is obtained:

$$\rho\left(\frac{\partial\langle u_i\rangle}{\partial t} + \langle u_j\rangle\frac{\partial\langle u_i\rangle}{\partial x_j}\right) = -\frac{\partial(\langle p\rangle + 2/3\rho k)}{\partial x_i} + (\mu + \mu_t)\frac{\partial^2\langle u_i\rangle}{\partial x_j\partial x_j} \tag{5.44}$$

Where the term $\langle p\rangle + 2/3\rho k$ is a corrected pressure term that includes the turbulent kinetic energy. It is important to notice that by using Boussinesq's approximation, the number of unknowns in the Reynold's stress term has been reduced from 6 terms to only 2 (the turbulent kinetic energy k and the turbulent viscosity μ_t). The reader should be aware of the difference between the dynamic viscosity μ and the turbulent viscosity μ_t. While the former is a physical property of the fluid, the latter is an artificial constant that does not depend on the fluid, but rather on the flow characteristics. The eddy viscosity controls the strength of the extra diffusion added by the turbulent stresses. Consequently, being an artificial parameter, μ_t must be modelled somehow.

Finally, it is important to notice that with Boussinesq's approximation, the turbulent transport of momentum is assumed to be proportional to the mean gradients of the momentum per unit of mass (i.e, velocity). Consequently, in a similar way, turbulent transport of any scalar is taken to be proportional to the gradient of the mean value of the quantity that is being transported, i.e:

$$-\rho\langle u_i'\varphi'\rangle = \Gamma_t\frac{\partial\Phi}{\partial x_i} \tag{5.45}$$

Where Γ_t is the turbulent or eddy diffusivity. The Prandtl/Schmidt number can be defined as the ratio between the turbulent eddy viscosity and the turbulent eddy diffusivity of a certain quantity:

$$\sigma_t = \frac{\mu_t}{\Gamma_t} \tag{5.46}$$

Values of σ_t are around unity according to Reynolds analogy, which states that both μ_t and Γ_t are comparable, due to the fact that the turbulent transport of an quantity is due to the same mechanism - eddy mixing [22].

5.3.1.1 Mixing length model

The mixing length model, also known as the Prandtl's mixing length model, is one of the subgroups of turbulence models included inside the eddy-viscosity models. It is based on the fact that given the units of the dynamic turbulent or eddy viscosity μ_t $(kgm^{-1}s^{-1})$; this could be written as the product of one velocity scale and one length scale according to:

$$\mu_t = \mathrm{C}\rho\,\vartheta l_m \tag{5.47}$$

Where C is a dimensionless constant of proportionality. Considering a blob of fluid which is moved in the vertical direction due to a fluctuating velocity v'. The blob of turbulent flow moves a distance l_m, known as the mixing length, which is analogous to the mean free path in molecular dynamics [23]. When the blob of flow reaches its new position, the fluctuation in the streamwise velocity can be approximated to be the difference between its original velocity and the one of its surroundings in the new position, i.e:

$$u' \sim \left(\langle u\rangle + \frac{\partial\langle u\rangle}{\partial y} l_m\right) - \langle u\rangle = \frac{\partial\langle u\rangle}{\partial y} l_m \tag{5.48}$$

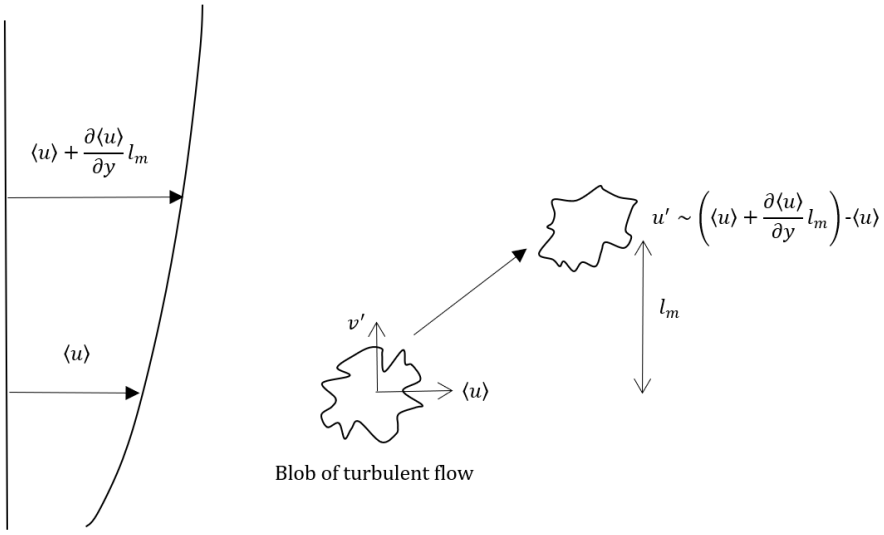

Figure 12: Prandtl's mixing length theory

The modulus of this fluctuating velocity is taken as the characteristic velocity in equation 5.47:

$$\vartheta = |u'| = \left|\frac{\partial\langle u\rangle}{\partial y}\right| l_m \tag{5.49}$$

The absolute value is taken to ensure that the characteristic velocity is always positive. Consequently. Substituting equation 5.49 into equation 5.47, the following is obtained:

$$\mu_t = C\rho\left|\frac{\partial\langle u\rangle}{\partial y}\right| l_m^2 \tag{5.50}$$

Finally, by introducing the previous approximation for the turbulent viscosity into the Boussinesq approximation 5.43, noting that for two-dimensional turbulent flows the only significant Reynolds stress term is $\tau_{xy} = \tau_{yx} = -\rho\langle u'v'\rangle$, and that the mean velocity gradient $\frac{\partial\langle u\rangle}{\partial y}$ is the most significant one, the following is obtained:

$$\tau_{xy} = \tau_{yx} = -\rho\langle u'v'\rangle = \rho l_m^2 \left|\frac{\partial\langle u\rangle}{\partial y}\right| \frac{\partial\langle u\rangle}{\partial y} \tag{5.51}$$

In which the constant of proportionality C has been absorbed into the mixing length l_m. From the previous expression, it is clear that the Reynolds stresses are heavily dependent on the flow characteristics as already stated. Consequently, the mixing length l_m will vary depending on the type of turbulent flow. For relatively simple two-dimensional turbulent flows such as mixing layers, jets or wakes, the mixing layer l_m can be approximated by simple algebraic expressions:

Flow	**Mixing Length** l_m	**L**
Mixing layer	0.07L	Layer width
Jet	0.09L	Jet half width
Wake	0.16L	Wake half width
Axisymmetric jet	0.075L	Jet half width

Table 2: Mixing lengths for two-dimensional turbulent flows [6]

The main advantage of the mixing length model is its simplicity, as no extra equations are needed to be solved. Consequently, it is really cheap computationally. However, even though the model works well for thin shear layers such as mixing layers, wakes and boundary layers, it does not work properly for turbulent flows with recirculation or separation zones.

The mixing length model is the basis for the Law of the Wall, which is described in the following section.

Law of the wall

In wall-bounded turbulent flows, close to the wall, three different regimes regarding the contribution of the Reynolds stresses in the total stresses can be observed. At the closest zone to the wall, a dampening effect of the turbulent or Reynolds stresses is observed. This dampening effect implies that there exists a region where viscous stresses dominate, known as the *viscous sub-layer*. After this zone, a transition zone is observed, in which the order of magnitude of the Reynolds shear stresses and viscous stresses are approximately equal in magnitude. This zone is known as the *transition or buffer layer*. Finally, this regions transitions to the last one, in which Reynolds stresses dominate, being those much larger than the viscous shear stresses. In this layer, known as the *fully turbulent or log-law layer*, the Prandtl's mixing length theory can be used.

Assuming that the fully turbulent layer begins at a distance from the wall (y) much smaller than the thickness of the boundary layer (δ), the total shear stresses can be approximated using a simple Taylor expansion series, such that:

$$\tau = \tau_w + \underbrace{\frac{\mathrm{d}\tau}{\mathrm{d}y} y}_{\ll \tau_\mathrm{w}} + \cdots \simeq \tau_\mathrm{w} \tag{5.52}$$

In the viscous sub-layer, as already stated, only viscous stresses are important, as Reynolds stresses are damped due to the presence of the wall, consequently:

$$\tau = \mu \frac{d\langle u \rangle}{dy} = \tau_w \rightarrow \langle u \rangle = \frac{\tau_w}{\mu} y \tag{5.53}$$

At this point, the friction velocity can be defined as:

$$u_\tau = \sqrt{\frac{\tau_w}{\rho}} \tag{5.54}$$

Which is used to define a non-dimensional velocity (u^+) and a dimensionless length scale (y^+) as:

$$u^+ = \frac{\langle u \rangle}{u_\tau} \tag{5.55}$$

$$y^+ = \frac{u_\tau y}{\nu} \tag{5.56}$$

With the friction velocity defined, equation 5.53 for the viscous sub-layer can be written as:

$$u^+ = \frac{\langle u \rangle}{u_\tau} = \frac{u_\tau}{\nu} y = y^+ \tag{5.57}$$

On the other hand, in the fully turbulent zone, the viscous shear stresses are negligible, and thus, the Reynolds stresses are dominant, i.e:

$$\tau = -\rho \langle u' v' \rangle = \tau_w \tag{5.58}$$

Recalling the mixing length model 5.51, and assuming that the mixing length $l_m \propto y$:

$$\left(\frac{d\langle u \rangle}{dy} \right)^2 \propto \frac{\tau_w}{\rho} \frac{1}{y^2} \rightarrow \frac{d\langle u \rangle}{dy} \propto \frac{u_\tau}{y} \tag{5.59}$$

Integrating the previous equation yields:

$$C_0 \langle u \rangle = ln(y) + C_0' \tag{5.60}$$

Where C_0 and C_0' are to integration constants. By making use of the definitions of u^+ and y^+ from equations 5.55 and 5.56, equation 5.60 can be written as:

$$u^+ = C_1 ln(y^+) + C_2 \tag{5.61}$$

Where C_1 and C_2 are two constants that need to be empirically found by comparing the previous expression with experimental data. By doing so, it is found that:

$$C_1 \approx 2.54 \qquad C_2 \approx 5.56 \tag{5.62}$$

C_1 is typically written as $1/\kappa$ where $\kappa = 0.41$, and known as the von Kármán constant, as he was the first to derive the logarithmic velocity profile.

If both velocity profiles for the viscous sub-layer and for the log-law region are graphed, and compared with experimental data, the graph shown in figure 13 is obtained. As it can be seen, for $y^+ < 5$ experimental results show excellent agreement with the expression found for the viscous sub-layer, implying that viscous shear stresses dominate, as already stated. For y^+ values higher than 5, the same approximation can be used, even though leading to higher errors. For $5 < y^+ < 30$ (the buffer layer), neither of the laws derived hold true. However, for $y^+ < 11$, the linear approximation should be used, while for $y^+ > 11$, it is advisable to use the logarithmic law. Finally, for $y^+ > 30$, the logarithmic law shows very good agreement with experimental data as well.

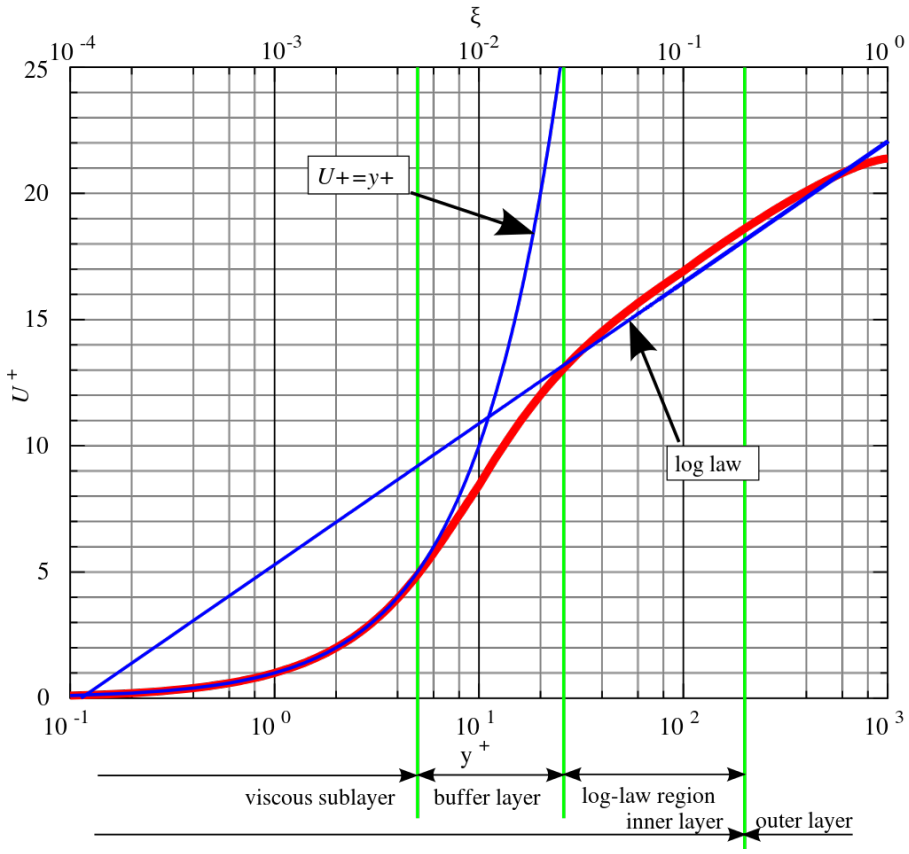

Figure 13: Law of the Wall. Extracted from [3]

5.3.1.2 The $k - \varepsilon$ model

The $k - \varepsilon$ turbulence model focuses on the mechanisms that affect the turbulent kinetic energy [6]. The model has two equations, one for the turbulent kinetic energy k, and another one for

the rate of dissipation of turbulent kinetic energy per unit of mass ε. Both parameters can be used to define a velocity scale ϑ and a length scale ℓ such that:

$$\vartheta = k^{1/2} \tag{5.63}$$

$$\ell = \frac{k^{3/2}}{\varepsilon} \tag{5.64}$$

Which are representative of the large-scale turbulence. Applying the same dimensional analysis as in the mixing length model previously derived, the following expression is obtained:

$$\mu_t = \mathrm{C}\rho\,\vartheta\ell = \rho C_\mu \frac{k^2}{\varepsilon} \tag{5.65}$$

In which C_μ is a non-dimensional constant. Consequently, the standard $k-\varepsilon$ model makes use of one transport equation for the turbulent kinetic energy k and another one for the rate of dissipation of turbulent kinetic energy ε, to solve for the turbulent viscosity μ_t.

$$\frac{\partial(\rho k)}{\partial t} + \nabla\cdot(\rho k\langle\mathbf{v}\rangle) = \nabla\cdot\left[\frac{\mu_t}{\sigma_k}\nabla k\right] + 2\mu_t\langle S_{ij}\rangle\cdot\langle S_{ij}\rangle - \rho\varepsilon \tag{5.66}$$

$$\frac{\partial(\rho\varepsilon)}{\partial t} + \nabla\cdot(\rho\varepsilon\langle\mathbf{v}\rangle) = \nabla\left[\frac{\mu_t}{\sigma_\varepsilon}\nabla\varepsilon\right] + C_{1\varepsilon}\frac{\varepsilon}{k}2\mu_t\langle S_{ij}\rangle\cdot\langle S_{ij}\rangle - C_{2\varepsilon}\rho\frac{\varepsilon^2}{k} \tag{5.67}$$

The terms on the left hand side represent the rate of change of k or ε and the transport of those quantities by convection. The first term on the right hand side represents the transport of k or ε by diffusion, the second term represents the rate of production of those quantities, while the last one is their rate of destruction. In the equations there are five adjustable constants C_μ, σ_k, σ_ε, $C_{1\varepsilon}$ and $C_{2\varepsilon}$ that are found through data fitting of of various turbulent flows. Their typical values are:

$$C_\mu = 0.09 \quad \sigma_k = 1.00 \quad \sigma_\varepsilon = 1.30 \quad C_{1\varepsilon} = 1.44 \quad C_{2\varepsilon} = 1.92 \tag{5.68}$$

With the previous equations, a system is obtained which allows to find the turbulent viscosity μ_t, and in virtue of the Boussinesq's approximation, close the system.

The main drawback of the $k-\varepsilon$ model is that it predicts excessive turbulent shear stresses, specially when adverse pressure gradients are present. Consequently, flow separation in curved shear layers is not well predicted.

5.3.1.3 Spalart-Allmaras model

The Spalart-Allmaras model provides more economical resolutions of boundary layers for external aerodynamics. It relates the eddy viscosity μ_t to a kinematic eddy viscosity parameter $\tilde{\nu}$ and to a wall-damping function $f_{\nu 1} = f_{\nu 1}(\tilde{\nu}/\nu)$:

$$\mu_t = \rho\tilde{\nu}f_{\nu 1} \tag{5.69}$$

The wall damping function tends to unity when the Reynolds number is high, in which case the kinematic eddy viscosity parameter equals the kinematic eddy viscosity, while at the wall, the

function f_{v1} tends to zero. Consequently, for this model, an extra transport equation for $\tilde{\nu}$ needs to be solved:

$$\frac{\partial(\rho\tilde{\nu})}{\partial t} + \nabla\cdot(\rho\tilde{\nu}\langle\mathbf{v}\rangle) = \frac{1}{\sigma_\nu}\nabla\cdot\left[(\mu+\rho\tilde{\nu})\nabla\tilde{\nu} + C_{b2}\rho\frac{\partial\tilde{\nu}}{\partial x_k}\frac{\partial\tilde{\nu}}{\partial x_k}\right] + C_{b1}\rho\tilde{\nu}\tilde{\Omega} - C_{w1}\rho\left(\frac{\tilde{\nu}}{\kappa y}\right)^2 f_w \quad (5.70)$$

The left hand side of the previous equation represents the rate of change of the viscosity parameter $\tilde{\nu}$ and its transport by convection. The right hand side expresses the transport of $\tilde{\nu}$ by turbulent diffusion, and the rate of production and dissipation of $\tilde{\nu}$. As it can be seen, the rate of production of $\tilde{\nu}$ is related to the local mean of vorticity $\langle\Omega\rangle = \sqrt{2\langle\Omega_{ij}\rangle\langle\Omega_{ij}\rangle}$ where $\langle\Omega_{ij}\rangle$ is the mean vorticity tensor:

$$\tilde{\Omega} = \langle\Omega\rangle + \frac{\tilde{\nu}}{(\kappa y)^2} f_{\nu 2} \quad (5.71)$$

While the functions $f_{\nu 2} = f_{\nu 2}(\tilde{\nu}/\nu)$ and $f_w = f_w(\tilde{\nu}/(\tilde{\Omega}\kappa^2 y^2))$ are two additional wall damping functions. The model constants are empirically found to be:

$$\sigma_\nu = 2/3 \quad \kappa = 0.4187 \quad C_{b1} = 0.1355 \quad C_{b2} = 0.622 \quad C_{w1} = C_{b1} + \kappa^2\frac{1+C_{b2}}{\sigma_\nu} \quad (5.72)$$

Unlike the $k-\epsilon$ model, the Spalart-Allmaras model performs good for solving boundary layers under adverse pressure gradients. However, for rapidly changing flows, the model does not perform well.

5.3.1.4 Wilcox $k-\omega$ model

In the $k-\omega$ model, the turbulent frequency $\omega = \varepsilon/k$ is used as the second model variable alongside k, to define the length scale as $l = \sqrt{k}/\omega$. Consequently, the eddy viscosity is written as:

$$\mu_t = \rho k/\omega \quad (5.73)$$

Which is used in combination with the Boussinesq's expression to compute the Reynolds stresses. Consequently, like in the $k-\varepsilon$ model, one transport equation is needed for k, while another one is needed for ω. The former reads the following:

$$\frac{\partial(\rho k)}{\partial t} + \nabla\cdot(\rho k\langle\mathbf{v}\rangle) = \nabla\cdot\left[\left(\mu+\frac{\mu_t}{\sigma_k}\right)\nabla k\right] + \left(2\mu_t\langle S_{ij}\rangle\cdot\langle S_{ij}\rangle - \frac{2}{3}\rho k\frac{\partial\langle u_i\rangle}{\partial x_j}\delta_{ij}\right) - \beta^*\rho k\omega \quad (5.74)$$

While the transport equation for ω reads:

$$\frac{\partial(\rho\omega)}{\partial t} + \nabla\cdot(\rho\omega\langle\mathbf{v}\rangle) = \nabla\cdot\left[\left(\mu+\frac{\mu_t}{\sigma_\omega}\right)\nabla\omega\right] + \gamma_1\left(2\rho\langle S_{ij}\rangle\cdot\langle S_{ij}\rangle - \frac{2}{3}\rho\omega\frac{\partial\langle u_i\rangle}{\partial x_j}\delta_{ij}\right) - \beta_1\rho\omega^2 \quad (5.75)$$

As in the previous transport equations, the left hand side of equations 5.74 and 5.75 represent the rate of change of k or ω and their transport by convection. On the other hand, on the right hand side each term represents, from left to right, the transport of k or ω by turbulent diffusion,

their rate of production and their rate of dissipation.

The model has the following model parameters:

$$\sigma_k = 2.0 \quad \sigma_w = 2.0 \quad \gamma_1 = 0.553 \quad \beta_1 = 0.075 \quad \beta^* = 0.09 \tag{5.76}$$

This model is specially interesting, as integration to the wall doesn't require wall-damping functions for low values of the Reynolds number.

6 Large eddy simulation (LES)

Even though different turbulence models have been developed for the RANS equations, a general purpose model that can be used for a wide range of applications and flow configurations has not been found yet. This can be explained due to the different behaviour of the large and small eddies. While the smaller eddies show a universal behaviour and are nearly isotropic, the largest eddies, which are responsible for extracting energy of the mean flow, are anisotropic and heavily-dependent on the flow configurations and boundary conditions. RANS equations try to model the collective behaviour of all the eddies of the flow, by modelling them with a single turbulence model. This implies that a general model that can be used in a wide set of applications is difficult to find. The essence of the Large eddy simulation (LES) approach is to solve for the larger eddies of the flow, which are problem-dependent, with a time-dependent simulation, while the effect of the smaller eddies, which are universal, is modelled.

In large eddy simulation (LES), a spatial filtering operator is used to separate the larger eddies and the smaller ones. This process is done by selecting a filtering function and a cutoff width, which sets the minimum length scale of the eddies that are solved in an unsteady computation. However, the information regarding the smaller eddies, which are filtered, is destroyed. Additionally, the effects of the interaction between the larger and smaller eddies is also lost, giving rise to sub-grid-scale stresses (SGS stresses), whose effect must be described by means of a SGS model.

The basic idea behind the large eddy simulation approach is shown in the following figure of the energy cascade:

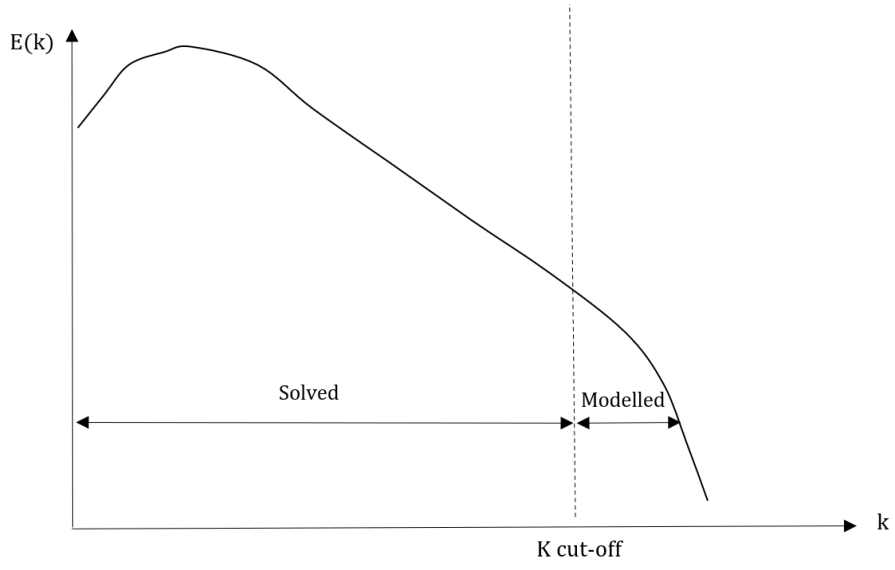

Figure 14: Filtered energy spectrum

6.1 Filtering functions

The spatial filtering function needed in LES separates scales by using a high-pass filter (low-pass filter in frequency). Mathematically, in physical space, it can be represented as a convolution product:

$$\bar{\phi}(\boldsymbol{x},t) = \int_{-\infty}^{+\infty}\int_{-\infty}^{+\infty} \phi\left(\boldsymbol{\xi},t'\right) G\left(\boldsymbol{x}-\boldsymbol{\xi},t-t'\right) dt' d^3\boldsymbol{\xi} \tag{6.1}$$

Where $\phi(\bar{\mathbf{x}},t)$ is the filtered function, and $\phi(\mathbf{x},t)$ is the unfiltered function. G is the convolution kernel which depends on the filter used, and depends on the cutoff scales in both space and time $\bar{\Delta}$ and $\bar{\tau_c}$, respectively. As it can be seen, filtering is an integration (a linear operator), and unlike the averaging used in RANS, in LES the integration is carried out in three dimensional space.

The previous integral can be written as:

$$\bar{\phi} = G \star \phi \tag{6.2}$$

And converted into Fourier space, the spectrum of the filtered function is found by multiplying the spectrum $\widehat{\phi}(\boldsymbol{k},\omega)$ of $\phi(\boldsymbol{x},t)$ by the spectrum of the kernel $\widehat{G}(\boldsymbol{k},\omega)$:

$$\overline{\widehat{\phi}}(\boldsymbol{k},\omega) = \widehat{\phi}(\boldsymbol{k},\omega)\widehat{G}(\boldsymbol{k},\omega) \tag{6.3}$$

Being k and ω the spatial wave number and time frequency. The spatial cutoff length $\bar{\Delta}$ and the cutoff time scale $\bar{\tau_c}$ are associated to the cutoff wave number k_c and cutoff frequency ω_c respectively.

The unresolved part of $\phi(\mathbf{x},t)$ is denoted by $\phi'(\mathbf{x},t)$ and can be defined as:

$$\begin{aligned}\phi'(\boldsymbol{x},t) &= \phi(\boldsymbol{x},t) - \bar{\phi}(\boldsymbol{x},t) \\ &= \phi(\boldsymbol{x},t) - \int_{-\infty}^{+\infty}\int_{-\infty}^{+\infty} \phi\left(\boldsymbol{\xi},t'\right) G\left(\boldsymbol{x}-\boldsymbol{\xi},t-t'\right) dt' d^3\boldsymbol{\xi} = (1-G)\star\phi\end{aligned} \tag{6.4}$$

Or in spectral form:

$$\widehat{\phi'} = (1-\widehat{G})\hat{\phi} \tag{6.5}$$

The filter used must verify certain properties to be applied to the Navier-Stokes equations [24]:

- Conservation of constants: $\bar{a} = a \Longleftrightarrow \int_{-\infty}^{+\infty}\int_{-\infty}^{+\infty} G\left(\boldsymbol{\xi},t'\right) d^3\boldsymbol{\xi} dt' = 1$
- Linearity: $\overline{\phi+\psi} = \bar{\phi} + \bar{\psi}$. Which is always satisfied independently of the kernel G due to the characteristics of the product of convolution.
- Commutation with derivation: $\overline{\dfrac{\partial\phi}{\partial s}} = \dfrac{\partial\bar{\phi}}{\partial s}, \quad s = \boldsymbol{x}, t$

Introducing the commutator $[f, g]$ of two operators f and g applied to a variable ϕ: $[f, g]\phi \equiv f \circ g(\phi) - g \circ f(\phi) = f(g(\phi)) - g(f(\phi))$; has the following properties:

$$
\begin{array}{l}
[f, g] = -[g, f] \quad \text{Skew-symmetry} \\
[f \circ g, h] = [f, h] \circ g + f \circ [g, h] \quad \text{Leibniz identity} \\
[f, [g, h]] + [g, [h, f]] + [h, [f, g]] = 0 \quad \text{Jacobi's identity}
\end{array}
$$

The filters that fulfill these properties, are not, in general, Reynolds operators, which imply that:

$$
\begin{aligned}
\overline{\bar{\phi}} &= G \star G \star \phi = G^2 \star \phi \neq \bar{\phi} = G \star \phi \\
\overline{\phi'} &= G \star (1 - G) \star \phi \neq 0
\end{aligned}
$$

Which implies that G is not a projector, i.e $(G \circ G) \neq G$. Therefore, the filtering operation might be understood as a change of variable which can be inverted without implying information loss.

The convolution kernel G in $\mathbb{R}^4$ can be assumed to be obtained by the multiplication of mono-dimensional kernels as:

$$
G\left(\boldsymbol{x} - \boldsymbol{\xi}, t - t'\right) = G(\boldsymbol{x} - \boldsymbol{\xi}) G_t\left(t - t'\right) = G_t\left(t - t'\right) \prod_{i=1,3} G_i\left(x_i - \xi_i\right)
$$

However, in LES, the most employed approach is spatial filtering. Consequently:

$$
G_t\left(t - t'\right) = \delta\left(t - t'\right)
$$

While different forms of the space kernel can be used. Nevertheless, given that the dynamics of the Navier-Stokes equations allow to associate a characteristic time with each characteristic length, a spatial filtering induces a time filtering, although implicitly.

The most common filtering functions in LES in three dimensions are:

- **Top-hat or box filter:**

$$
G(x - \xi) = \begin{cases} \dfrac{1}{\bar{\Delta}} & \text{if} \quad |x - \xi| \leqslant \frac{\bar{\Delta}}{2} \\ 0 & \text{otherwise} \end{cases} \tag{6.6}
$$

And the transfer function $\hat{G}$:

$$
\hat{G}(k) = \frac{\sin(k\bar{\Delta}/2)}{k\bar{\Delta}/2} \tag{6.7}
$$

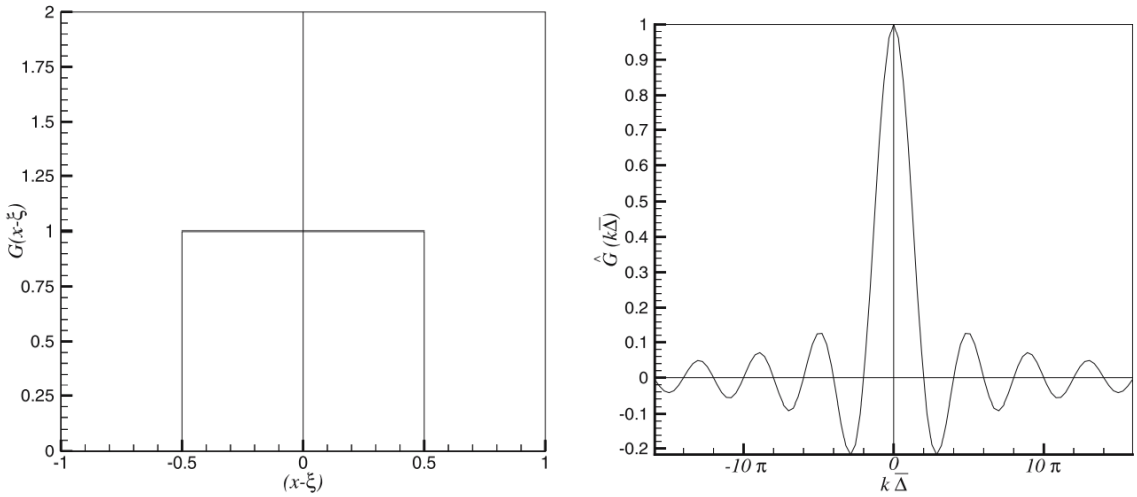

Figure 15: Top-hat filter. Convolution kernel in the physical space normalised by $\bar{\Delta}$ (left) and its transfer function (right)

- **Gaussian filter:**

$$G(x-\xi) = \left(\frac{\gamma}{\pi\bar{\Delta}^2}\right)^{1/2} \exp\left(\frac{-\gamma|x-\xi|^2}{\bar{\Delta}^2}\right)$$
$$\widehat{G}(k) = \exp\left(\frac{-\bar{\Delta}^2 k^2}{4\gamma}\right) \tag{6.8}$$

  Being the typical value for $\gamma = 6$

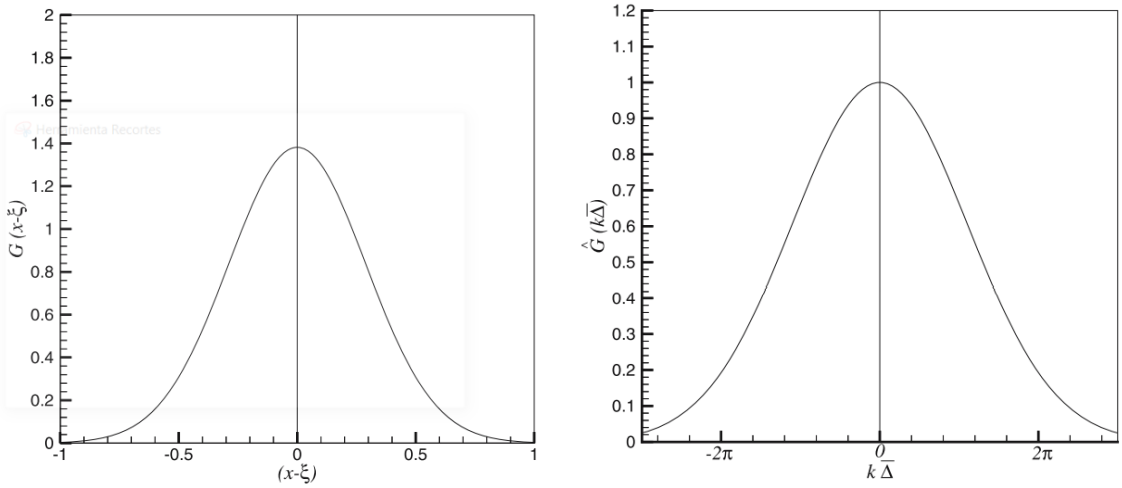

Figure 16: Gaussian filter. Convolution kernel in the physical space normalised by $\bar{\Delta}$ (left) and its transfer function (right)

- **Spectral or sharp cutoff filter:**

$$G(x-\xi) = \frac{\sin\left(k_c(x-\xi)\right)}{k_c(x-\xi)}, \text{ with } k_c = \frac{\pi}{\bar{\Delta}}$$
$$\widehat{G}(k) = \begin{cases} 1 & \text{if } |k| \leqslant k_c \\ 0 & \text{otherwise} \end{cases} \tag{6.9}$$

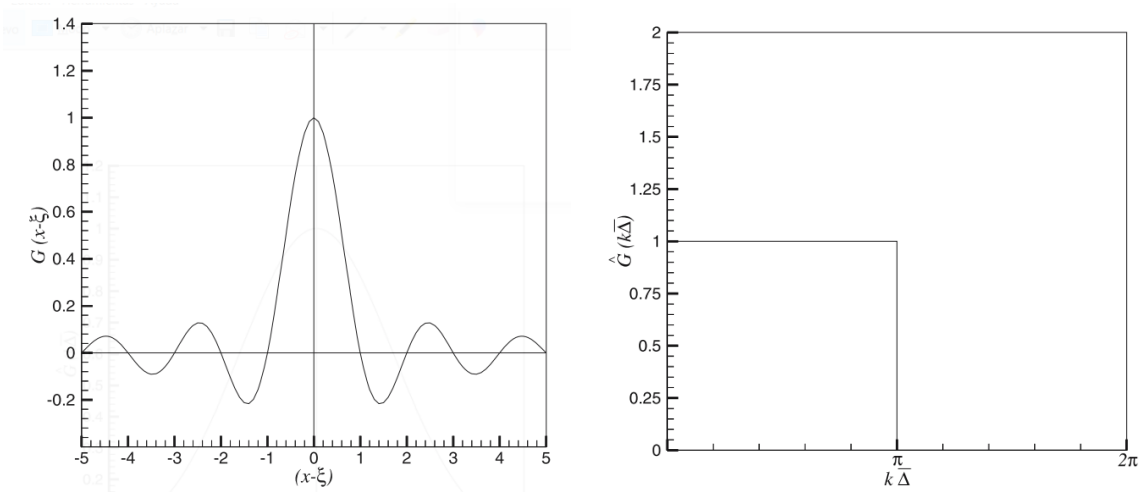

Figure 17: Sharp cutoff filter. Convolution kernel in the physical space normalised by $\bar{\Delta}$ (left) and its transfer function (right)

The top-hat filter is typically used in FVM implementations of LES, while the Gaussian and spectral cutoff filters are usually employed in the research literature, the former being introduced by the Stanford group in finite differences, while the latter is rarely used in general-purpose CFD codes [6].

6.2 Filtered unsteady Navier-Stokes equations

Recalling the incompressible form of the Navier-Stokes equations (momentum and mass conservation) 5.24 and 5.25, and making use of the linearity of the filtering operation and its basic property regarding its commutation with derivation, the following filtered equations are obtained:

$$\rho\left(\frac{\partial \overline{u_i}}{\partial t} + \frac{\partial}{\partial x_j}(\overline{u_i u_j})\right) = -\frac{\partial \overline{p}}{\partial x_i} + \frac{\partial}{\partial x_j}\left[\mu\left(\frac{\partial \overline{u_i}}{\partial x_j} + \frac{\partial \overline{u_j}}{\partial x_i}\right)\right] \tag{6.10}$$

$$\frac{\partial \overline{u_i}}{\partial x_i} = 0 \tag{6.11}$$

As it can be seen, the continuity equation reads exactly the same, with the difference that the filtered velocity is used instead . On the momentum equation, the filtered pressure $\overline{p}$ appears, as well as a non-linear term $\overline{u_i u_j}$, which must be expressed as a function of $\overline{\mathbf{v}}$ and $\mathbf{v}'$, in a similar way as it was done in the RANS equations with the Reynolds stress term. It must be noticed that the tilde represents the fluctuations or unresolved part. This non-linear term can be expressed as triple decomposition which allows to express it in terms of the filtered quantity and the unresolved scales as:

$$\overline{u_i u_j} = \overline{(\overline{u_i} + u_i')(\overline{u_j} + u_j')} = \overline{\overline{u_i}\overline{u_j}} + \overline{\overline{u_i} uj'} + \overline{\overline{u_j} u_i'} + \overline{u_i' u_j'} \tag{6.12}$$

The previous decomposition can be used to rewrite the filtered momentum equation as:

$$\rho\left(\frac{\partial \overline{u_i}}{\partial t} + \frac{\partial}{\partial x_j}(\overline{\overline{u_i}\overline{u_j}})\right) = -\frac{\partial \overline{p}}{\partial x_i} + \frac{\partial}{\partial x_j}\left[\mu\left(\frac{\partial \overline{u_i}}{\partial x_j} + \frac{\partial \overline{u_j}}{\partial x_i}\right)\right] - \frac{\partial \tau_{ij}}{\partial x_j} \tag{6.13}$$

The subgrid tensor τ includes all the terms that are not only dependent on the large scales, i.e:

$$\tau_{ij} = C_{ij} + R_{ij} \tag{6.14}$$

Where

$$C_{ij} = \rho\overline{\overline{u_i} u_j'} + \rho\overline{u_i' \overline{u_j}} \tag{6.15}$$

$$R_{ij} = \rho\overline{u_i' u_j'} \tag{6.16}$$

C_{ij} is the cross-stress tensor, which represents the interaction between the larger and the smaller scales. The subgrid tensor R, known as the Reynolds subgrid tensor, reflects the interaction between smaller scales. This approach, known as the double decomposition, focuses on the fact that all the terms that are present on the equations of the filtered quantities must also be filtered quantities. However, another approach is to consider that the terms must be evaluated directly from filtered variables. To do so, the term $\overline{\overline{u_i}\overline{u_j}}$ must be decomposed further by using Leonard's decomposition:

$$\rho\overline{\overline{u_i}\overline{u_j}} = \rho(\overline{\overline{u_i}\overline{u_j}} - \overline{u}_i\overline{u}_j) + \rho\overline{u}_i\overline{u}_j = L_{ij} + \rho\overline{u}_i\overline{u}_j \tag{6.17}$$

Where L_{ij} is the Leonard tensor, given by:

$$L_{ij} = \rho(\overline{\overline{u_i}\overline{u_j}} - \overline{u}_i\overline{u}_j) \tag{6.18}$$

Thus, the term $\rho\overline{u_i u_j}$ can be expressed as:

$$\rho\overline{u_i u_j} = \rho\overline{u}_i\overline{u}_j + L_{ij} + C_{ij} + R_{ij} \tag{6.19}$$

Where:

$$\tau_{ij} = L_{ij} + C_{ij} + R_{ij} = \rho\overline{u_i u_j} - \rho\overline{u}_i\overline{u}_j \tag{6.20}$$

This decomposition is known as the triple decomposition or simply Leonard decomposition, and allows to rewrite the filtered Navier-Stokes momentum equation as:

$$\rho\left(\frac{\partial \overline{u_i}}{\partial t} + \frac{\partial}{\partial x_j}(\overline{u}_i\overline{u}_j)\right) = -\frac{\partial \overline{p}}{\partial x_i} + \frac{\partial}{\partial x_j}\left[\mu\left(\frac{\partial \overline{u_i}}{\partial x_j} + \frac{\partial \overline{u_j}}{\partial x_i}\right)\right] - \frac{\partial \tau_{ij}}{\partial x_j} \tag{6.21}$$

It is important to notice that the non linear term $\overline{u}_i\overline{u}_j$ is quadratic, and thus, it contains frequencies higher than each of the composing terms. Additionally, it must be noticed the fact that, if the filter is a Reynolds operator (i.e $\overline{\overline{\mathbf{u}}} = \overline{\mathbf{u}}$, $\overline{\mathbf{u}'} = 0$, $\overline{\overline{\mathbf{u}}\overline{\mathbf{u}}} = \overline{\mathbf{u}}\overline{\mathbf{u}}$), the tensors C_{ij} and L_{ij} are

identically zero and the subgrid tensor is reduced to the tensor R_{ij}.

As it can be seen, the difference between the closure problem in LES and in RANS is that in LES the average of the product is not the product of the averages. This implies that in LES more interactions need to be modelled in comparison to RANS modelling.

6.2.1 Eddy Viscosity closure models in LES

The basic idea for the closure problem is to find a tensor $\mathcal{S}(\overline{\mathbf{u}}, \overline{\mathbf{u}})$ which approximates the sub-grid scale tensor τ_{ij}. The idea behind the eddy viscosity models employed in LES is totally analogous to the Boussines'q hypothesis previously derived for RANS equations. Smagorinsky (1963) suggested that, given the isotropy property of the smaller eddies, Boussinesq's approximation might give a good approximation regarding the effect of the unresolved scales on the solved ones. Consequently, the Reynolds subgrid tensor R_{ij} is assumed to be proportional to the mean filtered rate of strain tensor $\overline{S_{ij}}$:

$$R_{ij} = -2\mu_t \bar{S}_{ij} + \frac{1}{3} R_{ii}\delta_{ij} = -\mu_t \left(\frac{\partial \bar{u}_i}{\partial x_j} + \frac{\partial \bar{u}_j}{\partial x_i} \right) + \frac{1}{3} R_{ii}\delta_{ij} \tag{6.22}$$

In which the proportionality constant μ_t appears, with dimensions of $Pa \cdot s$. The term $\frac{1}{3}R_{ii}\delta_{ij}$ performs the same function as the term $-\frac{2}{3}\rho k \delta_{ij}$ in the Boussinesq's approximation in equation 5.43, making sure that the sum of the modelled normal sub-grid scale tensor stresses is equal to the kinetic energy of the unfiltered eddies [6]. Nevertheless, in current CFD codes, it is common to model the whole stress tensor τ_{ij} as a single entity by means of a unique SGS turbulence model:

$$\tau_{ij} = -2\mu_t \bar{S}_{ij} + \frac{1}{3} \tau_{ii}\delta_{ij} = -\mu_t \left(\frac{\partial \bar{u}_i}{\partial x_j} + \frac{\partial \bar{u}_j}{\partial x_i} \right) + \frac{1}{3} \tau_{ii}\delta_{ij} \tag{6.23}$$

The term $\frac{1}{3}\tau_{ii}\delta_{ij}$ of the eddy viscosity approach is usually included into the pressure term, giving place to a modified filtered pressure in the filtered momentum equation, and thus, it is commonly neglected when modelling the SGS tensor. Consequently, through the use of the eddy viscosity modelling, the filtering equations for incompressible flow read:

$$\rho \left(\frac{\partial \overline{u_i}}{\partial t} + \frac{\partial}{\partial x_j}(\overline{u}_i \overline{u}_j) \right) = -\frac{\partial \overline{p}}{\partial x_i} + \frac{\partial}{\partial x_j} \left[(\mu + \mu_t) \left(\frac{\partial \overline{u_i}}{\partial x_j} + \frac{\partial \overline{u_j}}{\partial x_i} \right) \right] \tag{6.24}$$

$$\frac{\partial \overline{u_i}}{\partial x_i} = 0 \tag{6.25}$$

Therefore, the only thing remaining is to find an expression for the eddy viscosity.

$$\mu_t = \rho (C_m \bar{\Delta})^2 D_m(\bar{\mathbf{v}}) \tag{6.26}$$

Where C_m is the model constant and $D_m(\bar{\mathbf{v}})$ is the differential operator with units of frequency.

6.2.1.1 Smagorinsky-Lilly SGS model

The Smagorinsky-Lilly model is based on the Prandtl's mixing length previously derived. It assumes that, given the units of the dynamic eddy viscosity ($kgm^{-1}s^{-1}$), this can be expressed as the product of the density with one length scale and one velocity scale, i.e: $\mu_t = \rho l_{\bar{\Delta}} v_{\bar{\Delta}}$. Regarding the characteristic length, it is reasonable to use the cutoff width multiplied by a constant:

$$l_{\bar{\Delta}} = C_S \bar{\Delta} \tag{6.27}$$

The constant, known as the Smagorinsky constant, indicates the fraction of the cutoff width that gives the sub-grid length scale, which is the average length-scale of the unfiltered eddies. Regarding the characteristic velocity, the filtered rate of strain tensor can be used to express the sub-grid scale velocity as:

$$v_{\bar{\Delta}} = l_{\bar{\Delta}} \sqrt{2\overline{S}_{ij}\overline{S}_{ij}} \tag{6.28}$$

Consequently, the Smagorinsky eddy viscosity reads:

$$\mu_t = \rho (C_S \bar{\Delta})^2 \sqrt{2\overline{S}_{ij}\overline{S}_{ij}} = \rho (C_S \bar{\Delta})^2 |\bar{S}| \tag{6.29}$$

At this point, the only thing remaining is to find the value for the Smagorinsky constant C_S. In order to determine it, it can be assumed that the smallest modelled scale $k_c = \pi/\bar{\Delta}$ is inside the inertial subrage of Kolmogorov's energy spectrum:

$$E(k) = C_K \varepsilon^{2/3} k^{-5/3} \tag{6.30}$$

Under this assumption made, if the kinetic energy dissipation ε is equated with the model dissipation, an expression for the Smagorinsky constant can be obtained:

$$\varepsilon = (C_S \bar{\Delta})^2 |\bar{S}|^3 \tag{6.31}$$

And $|\bar{S}|$ is evaluated as follows:

$$|\bar{S}|^2 = 2 \int_0^{k_c} k^2 E(k) dk = \frac{3}{2} C_K \varepsilon^{2/3} k_c^{4/3} \tag{6.32}$$

Consequently, by taking $C_k \approx 1.58$:

$$C_S = \frac{1}{\pi} \left(\frac{2}{3C_K} \right)^{3/4} \approx 0.17 \tag{6.33}$$

With a value for the Smagorinsky constant of $C_s = 0.17$, the model provides excellent results for homogeneous isotropic turbulence [25]. However, in practical applications it is common to use $C_s = 0.11$. Additionally, there is energy transfer everywhere from the filtered scales to the unfiltered ones, meaning that there is no backscatter (although this is applicable to any eddy viscosity model) [21]. However, it is not the most appropriate model to capture the near-wall behaviour properly. This can be easily understood by analysing the Smagorinsky eddy viscosity,

which does not vanish at the wall.

As it can be seen, by specifying the Smagorinsky constant and the Smagorinsky length scale, the filtered Navier-Stokes equations 6.24 and 6.25 can be solved without directly specifying the filter used, as it does not appear neither in the equations, nor in the Smagorinsky model. However, the filter used is implicitly contained inside the model used.

6.2.1.2 Proper invariants for eddy-viscosity sub-grid scale models

The eddy-viscosity model presented for LES rely on differential operators seeking to properly detect different flow configurations. The majority of the eddy-viscosity models are formed through the combination of invariants of a symmetric tensor that depends on the gradient of the filtered velocity $\overline{G}_{ij} = \dfrac{\partial \overline{u}_i}{\partial x_j}$, mainly the symmetric part of the tensor (rate of strain) $\overline{S}_{ij}$, and the skew-symmetric part $\overline{\Omega}_{ij} = \dfrac{1}{2}\left(\dfrac{\partial \overline{u}_i}{\partial x_j} - \dfrac{\partial \overline{u}_j}{\partial x_i}\right)$. The tensor $\overline{G}_{ij}$ contains 8 independent elements and can be characterised by 5 invariants:

$$\left\{Q_{\mathrm{G}}, R_{\mathrm{G}}, Q_{\mathrm{S}}, R_{\mathrm{S}}, V^2\right\} \tag{6.34}$$

Where:

$$P_{\mathrm{A}} = \mathrm{tr(A)} \tag{6.35}$$

$$Q_{\mathrm{A}} = 1/2\left\{tr^2(\mathrm{A}) - \mathrm{tr}\left(\mathrm{A}^2\right)\right\} \tag{6.36}$$

$$R_{\mathrm{A}} = \det(\mathrm{A}) = 1/6\left\{tr^3(\mathrm{A}) - 3\,\mathrm{tr(A)}\,\mathrm{tr}\left(\mathrm{A}^2\right) + 2\,\mathrm{tr}\left(\mathrm{A}^3\right)\right\} \tag{6.37}$$

$$V^2 = 4\left(tr\left(\overline{\mathrm{S}}^2\overline{\Omega}^2\right) - 2Q_{\mathrm{s}}Q_{\Omega}\right) \tag{6.38}$$

P_A, Q_A and R_A represent the first, second and third invariants of a A, which is a second order tensor. The subscript $_G$ or $_s$ indicate if it is the corresponding invariant of $\overline{G}_{ij}$ or $\overline{S}_{ij}$ respectively. It is interesting to notice that if tensor A is traceless, the previous expressions reduce to:

$$P_{\mathrm{A}} = 0 \tag{6.39}$$

$$Q_{\mathrm{A}} = -1/2\,\mathrm{tr}\left(\mathrm{A}^2\right) \tag{6.40}$$

$$R_{\mathrm{A}} = \det(\mathrm{A}) = 1/3\,\mathrm{tr}\left(\mathrm{A}^3\right) \tag{6.41}$$

The following relations can be derived between the principal invariants:

$$P_{\mathrm{G}} = P_{\mathrm{S}} = P_{\Omega} = 0 \tag{6.42}$$

$$Q_{\mathrm{G}} = Q_{\mathrm{S}} + Q_{\Omega} \tag{6.43}$$

$$R_{\mathrm{G}} = R_{\mathrm{S}} + \mathrm{tr}\left(\bar{\Omega}^2\overline{\mathrm{S}}\right), \quad R_{\Omega} = 0 \tag{6.44}$$

Finally, for the sake of convenience, the following relations are defined as well:

$$\mathrm{tr}\left(\bar{\mathrm{G}}\bar{\mathrm{G}}^T\right) = \mathrm{tr}\left(\overline{\mathrm{S}}^2\right) - \mathrm{tr}\left(\overline{\Omega}^2\right) = 2\left(Q_\Omega - Q_\mathrm{S}\right) \tag{6.45}$$

$$\mathrm{tr}\left(\overline{\mathrm{S}}^2\overline{\Omega}^2\right) = 1/8\left(\mathrm{tr}\left(\overline{\mathrm{G}}^4\right) - \mathrm{tr}\left(\bar{\mathrm{G}}\bar{\mathrm{G}}^T\bar{\mathrm{G}}\bar{\mathrm{G}}^T\right)\right) = 1/8\left(2Q_\mathrm{G}^2 - \mathrm{tr}\left(\bar{\mathrm{G}}\bar{\mathrm{G}}^T\bar{\mathrm{G}}\bar{\mathrm{G}}^T\right)\right) \tag{6.46}$$

$$\mathrm{tr}\left(\overline{\mathrm{S}}^2\overline{\Omega}^2\right) = V^2/4 + 2Q_\mathrm{s}Q_\Omega \tag{6.47}$$

$$\mathrm{tr}\left(\tilde{\mathrm{A}}^2\right) = \mathrm{tr}\left(\mathrm{A}^2\right) - 1/3tr^2(\mathrm{A}) \tag{6.48}$$

Where $\tilde{\mathrm{A}} = \mathrm{A} - 1/3\mathrm{tr}(\mathrm{A})$ is the traceless part of the tensor A.

6.2.1.3 Unified Framework for eddy-viscosity models

The different eddy-viscosity models employed in large eddy simulations can be re-written in terms of the invariants described in the previous section.

Smagorinsky-Lilly model

The Smagorinsky-Lilly model, previously defined, can be written in terms of the previously defined invariants according to:

$$\nu_t^{\mathrm{smag}} = 2(C_s\bar{\Delta})(-Q_\mathrm{S})^{1/2} \tag{6.49}$$

WALE model

The Wall-adapting local eddy (WALE) viscosity model is based on the second invariant of the traceless part of the symmetric tensor $S_d = 1/2(\bar{G}^2 + (\bar{G}^2)^T) = \bar{S}^2 + \bar{\Omega}^2$. This model, proposed by Nicoud and Ducros, can be written in terms of the basic invariants previously described as:

$$\nu_t^W = \left(C_W\bar{\Delta}\right)^2 \frac{\left(V^2/2 + 2Q_\mathrm{G}^2/3\right)^{3/2}}{(-2Q\mathrm{s})^{5/2} + \left(V^2/2 + 2Q_\mathrm{G}^2/3\right)^{5/4}} \tag{6.50}$$

Where the constant $C_W = \sqrt{0.5}$ [26].

Vreman's model

Vreman's model makes use of the first two invariants of the tensor $\bar{G}\bar{G}^T$, yielding the following expression for the eddy viscosity:

$$\nu_t^{Vr} = \left(C_{Vr}\bar{\Delta}\right)^2 \left(\frac{V^2 + Q_\mathrm{G}^2}{2\left(Q_\Omega - Q_\mathrm{s}\right)}\right)^{1/2} \tag{6.51}$$

The constant used in the Vreman's model is taken as $C_{Vr} = \sqrt{0.07}$.

Verstappen's model

An additional model was proposed by Verstappen, which, in contrast with the previous ones defined, makes use of the third invariant of the filtered rate of strain tensor $\bar{S}$:

$$\nu_t^{\mathrm{Ve}} = (C_{Ve}\bar{\Delta})^2 \frac{|R_s|}{-Q_s} \tag{6.52}$$

Being its proportionality constant equal to $C_{Ve} = 1/\pi\sqrt{3/2}$.

S3PQR model

Trias et al. [26], propose a family of models, all of them based on the invariants of the tensor $\bar{G}\bar{G}^T$, aiming to achieve a better wall behaviour. The three models of this family are shown below:

$$\begin{aligned} \nu_t^{S3PQ} &= \left(C_{s3pq}\bar{\Delta}\right)^2 P_{\mathrm{GG}^T}^{-5/2} Q_{\mathrm{GG}^T}^{3/2} \\ \nu_t^{S3PR} &= \left(C_{s3pr}\bar{\Delta}\right)^2 P_{\mathrm{GG}^T}^{-1} R_{\mathrm{GG}^T}^{1/2} \\ \nu_t^{S3QR} &= \left(C_{s3qr}\bar{\Delta}\right)^2 Q_{\mathrm{GG}^T}^{-1} R_{\mathrm{GG}^T}^{5/6} \end{aligned} \tag{6.53}$$

The model constant was found by Trias et al. by relating it with Vreman's model constant in order to assure numerical stability and a dissipation smaller or equal than the one in Vreman's model. According to this, the constant was found to be $C_{\mathrm{s3pqr}} = \sqrt{3}C_{Vr}$, and proved to be successful in the resolution of decaying isotrpic turbulence and a turbulent channel flow.

As previously seen for the Smagorinsky-Lilly model, its major drawback was the fact that the model did not vanish at the wall. Therefore, a good model should totally switch-off at the wall, and slowly increase its effect outside the viscous sub-layer. The wall-behaviour of the different models showed under the unified framework can be seen in the following table:

Wall-behaviour of each model				
Smagorinsky-Lilly	WALE	Vreman's	Verstappen's	S3PQR
$\mathcal{O}(y^0)$	$\mathcal{O}(y^3)$	$\mathcal{O}(y^1)$	$\mathcal{O}(y^1)$	$\mathcal{O}(y^3)$

Table 3: Near wall-baheviour of the Smagorinsky-Lilly, WALE, Vreman's, Verstappen's and S3PQR models

As it can be seen in the previous table, only the S3PQR and the WALE model exhibit a wall-behaviour of the order of $\mathcal{O}(y^3)$, while Vreman's and Verstappen's are of the order of $\mathcal{O}(y^1)$. The Smagorinsky-Lilly, as stated previously, is the one that has the worst wall-behaviour, only of the order of $\mathcal{O}(y^0)$. Another important factor regarding the models is the fact that the eddy viscosity should be null for 2D flows, or in other words, the model should totally vanish for bidimensional flow configurations. This property is only satisfied by Verstappen's and for the S3PQR models.

7 Natural laminar convection in square heated cavity

The first case solved is the study of natural convection inside a square cavity with heated walls. It is considered laminar flow and incompressible Newtonian fluid inside the cavity. Heat transfer due to radiation is totally neglected. Additionally, Boussinesq's approximation is used to consider that differences in density are neglected in all the terms, except on the buoyancy force when it is multiplied by $\boldsymbol{g}$. Non-dimensional equations are considered in this case, but using the following non-dimensional variables instead:

$$\boldsymbol{r}^* = \boldsymbol{r}/L \qquad \mathbf{v}^* = \mathbf{v}\frac{L}{\alpha} \qquad T^* = \frac{T - T_c}{T_h - T_c} \qquad p^* = \frac{pL^2}{\rho\alpha^2} \tag{7.1}$$

Therefore, the non-dimensional equations that are considered are the following:

$$\nabla^* \mathbf{v}^* = 0 \tag{7.2}$$

$$\frac{D\mathbf{v}^*}{Dt^*} = -\nabla^* p^* + Pr\nabla^{*2}\mathbf{v}^* + RaPrT^*\mathbf{k} \tag{7.3}$$

$$\frac{DT^*}{Dt^*} = \nabla^{*2}T^* \tag{7.4}$$

In which the vector $\mathbf{k}$ in the momentum equation is equal to $\mathbf{k} = (0, 1, 0)^T$. The energy equation is space-discretised in the same manner as the momentum equation, implying that the same symmetry-preserving discretization for the operators is used. In terms of the time integration method, both the diffusive and convective terms are grouped and discretised with a second order Adams-Bashforth scheme, while the transient term is discretised using a second order central difference scheme like in the momentum equation. The Conjugate Gradient solver is used as a solver for the Poisson equation.

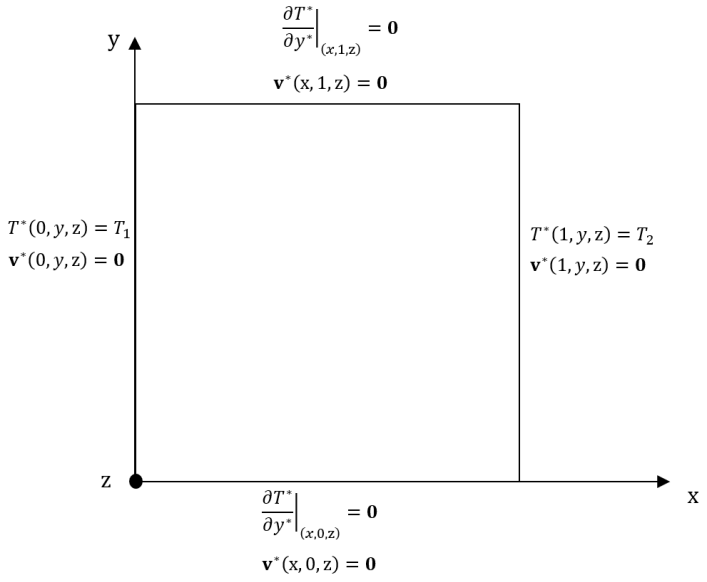

Figure 18: Boundary conditions of the natural laminar convection in square heated cavity problem

The problem is defined in a similar manner as in [7]. A square cavity with dimensions $0 \leqslant x \leqslant 1$, $0 \leqslant y \leqslant 1$, $0 \leqslant z \leqslant 1$ is considered. For the top and bottom walls at $(x, y = 0, 1, z)$, Dirichlet boundary conditions are used for the non-dimensional velocity, while Neumann boundary conditions are used for the non-dimensional temperature. For the vertical walls at $(x = 0, 1, y, z)$, Dirichlet boundary conditions are used for both the non-dimensional temperature and the non-dimensional velocity. For the vertical walls at $(x, y, z = 0, 1)$, periodic boundary conditions are imposed. The Prandtl number is set to $Pr = 0.71$, and the problem is solved for different Rayleigh numbers of $Ra = 1e3$, $Ra = 1e4$, $Ra = 1e5$ and $Ra = 1e6$.

The mesh employed is a uniform mesh of $64 \times 64 \times 3$ control volumes. Only 3 control volumes are used in the z direction given the fact that the problem considered is laminar. For each of the previous Rayleigh numbers, the non dimensional temperature field and non dimensional velocity modulus is shown in the figures below:

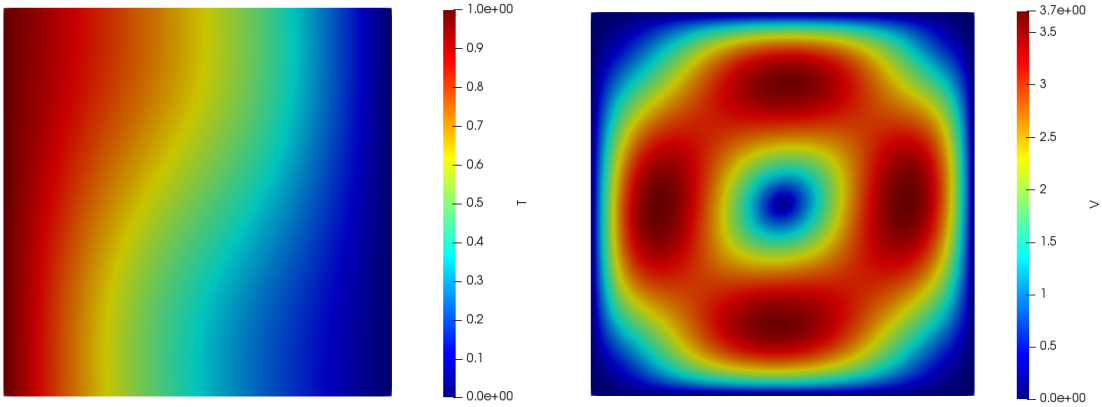

Figure 19: Non-dimensional temperature (left) and non-dimensional velocity modulus for $Ra = 1e3$

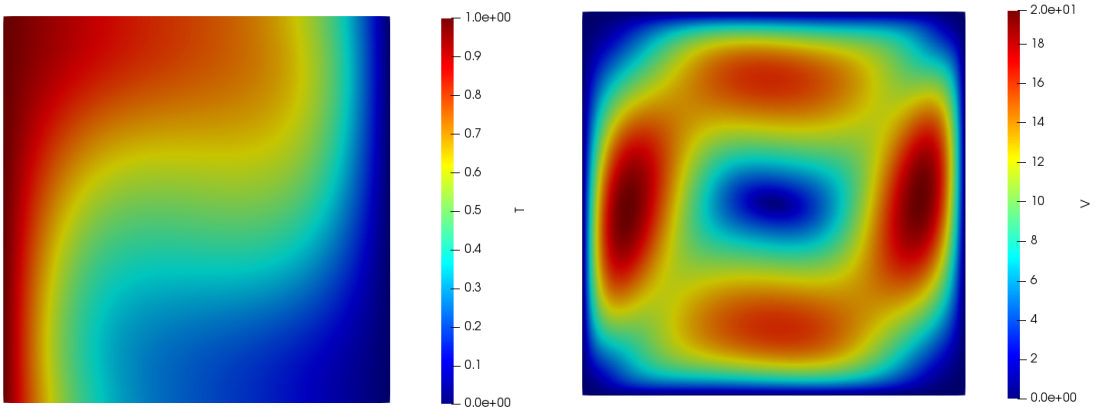

Figure 20: Non-dimensional temperature (left) and non-dimensional velocity modulus for $Ra = 1e4$

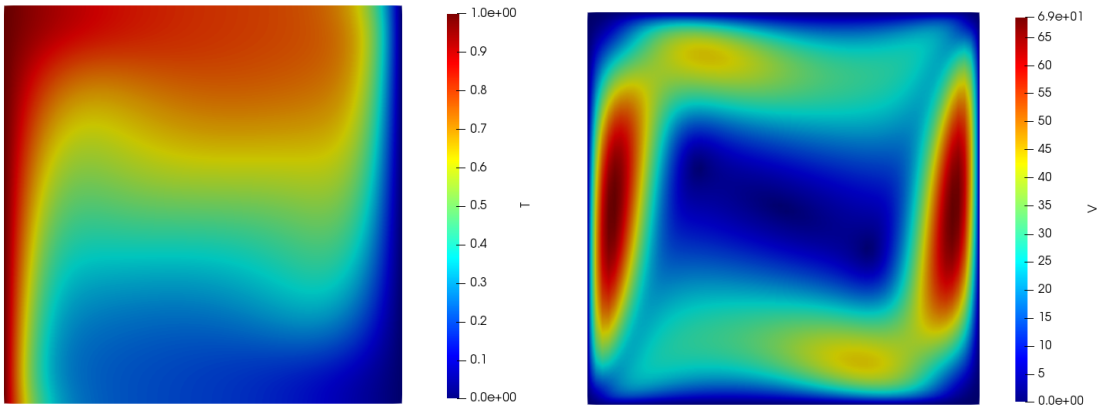

Figure 21: Non-dimensional temperature (left) and non-dimensional velocity modulus for $Ra = 1e5$

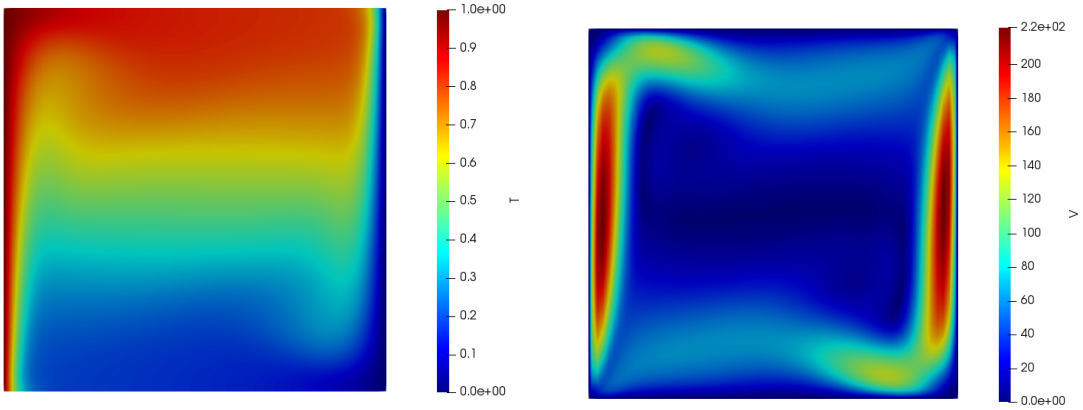

Figure 22: Non-dimensional temperature (left) and non-dimensional velocity modulus for $Ra = 1e6$

As it can be easily seen, for a Rayleigh number of $Ra = 1e3$, the isotherms are similar to a case of pure conduction. See for instance [27]. This is given due to the fact that conduction is the dominant heat transport mechanism. Isotherms, however, appear to be slightly curved due to the fact that buoyancy forces are being considered. As the Rayleigh number increases, it can be seen how the isotherms flatten at the centre of the cavity as thermal transport by convection dominates over thermal transport by diffusion. As a result, as the Rayleigh number increases, larger temperature and velocity gradients are observed at the hot and cold walls of the cavity.

Next, in terms of other important numerical results, the following parameters are computed in order to compare the data obtained in the present study with the data from [7]: maximum horizontal non-dimensional velocity component on the vertical mid-plane of the cavity ($u^*_{max}(0.5, y, z)$), and its location ($y_{u^*_{max}}$), maximum vertical non-dimensional velocity component on the horizontal mid-plane of the cavity ($v^*_{max}(x, 0.5, z)$), and its location ($x_{v^*_{max}}$), the average x-component of the Nusselt number on the vertical wall at $x = 0$ (Nu_0), the average x-component of the Nusselt number at the vertical mid-plane of the wall ($Nu_{1/2}$), the maximum value of the x-component of

the local Nusselt number at the vertical wall at $x = 0$, ($Nu_{max}(0, y, z)$) and its location ($y_{Nu_{max}}$), the minimum value of the x-component of the local Nusselt number at the vertical wall at $x = 0$, ($Nu_{min}(0, y, z)$) and its location ($y_{Nu_{min}}$).

The local x-component of the Nusselt number can be computed as the dimensionless heat flux, i.e:

$$Nu_x(x, y) = u^*T^* - \frac{\partial T^*}{\partial x^*} \tag{7.5}$$

While its average value on a vertical line can be computed as a line integral according to:

$$Nu_x(x) = \int_0^1 Nu_x(x, y)dy \tag{7.6}$$

Table 4: Results for the natural convection in square heated cavity for $Ra = 1e3$, and comparison with benchmark results from [7] (I)

	$\boldsymbol{Ra = 1e3}$				
	$\boldsymbol{u^*_{max}(0.5, y, z)}$	$\boldsymbol{y_{u^*_{max}}}$	$\boldsymbol{v^*_{max}(x, 0.5, z)}$	$\boldsymbol{x_{v^*_{max}}}$	$\boldsymbol{Nu_{1/2}}$
Benchmark	3.649	0.813	3.697	0.178	1.118
Results	3.646	0.820	3.697	0.180	1.118
Error(%)	0.00	0.86	0.00	1.11	0.00

Table 5: Results for the natural convection in square heated cavity for $Ra = 1e3$, and comparison with benchmark results from [7] (II)

	$\boldsymbol{Ra = 1e3}$				
	$\boldsymbol{Nu_0}$	$\boldsymbol{Nu_{max}(0, y, z)}$	$\boldsymbol{y_{Nu_{max}}}$	$\boldsymbol{Nu_{min}(0, y, z)}$	$\boldsymbol{y_{Nu_{min}}}$
Benchmark	1.117	1.505	0.092	0.692	1
Results	1.118	1.509	0.084	0.691	0.992
Error(%)	0.09	0.26	8.70	0.14	0.80

Table 6: Results for the natural convection in square heated cavity for $Ra = 1e4$, and comparison with benchmark results from [7] (I)

	$\boldsymbol{Ra = 1e4}$				
	$\boldsymbol{u^*_{max}(0.5, y, z)}$	$\boldsymbol{y_{u^*_{max}}}$	$\boldsymbol{v^*_{max}(x, 0.5, z)}$	$\boldsymbol{x_{v^*_{max}}}$	$\boldsymbol{Nu_{1/2}}$
Benchmark	16.178	0.823	19.617	0.119	2.243
Results	16.171	0.820	19.619	0.117	2.247
Error(%)	0.04	0.36	0.01	1.68	0.18

Table 7: Results for the natural convection in square heated cavity for $Ra = 1e4$, and comparison with benchmark results from [7] (II)

	$Ra = 1e4$				
	Nu_0	$Nu_{max}(0,y,z)$	$y_{Nu_{max}}$	$Nu_{min}(0,y,z)$	$y_{Nu_{min}}$
Benchmark	2.238	3.528	0.143	0.586	1
Results	2.251	3.551	0.148	0.585	0.993
Error(%)	0.58	0.65	3.50	0.17	0.70

Table 8: Results for the natural convection in square heated cavity for $Ra = 1e5$, and comparison with benchmark results from [7] (I)

	$Ra = 1e5$				
	$u^*_{max}(0.5,y,z)$	$y_{u^*_{max}}$	$v^*_{max}(x,0.5,z)$	$x_{v^*_{max}}$	$Nu_{1/2}$
Benchmark	34.730	0.855	68.590	0.066	4.519
Results	34.791	0.852	68.448	0.070	4.553
Error(%)	0.18	0.35	0.21	6.1	0.75

Table 9: Results for the natural convection in square heated cavity for $Ra = 1e5$, and comparison with benchmark results from [7] (II)

	$Ra = 1e5$				
	Nu_0	$Nu_{max}(0,y,z)$	$y_{Nu_{max}}$	$Nu_{min}(0,y,z)$	$y_{Nu_{min}}$
Benchmark	4.509	7.717	0.081	0.729	1
Results	4.562	7.908	0.071	0.725	0.993
Error(%)	1.17	2.48	12.35	0.55	0.70

Table 10: Results for the natural convection in square heated cavity for $Ra = 1e6$, and comparison with benchmark results from [7] (I)

	$Ra = 1e6$				
	$u^*_{max}(0.5,y,z)$	$y_{u^*_{max}}$	$v^*_{max}(x,0.5,z)$	$x_{v^*_{max}}$	$Nu_{1/2}$
Benchmark	64.63	0.850	219.36	0.0379	8.799
Results	65.49	0.852	221.61	0.039	9.054
Error(%)	1.33	0.24	1.03	2.90	2.90

Table 11: Results for the natural convection in square heated cavity for $Ra = 1e6$, and comparison with benchmark results from [7] (II)

	$Ra = 1e6$				
	Nu_0	$Nu_{max}(0,y,z)$	$y_{Nu_{max}}$	$Nu_{min}(0,y,z)$	$y_{Nu_{min}}$
Benchmark	8.817	17.925	0.0378	0.989	1
Results	9.069	19.241	0.024	0.965	0.993
Error(%)	2.86	7.34	36.51	2.43	0.70

As it can be seen by comparing the results obtained in the present study and the benchmark results from [7], really good agreement is obtained. It can be seen that larger errors are observed as the Rayleigh number increases, which might indicate that a finer mesh is needed. In terms of the results themselves, slight differences in the average Nusselt number computed at $x = 0$ and $x = 1/2$ are observed for both the benchmark results and the self obtained ones. The discrepancies must be due to numerical errors, as it is expected to obtain the same value for the Nusselt number regardless of the position in which it is measured. This is due to the fact that, given that the top and bottom walls of the cavity are adiabatic, the heat flow across any vertical line joining both walls must be the same, hence, leading to a same average Nusselt number independent of the x coordinate. Nevertheless, it is clear that as the Rayleigh number increases, the average Nusselt number in the x direction increases, indicating that convective heat transport becomes the dominant heat transport mechanism. The maximum local Nusselt number in the left wall also increases with the Rayleigh number. Its position slightly changes for each case studied, but it is located very near bottom vertex. The minimum value of the local Nusselt number on the same wall slightly decreases for $Ra = 1e4$, and then starts to increases for higher values of the Rayleigh number. However, it is always located at the top vertex. Maximum values for both the vertical and horizontal velocity components also increase with the Rayleigh number, which is totally expected as convection dominates.

8 Taylor-Green vortex

The Taylor-Green vortex (TGV) is a well known problem in computational fluid dynamics to study vortex dynamics and the energy decay process in turbulent flows due to the vortex stretching phenomenon. At the beginning, an initial vorticity distribution is given. However, as time advances, vortices start to roll-up, stretching and interacting between them, breaking up eventually. The problem consists on a cubic domain with periodic boundary conditions in all the directions, with dimensions $0 < x, y, z < 2\pi L$, where L is a characteristic length. An initial distribution of velocity, and hence, of vorticity, is given according to [28]:

$$u = U_0 sin\left(\frac{x}{L}\right) cos\left(\frac{y}{L}\right) cos\left(\frac{z}{L}\right) \tag{8.1}$$

$$v = -U_0 cos\left(\frac{x}{L}\right) sin\left(\frac{y}{L}\right) cos\left(\frac{z}{L}\right) \tag{8.2}$$

$$w = 0 \tag{8.3}$$

The initial pressure field is given by:

$$p = p_0 + \frac{\rho_0 U_0^2}{16}\left(cos\left(\frac{2x}{L}\right) + cos\left(\frac{2y}{L}\right)\right)\left(cos\left(\frac{2z}{L}\right) + 2\right) \tag{8.4}$$

Being U_0 and ρ_0 reference values for the velocity and density, although the flow is treated as incompressible. The problem is solved for a Reynolds number of $Re = 1600$ during 20 time units (TU), being a time unit defined as $TU = tU_0/L$.

During the simulation, the volume-averaged kinetic energy is computed as a function of time:

$$E_k = \frac{1}{\rho_0 \Omega}\int_\Omega \frac{1}{2}\rho(\mathbf{v}\cdot\mathbf{v})d\Omega \tag{8.5}$$

And the kinetic energy dissipation rate (KEDR) can be computed by differencing E_k in time:

$$\varepsilon(E_k) = -\frac{dE_k}{dt} \tag{8.6}$$

In the previous expression, the kinetic energy dissipation rate has been expressed as a function of E_k to note that it has been directly computed from the integrated kinetic energy.

Additionally, the integrated enstrophy is also computed as a function of time:

$$\zeta = \frac{1}{\rho_0 \Omega}\int_\Omega \rho\frac{\boldsymbol{\omega}\cdot\boldsymbol{\omega}}{2}d\Omega \tag{8.7}$$

Which can also be used to compute the kinetic energy dissipation rate as, for an incompressible fluid, it can be shown that:

$$\varepsilon(\zeta) = 2\frac{\mu}{\rho_0}\zeta \tag{8.8}$$

The kinetic energ dissipation rate is computed in both ways and compared with the reference solution from van Rees et al. [4], generated with a spectral method.

The equations are discretised with the symmetry-preserving scheme previously described, and the pressure velocity coupling is solved with the projection method, also outlined in the previous sections. The conjugate gradient method is used as a solver. First of all, the isosurface of the z-component of the vorticity ar plotted as a function of time for a mesh of $32 \times 32 \times 32$ control volumes.

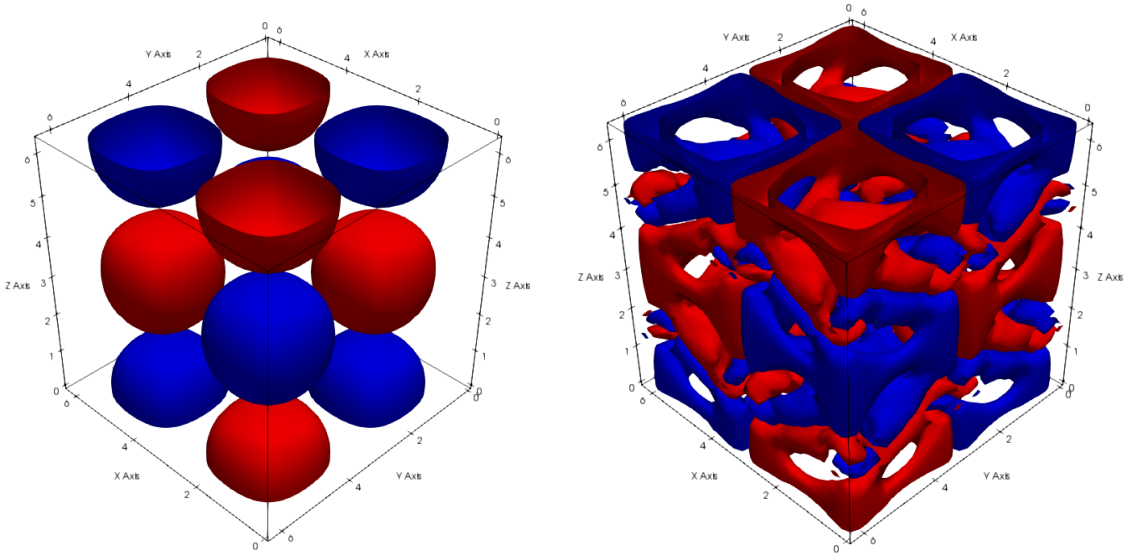

Figure 23: Isosurfaces of the z-component of the vorticity at $TU = 0$ (left) and at $TU \approx 5$. In blue $\omega_z = -0.7s^{-1}$ and in red $\omega_z = 0.7s^{-1}$

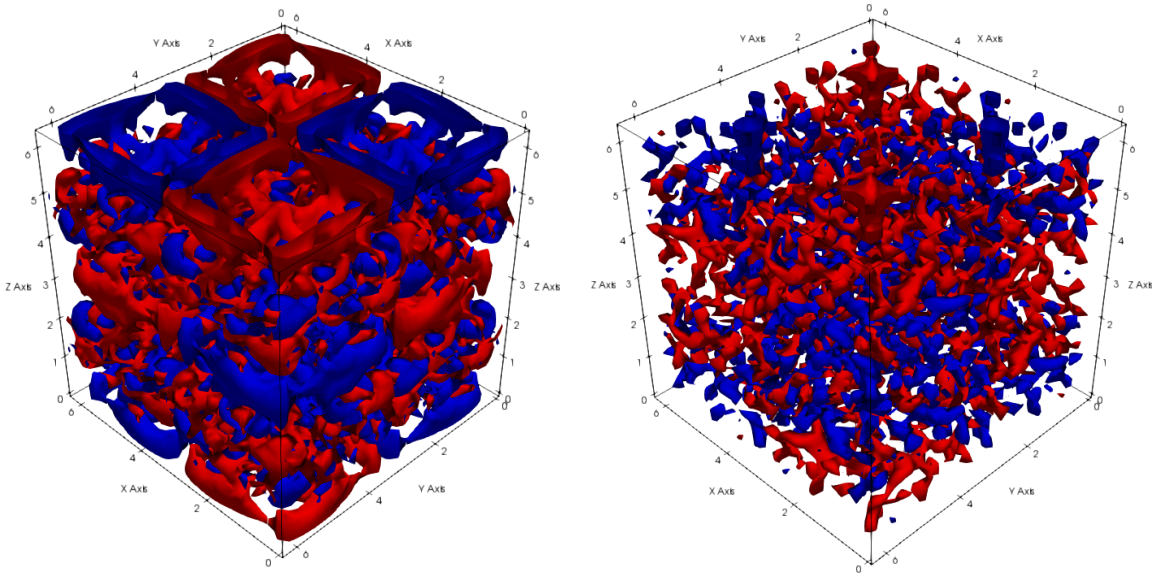

Figure 24: Isosurfaces of the z-component of the vorticity at $TU \approx 10$ (left) and at $TU \approx 20$. In blue $\omega_z = -0.7s^{-1}$ and in red $\omega_z = 0.7s^{-1}$

As it can be seen, after 5 TU, the velocity distribution retains some of the characteristics of the

initial velocity field. However, the vortices are already slightly stretched and start to interact between them. At TU=10, vortical structures start to break up and mix. After 20 time units, the flow is totally chaotic showing a lot of smaller vortices and a velocity distribution typical of turbulent flows.

Next, the volume-averaged kinetic energy is plotted as a function of the non-dimensional time and compared with the reference results from van Rees et al. [4].

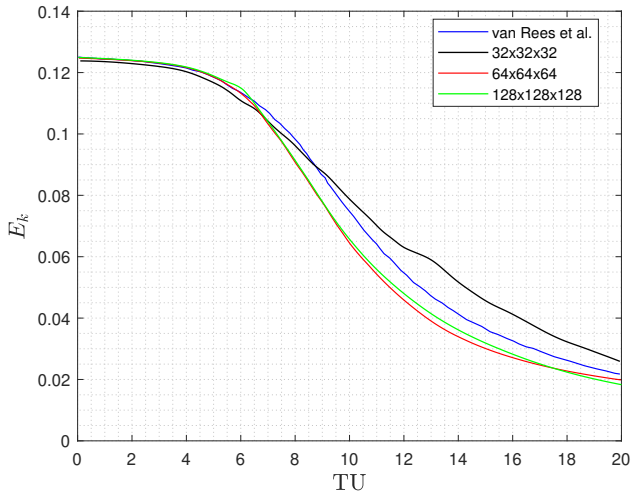

Figure 25: Volume-averaged kinetic energy of the Taylor-Green Vortex problem and comparison with results from van Rees et al. [4]

As it can be seen, the volume-averaged kinetic energy monotonously decreases, given the fact that there is no energy introduced into the system, and consequently, all the initial kinetic energy of the domain ends up being dissipated due to viscous effects. At the beginning, during the first 5 time units approximately, the volume-averaged kinetic energy remains nearly constant due to the fact that only big vortical structures are present. When the vortical structures start to stretch and interact between them, much smaller structures are being formed and the averaged kinetic energy starts to decrease more rapidly as dissipation happens in the smaller scales that are being created. This is clearly seen by the rapid kinetic energy decrease between 5 and 15 TU approximately. From this time on, only very small structures are present in the flow, and the rate at which the kinetic energy decreases reduces. The latter explanation can also be understood by analysing figure 26 , which shows the kinetic energy dissipation rate computed from the enstrophy ($\varepsilon(E_\zeta)$), and computed as the time derivative of the volume-averaged kinetic energy ($\varepsilon(E_k)$).

It can be seen how the KEDR computed from the volume-averaged kinetic energy shows better agreement with the results from van Rees et al. [4], even for coarser meshes. Nevertheless, it is interesting to notice how different the KEDR curves obtained with each mesh are, even though the time variation of the volume-averaged kinetic energy shown in figure 25 show similar results for all the meshes tested. On the other hand, the KEDR computed from the enstrophy shows lower values in comparison to their respective values of the $\varepsilon(E_k)$. However, the $\varepsilon(E_\zeta)$) profiles

obtained show much less spikes and a smoother variation, even though the peak in the KEDR is not correctly captured by any of the meshes employed, which indicates that the the results obtained are still far from a DNS results.

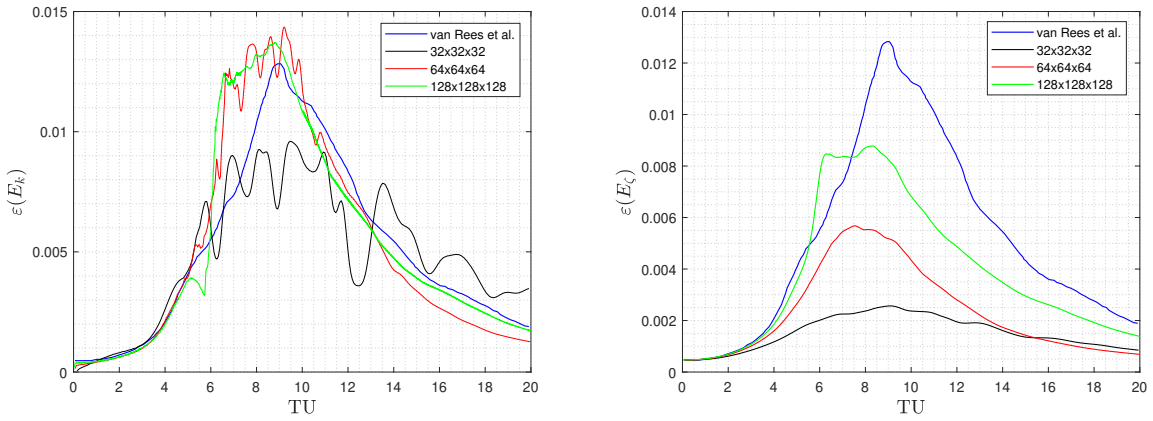

Figure 26: Kinetic energy dissipation rate of the Taylor-Green vortex problem. On the left, the KEDR computed as the derivative of the volume averaged kinetic energy. On the right, the KEDR computed from the enstrophy

9 Turbulent channel flow at $Re_\tau = 180$

The next benchmark problem solved is a turbulent channel flow with periodic boundary conditions in the streamwise and spanwise directions. The problem is sketched below:

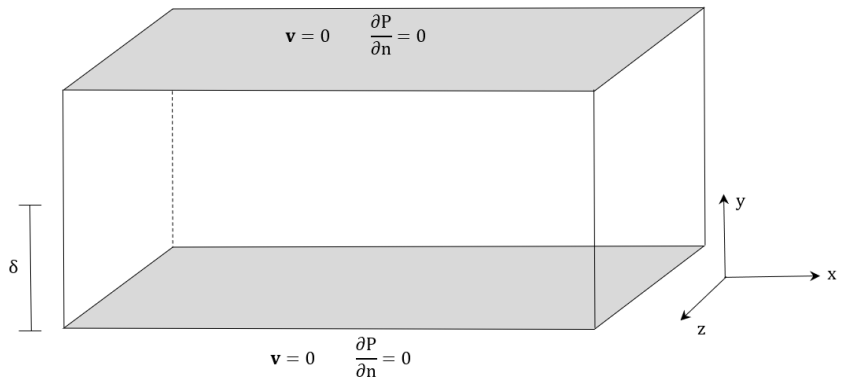

Figure 27: Schematic of the turbulent channel flow problem

As already stated, periodic boundary conditions are imposed in the streamwise (x) and spanwise (z) directions. At the top and bottom walls the non-slip condition is applied, hence, Dirichlet boundary conditions are set for the velocity vector, and Neumann boundary conditions for the pressure, as sketched above in figure 27. The channel dimensions are set at $4\pi \times 2 \times 2\pi$. Additionally, to impose the movement of the fluid in the streamwise direction, a constant pressure gradient of $\frac{\partial p}{\partial x} = -1$ is applied to the x-component of the momentum equation as a source term. Given that this a typical benchmark problem for wall-bounded turbulent flows, it is common to normalise the equations with the friction velocity u_τ (defined in equation 5.54) and the channel's half-width (δ). This allows to express the problem in terms of a friction Reynolds number Re_τ, defined as $Re_\tau = u_\tau \delta / \nu$. For this problem, the friction Reynolds is set to $Re_\tau = 180$.

In terms of numerical simulations performed, the problem is firstly solved with a direct numerical simulation (DNS) and verified with the data from Moser et al. [5]. Different meshes are employed for this first case, with grid points uniformly distributed in both the streamwise and spanwise directions, whereas for the wall-normal direction, grid points are distributed according to a piecewise hyperbolic sine functions, which, for the lower-half part of the channel reads the following:

$$y_j = \sinh(\gamma j / N_y) / \sinh(\gamma / 2) \quad j = 0, 1, ..., N_y/2 \tag{9.1}$$

where N_y denotes the total number of grid points employed in the wall-normal direction; and γ is the stretching parameter. The latter is set to 8.0, as it allows to place the first point in the wall-normal direction inside the viscous sub-layer ($y^+ < 5$). The points in the upper half of the channel are placed symmetrically to the lower ones with respect to the channel's centreline. The problem is also solved with the Smagorinsky, Vreman's and S3PR models. The subgrid characteristic length is computed as the minimum value of the cell size, i.e $\Delta \equiv min(\Delta x, \Delta y, \Delta z)$. Field averages are performed over the four statistically invariant transformations: time, streamwise, spanwise directions and central plane symmetry. Time averages are carried out after an

initial start-up period, and the time-span over which the fields are averaged is equal to 60-time units (based on the friction velocity u_τ and the channel's half-width).

9.1 DNS results

First of all, the *rms* values of the fluctuating velocity components obtained with 5 different meshes are shown and compared with the DNS data from Moser et al. [5].

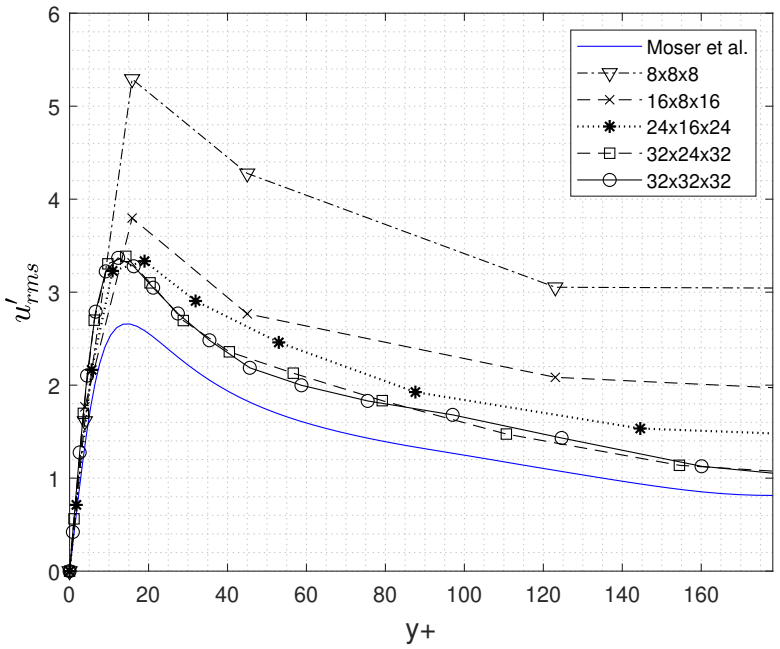

Figure 28: u'_{rms} velocity profile for different meshes in wall-units for $Re_\tau = 180$ and comparison with results from [5]

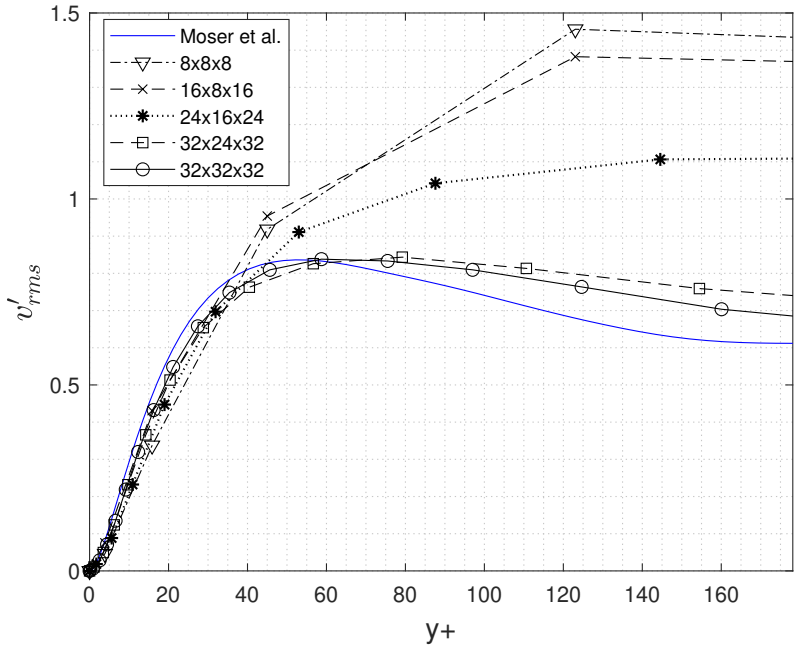

Figure 29: v'_{rms} velocity profile for different meshes in wall-units for $Re_\tau = 180$ and comparison with results from [5]

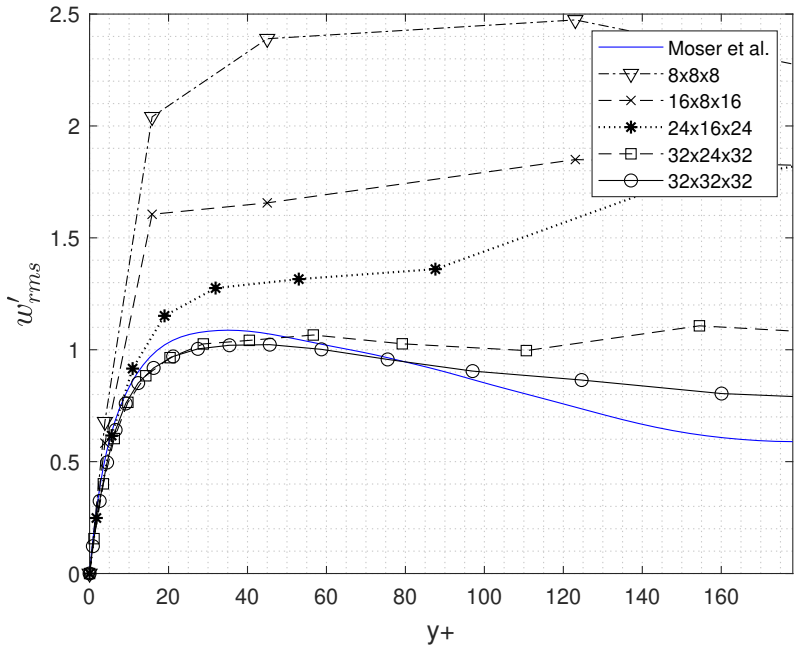

Figure 30: w'_{rms} velocity profile for different meshes in wall-units for $Re_\tau = 180$ and comparison with results from [5]

As it can be seen in the previous plots showing the root-mean-square of the fluctuating velocity components, there is relatively good agreement with the reference results from Moser et al. [5] for all the points near the wall. This is due to the fact that more points are located in this region according to the hyperbolic sine function law previously described and also because by imposing the friction Reynolds, the shear stress in the wall is also imposed. However, for higher y^+ values and as we get close to the channel's centreline, in general, larger errors are observed for all three profiles. Nevertheless, it can be clearly seen how, as the mesh improves, the obtained velocity profiles start to resemble the ones obtained with a full DNS simulation. With a 32^3 mesh and, without using any turbulence model, there is good agreement with the reference results taking into account how coarse the mesh used is. The solution obtained for the u'_{rms} profile correctly predicts the position of the peak, but over-predicts its value in the whole domain. Regarding the results of the v'_{rms} and w'_{rms} velocity profiles, the peak values are relatively well-predicted with the 32^3 mesh. However, their values are slightly under-predicted inside the viscous sub-layer and buffer layer, and start to be over-predicted for y^+ values higher than 110, approximately. The data of table 12 shows the maximum absolute error observed for each rms profile of the fluctuations taking as a reference solution the results from Moser et al. [5], and the position of the maximum error observed, in wall units; where ε_u, ε_v, ε_w, $y^+_{\varepsilon_u}$, $y^+_{\varepsilon_v}$ and $y^+_{\varepsilon_w}$ represent the absolute errors observed for each profile and its location, respectively.

Table 12: Maximum absolute errors of the root-mean square of the fluctuating velocity components and position of the maximum errors

Mesh	$\boldsymbol{\varepsilon_u}$	$\boldsymbol{y^+_{\varepsilon_u}}$	$\boldsymbol{\varepsilon_v}$	$\boldsymbol{y^+_{\varepsilon_v}}$	$\boldsymbol{\varepsilon_w}$	$\boldsymbol{y^+_{\varepsilon_w}}$
8x8x8	2.496	45.000	0.742	123.038	1.525	123.038
16x8x16	1.246	15.837	0.688	123.034	1.073	123.034
24x16x24	0.738	18.983	0.472	144.556	1.171	144.556
32x24x32	0.699	9.697	0.116	154.467	0.458	154.467
32x32x32	0.465	9.159	0.128	27.432	0.177	160.077

According with the results shown in the previous table, it can be seen how the largest absolute errors are produced for the streamwise velocity fluctuations. The rms values of the fluctuations of the wall-normal velocity profile show surprisingly good agreement with the reference results, even with the coarsest mesh used, while for the spanwise velocity fluctuations, the absolute error observed lays between the previous two, except for the 24x16x24 mesh. It is also interesting to notice the location where the maximum errors are observed. It can be seen how the maximum error obtained for the fluctuations in the streamwise velocity component happens inside the buffer layer for all the meshes tested except for the coarsest mesh employed, in which the maximum error is observed in the log-law region. However, for the fluctuations in the wall-normal and spanwise velocity components, the larger errors are obtained close to the channel's centreline in the outer layer or core region, except for the ε_v error for the 32^3 mesh, which is observed in the buffer layer. This is a clear indicator that more points are needed close to the channel's centreline, given that the hyperbolic sine law used makes the spacing between the channel's centre nodes to large to properly capture the flow behaviour in this region.

Similar conclusions can be obtained by analysing figure 31, in which the mean velocity profile is graphed in wall units. First of all, it must be noticed that for all the meshes used, the first

point in the wall-normal direction lays inside the viscous sub-layer. For the coarsest mesh, it is located at $y^+ = 3.88$, while for the finest mesh used it is positioned at $y^+ = 0.833$. Regarding the comparison with the DNS results from Moser et al. [5], it can be seen that, regardless of the mesh employed, there is good agreement for the points located inside the viscous sub-layer and initial part of the buffer layer, while higher discrepancies are observed as we move towards the channel's centreline. For all the meshes tested and, except for the last point of the 16x8x16 mesh, the velocity profile is slightly over-predicted for $y^+ > 5$, which once again indicates that more points are needed in the wall-normal direction.

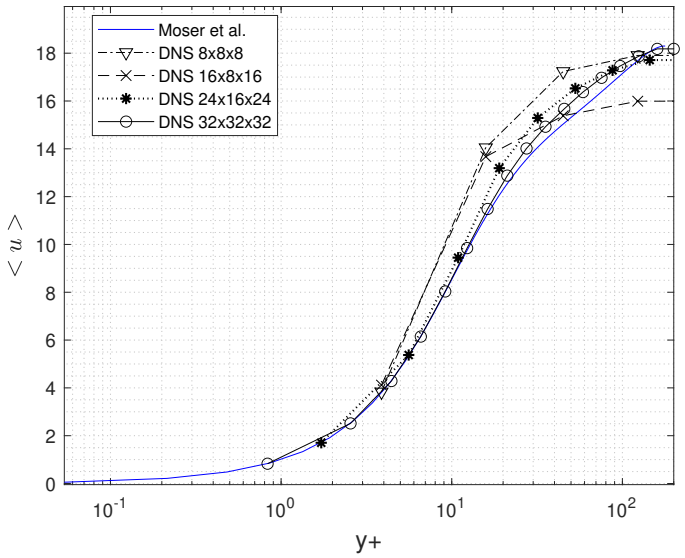

Figure 31: Mean velocity profile in wall-units for $Re_\tau = 180$ and comparison with results from [5]

Figure 32 shows the mean total, turbulent and viscous shear stresses. The first thing to notice is that just at the wall, the mean shear stress, corresponding to the value of τ_w, is equal to one, which is totally expected given that the value of the Re_τ was imposed. However, at the beginning of the buffer layer region, a slight overshoot in the total shear stresses is observed, which might be attributed to a lack of mesh refinement in this zone. Nevertheless, this difference is not too considerable and the solution obtained is still acceptable, as it perfectly allows to understand the flow behaviour near the wall. The different sub-divisions of the turbulent boundary layer are also shown, which helps to get a better understanding of the law of the wall. As it can be seen, in the viscous sub-layer, viscous shear stresses predominate due to the the rapid change in the average fluid velocity in the direction normal to the wall. Nevertheless, given that some turbulent shear stresses, although very small, are still present, the flow in this region can not be considered strictly laminar. After the viscous sub-layer, the buffer layer zone can be clearly distinguished as both the turbulent and viscous shear stresses are both too important to be ignored. Finally, in the log-law region, turbulent shear stresses dominate, while viscous shear stresses are nearly damped to zero. Consequently, when both components of the shear stress are combined together in all the three regions a near linear variation in the total mean shear stress is observed.

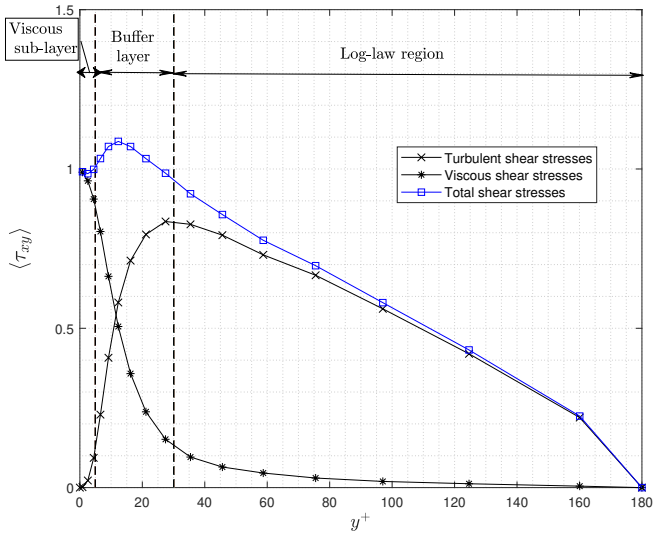

Figure 32: Mean shear stresses for $Re_\tau = 180$ and a 32^3 mesh without model

9.2 LES results

Once the turbulent channel flow problem was solved without any turbulence model, the same problem was solved applying three different LES eddy-viscosity models: the Smagorinsky, Vreman's and S3PR models, as each of them exhibits a different near-wall behaviour. First of all, in order to test the proper implementation of the different models, the average eddy-viscosity $\langle \nu_t \rangle$ divided by the kinematic viscosity ν is graphed in the following figure:

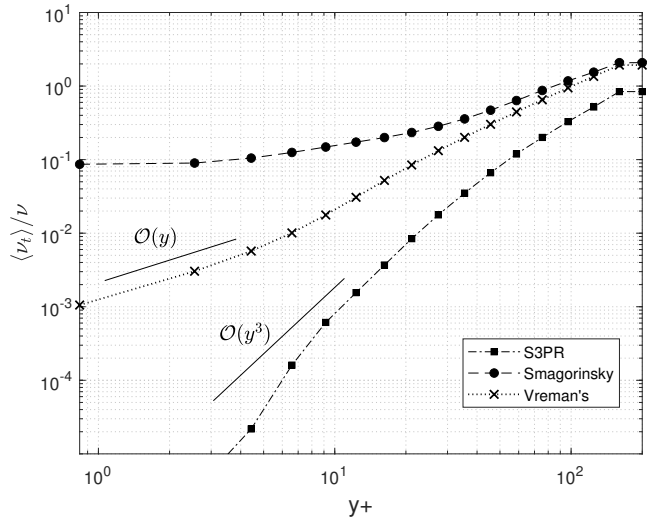

Figure 33: Mean eddy-viscosity $\langle \nu_t \rangle$ divided by the kinematic viscosity ν. Results for a turbulent channel flow at $Re_\tau = 180$ obtained with a 32^3 mesh for different LES models

As it can be seen, the $S3PR$ model shows a cubic behaviour in the near wall region as expected according to the studies from Trias et al. [26], while Vreman's model tends to add more dissipation in the buffer layer in comparison, showing a first order behaviour. Finally, the Smagorinsky model presents an $\mathcal{O}(y^0)$ behaviour, which implies that the eddy-viscosity does not vanish at the wall.

Next, the root-mean-square values of the fluctuating velocity components are plotted in figure 34 and compared with the DNS results from Moser et al. [5] for the S3PR, Smagorinsky and Vreman's model. Regarding the comparison with the three models used, it can be seen how the S3PR model, in comparison to the other two, shows a better performance in the buffer layer region. This can be explained given the better near-wall behaviour that the S3PR model has, while Vreman's, and specially the Smagorinsky model, tend to over-dissipate in the near-wall region. However, it is interesting to notice how, at the core region of the flow, the Smagorinsky model is the one that shows better results. This could be attributed to the fact the latter shows a larger eddy-viscosity in the outer layer region in comparison to the other two models tested, as shown in figure 33.

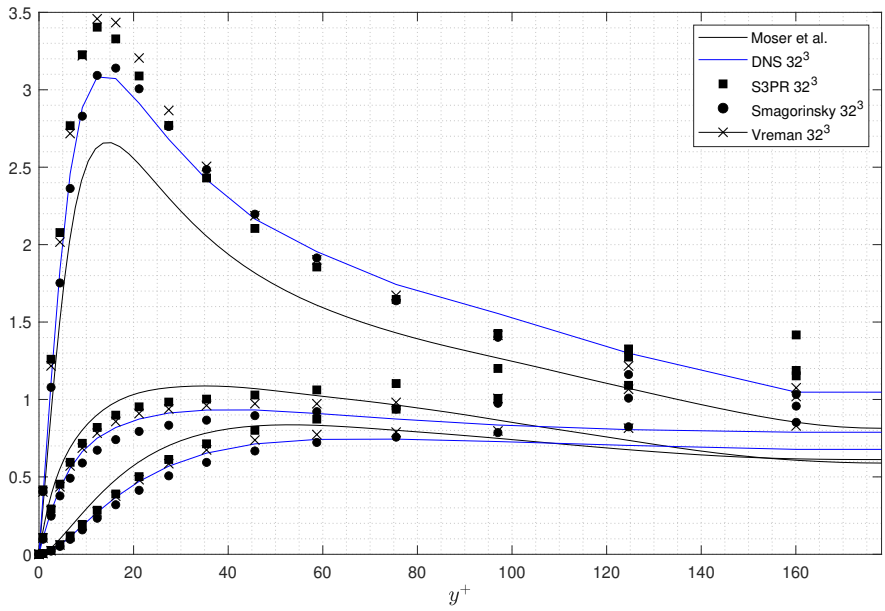

Figure 34: Root-mean-square of the fluctuating velocity components for a turbulent channel flow at $Re_\tau = 180$ obtained with a 32^3 mesh for different LES models, and comparison with the DNS results from Moser et al. [5]. From top to bottom u'_{rms}, v'_{rms} and w'_{rms} respectively.

Next, the results obtained with these models are compared with the DNS results obtained for the same mesh. The S3PR model shows and over-prediction for the u'_{rms} profile in the buffer layer region. Although the position of the peak value of the the rms of the fluctuations is correctly predicted, its value is even higher than the one obtained with the DNS simulation. However, between $35 < y^+ < 125$, the values of the u'_{rms} are considerably improved. From $y^+ > 125$, an over-prediction of the rms of the streamwise velocity fluctuations is observed again. Regarding

the results for the v'_{rms} and w'_{rms}, the S3PR model improves the results in the buffer layer region considerably, but over-predicts the rms values in the core region in comparison to the DNS results obtained.

The Smagorinsky model shows very similar results to the DNS simulation for the u'_{rms} velocity profile in the buffer layer region, but improves the solution for $y^+ > 45$. However, the model does not improve the results of the DNS simulation neither in the buffer layer region, nor in the outer layer of both the root-mean-square values of the spanwise and wall-normal velocity fluctuations.

Finally, Vreman's model shows an intermediate behaviour between the S3PR and the Smagorinsky model. The model correctly predicts the peak position for the u'_{rms} velocity profile, but the peak value obtained is even higher than the one obtained in the SP3R simulation. For the v'_{rms} profile, improvements in the results are only present in the buffer layer. The root-mean-square values of the fluctuations of the spanwise velocity component show very similar results to the DNS simulation in the buffer layer, but important discrepancies in the core region.

All in all, it can be seen how, among the three models tested, only the S3PR and Vreman's model improved the results in the buffer layer, being the former the most suitable one given its near-wall behaviour. However, the three models tested worsen the results in the core region of the channel in comparison to the DNS results obtained with the same mesh, being the Smagorinsky model the one that worsens the less in this region, probably due to its larges eddy-viscosity in that part of the domain. This behaviour could probably be improved by a better tuning of the models, and further test should be done as a future research to see if the results could be further improved for the same mesh.

10 Conclusions and future work

As already stated at the begining of the thesis, the objective of the present study was the elaboration, validation and verification of $C++$ codes to solve the incompressible Navier-Stokes equations under turbulent regime, by applying a symmetry-preserving discretization. The code has been tested by solving the well-known problem of a turbulent channel flow and thus, it can be concluded that the general objectives set before the development of the thesis have been accomplished. Additionally, the development of this study has been useful to get a better understanding of the physics behind turbulent flows and how they can be modelled.

First of all, it has been observed how important it is to preserve the symmetry of all the operators involved in the spatial discretization of the Navier-Stokes equations in order to avoid the artificial introduction or the dissipation of kinetic energy into the system. Verstappen et al. [15] propose a fourth order symmetry preserving discretization. However, given its higher complexity, a second order model was used in this thesis, which was properly verified.

Next, the classical approach to tackle turbulence has been briefly studied through the concept of the energy cascade. It has been observed how the larger scales of a turbulent flow, which are anisotropic and problem-dependent, transfer energy to smaller and smaller scales, until reaching sufficiently smaller eddies, which have an isotropic behaviour and whose Reynolds number is small enough so that this energy ends up being dissipated due to viscous effects.

The statistical description of turbulent flows has also been discussed, and the turbulence modelling problem has firstly been approached by considering the Reynolds-averaged Navier Stokes equations (RANS). Different eddy viscosity models have been overviewed to tackle the closure problem, such as the mixing-length model, the $k-\varepsilon$, Spalart-Allmaras and Wilcox $k-\omega$ models. However, it has been observed that, due to the fact that the RANS equations intend to model the overall behaviour of all the eddies of the flow, a general model that works properly for a wide range of flow configurations is difficult to find. On the other hand, the principles behind the Large Eddy Simulation (LES) have also been reviewed, and how the equations can be space-filtered by using different filters. Special emphasis has been put in how the non-linear term that appears in the filtered equations can be treated, and in how to model the interactions between the larger and smaller scales of the flow with various eddy viscosity models, such as the Smagorinsky, WALE, Vreman's, Verstappen's and the S3PQR models developed by Trias et al. [26], emphasising their near-wall behaviour.

Regarding the results of the Taylor-Green vortex problem, good agreement has been observed with the results of van Rees et al. [4] regarding the time evolution of the volume-averaged kinetic energy, even for coarser meshes. The kinetic energy dissipation rate (KEDR) was also computed as a function of time by differentiating the kinetic energy and also by making use of the enstrophy. Both approaches failed to correctly capture its peak value in time. However, the second approach showed a smoother variation of the KEDR, while the first one obtained peak values closer to the peak value of the reference results. The isosurface of the z-component of vorticity plotted for four different time units allowed to visualize how the main vortexs stretch and start to interact between them, breaking up and eventually obtaining a velocity distribution typical of turbulent flows.

Finally, a turbulent channel flow problem for $Re_\tau = 180$ was also studied. Firstly, DNS results were obtained with different meshes. Root-mean-square values of the fluctuating velocity components and the mean velocity profile in wall units were computed, obtaining considerably good agreement with the results of Moser et al. [5] for a mesh of 32^3. The maximum absolute error regarding the u'_{rms} values was observed in the buffer-layer region for the finest mesh employed, while the rms values of the wall-normal and span-wise velocity fluctuations showed a maximum error in the latest part of the buffer layer region and core region respectively, indicating that a finer mesh is needed to place more control volumes close to the channel's centerline. Finally, the S3PR, Smagorinsky and Vreman's model were programmed and compared. While the three models tested failed to improve the results observed in the core region of the flow, except for the fluctuations in the stream-wise direction, the S3PR model improved the results considerably in the buffer-layer region given its third order near-wall behaviour. On the other hand, Vreman's model also improved the results in the buffer layer, although to a lesser extent given that the model tends to add more dissipation in this region. Finally, the Smagorinsky model did not improve the results neither in the buffer layer, nor in the core region, except for the u'_{rms} velocity profile for which the model slightly improved the results in the outer layer. However, the latter was the one that worsened the less in the core region, probably due to the fact that a larger eddy-viscosity was introduced in that part of the domain in comparison to the other models.

Regarding the future work to be done, it could be interesting to try to better tune the different LES models used to see if better results could be obtained for the same meshes employed. Additionally, the parallelization of the code is a fundamental topic in order to be able to solve problems with finer meshes, as solving all the problems with only 1 CPU was a limiting case. Additionally, investigation in regards to more efficient solvers should also be done, which might also improve the overall performance of the code. Moreover, the implementation of unstructured meshes is also an important topic that should be studied in order to simulate flows around more complex geometries.

11 Task planning

The Gantt chart presented in the following page is an initial schedule that was done at the start of the thesis. It must be noticed that the Gantt chart was modified during the development of the project to account for all the minor problems encountered during the development of the study.

The preliminary code modifications took slightly longer than expected. Even though the extension of the code developed during the Bachelor's thesis took shorter than planned, the symmetry-preserving discretization took a bit longer than expected to verify.

Regarding the DNS simulations of the turbulent channel flow, those also took longer than expected due to minor issues regarding the computation of the statistics of the flow. On the other hand, even though the implementation of the LES models did not take much, the simulations took considerably longer than planned given the high computational resources required.

Regardless of everything mentioned above, the general schedule that was followed is presented in the following page:

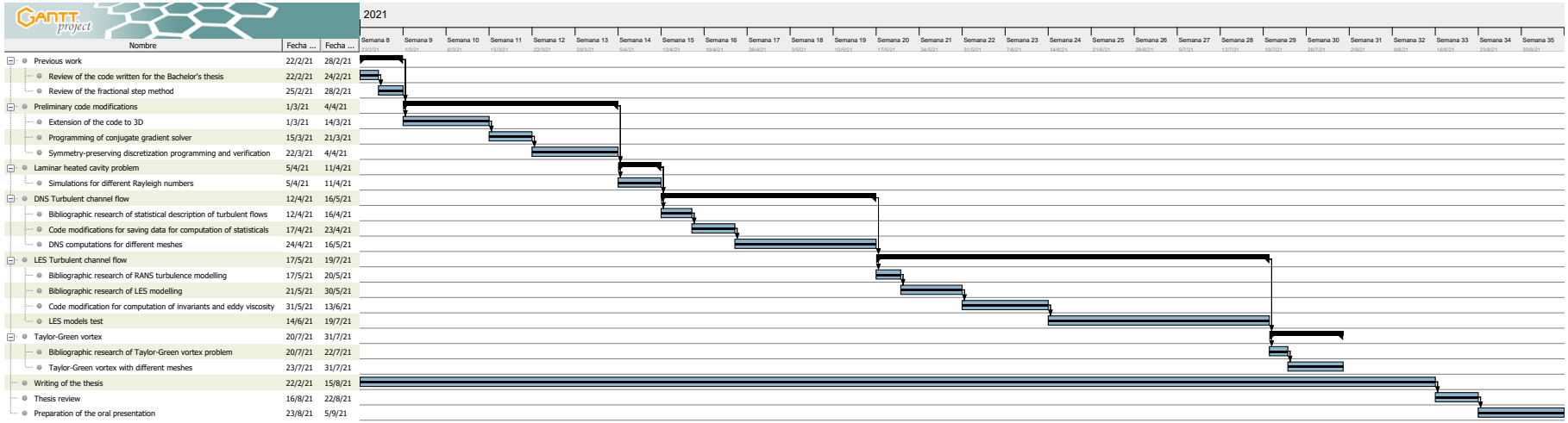

Figure 35: Gantt chart

12 Budget of the study

The following section is a brief estimation of the cost that a study like the present could have. Therefore, the reader should not consider this budget as a detailed breakdown of the cost that each project sub-task had, as the following estimations have been made:

- The present study is a thesis for the obtainment of the Master's degree in aeronautical engineering. Therefore, the hourly price for the elaboration of the present study has been considered taking into account the salary that a recently graduated aerospace engineer with no previous experience could have. With this, and taking into account that this is just a thesis and not a full-time job, the hourly price is estimated to be around 10.6 €/hour [29].

- The price of all the software used for the thesis development also needs to be considered. The development of all the codes has been done with *DevC++*, which is a free and full-featured IDE (Integrated Development Environment). All the line plots have been done with *Matlab*, whose annual educational license price is of 250€ [30]. However, given that the university provides a key license for the students, its use has been totally free throughout the duration of the project. On the other hand, all the data visualization and colour plots have been obtained with *Paraview*, which is an open-source multiple-platform application and hence, totally free. The self-drawn figures have been made with *Microsoft Word*, whose educational Office 365A1 plan is free for students. Finally, the thesis has been written with the free plan of the collaborative cloud-based LaTeX editor *Overleaf*. Therefore, all the software employed in the development of this study has been free to use.

- The price of the hardware is another important part of the total cost of the project, and hence, it should be taken into account. Considering that the price of the laptop used to write all the code and run all the simulations is about 1900€, and assuming its lifetime to be of about 5 years, the cost of its use during the development of the thesis can be estimated to be about 221.69 €. Additionally, an external monitor with a price of 300 € has also been employed. Assuming the same lifetime, its cost of use is about 35€ for its use during the whole study.

- Finally, the price of the electricity is an important part in the overall budget of the study. This needs to include not only the electricity consumption of the computer and the external screen, but also the consumption due to lighting and room acclimatisation, given that the majority of the work has been done during the winter and spring times. To do so, the average cost of 1 $kW \cdot h$ is estimated to be about $0.25€/kW \cdot h$ considering all the fees and taxes added to the baseline price. The lighting consumption is estimated to be around $0.06kW \cdot h$, while the consumption of the computer and the external screen is estimated to be around $0.3kW \cdot h$.

Therefore, the breakdown of the total costs can be easily seen with the following tables grouping the hardware cost, software costs, lighting and acclimatisation costs and salary:

Table 13: Software cost breakdown

Software	Monthly cost	Total cost
Dev C++	0.00 €	0.00 €
Matlab (student's license)	0.00 €	0.00 €
Paraview	0.00 €	0.00 €
Office 365 A1	0.00 €	0.00 €
Overleaf (free plan)	0.00 €	0.00 €
	TOTAL	0.00 €

Table 14: Hardware cost breakdown

Hardware	Monthly cost	Total cost
Personal computer	31.67 €	221.69 €
External monitor	5.00 €	35.00 €
	TOTAL	256.69 €

Table 15: Salary

Working hours	Hourly price	Total cost
1440	10.6 €	15264.00 €
	TOTAL	15264.00 €

Table 16: Total budget breakdown

Expense	Cost
Software cost	0.00 €
Hardware cost	256.69 €
Salary	15264.00 €
Electricity	270 €
TOTAL	15790.69 €

13 Environmental impact

The environmental impact that the development of this thesis has had is difficult to quantify. Consequently, determining the environmental footprint that this study has entailed is not an easy task and thus, some assumptions need to be considered in order to get an reasonable approximation. Given that all the thesis has been developed with a personal computer, it is clear that all the electricity consumed by this equipment has an important role in the environmental footprint that the present study has had. Nevertheless, quantifying its contribution is also cumbersome, as its origin could be a renewable energy source, such as wind power, hydropower, solar energy,..; or it could be a non-renewable energy sources, such as solid fuels. However, the data provided by the CNMC (Comisión Nacional de los Mercados y la Competencia) [31] can be used to estimate the amount of carbon dioxide and radioactive residues produced per $kW \cdot h$ of electricity consumed. According to this source, only 16.1% of the electricity produced during 2019 by "Endesa Generación" came from a renewable energy source. A 29.0% came from combined natural gas cycles, a 6.7% from carbon, a 3% from fuel/gas, and nearly a 29.4% of the electricity produced by the company came from nuclear energy. Therefore, it is estimated that about $0.27kg$ of CO_2 and $0.69mg$ of radioactive residues are produced per $kW \cdot h$ of electricity consumed. Therefore, assuming that about 1080 $kW \cdot h$ have been used throughout the duration of the present thesis, the following carbon dioxide and radioactive emissions can be estimated:

Table 17: CO_2 emissions and radioactive residues produced per $kW \cdot h$ of electricity and total amount of emissions

Emission type	**Emissions per $kW \cdot h$**	**Total emissions**
CO_2	0.27 kg	291.60 kg
Radioactive residues	0.69 mg	$7.45 \cdot 10^{-4} kg$
	TOTAL	291.60 kg

As it can be seen, the amount of radioactive residues are totally negligible. However, the amount of CO_2 is quite considerable, and equivalent to the carbon dioxide emissions produced, by an average car driving 2700 km, according to the data provided during NEDC cycles by the European Environmental Agency [32].

Finally, another important aspect to take into account, even though in a less important manner, is the amount of paper used for taking notes. During the development of the thesis, non-recycled paper has been used, which also implies an environmental impact due to its fabrication, packaging production and distribution. Nevertheless, it is considered that its contribution in the footprint is not relevant in comparison to the carbon dioxide emissions previously outlined and thus, it will not be considered.

References

[1] S. Mazumder, "Numerical methods for partial differential equations," Jan 2016. [Online]. Available: https://nanohub.org/resources/23427

[2] P. K. Kundu and I. M. Cohen, "Fluid mechanics," 2002.

[3] Wikipedia, the free encyclopedia, "Law of the wall," https://en.wikipedia.org/wiki/Law_of_the_wall, [Online] Accessed on July 2021.

[4] A. Leonard, W. van Rees, P. Koumoutsakos, and D. Pullin, "A comparison of vortex and pseudo-spectral methods for the simulation of periodic vortical flows at high reynolds numbers," *Journal of Computational Physics*, vol. 230, p. 2794–2805, 2011.

[5] R. D. Moser, J. Kim, and N. N. Mansour, "Direct numerical simulation of turbulent channel flow up to Re_τ= 590," *Physics of fluids*, vol. 11, no. 4, pp. 943–945, 1999.

[6] H. K. Versteeg and W. Malalasekera, *An introduction to computational fluid dynamics: the finite volume method*. Pearson education, 2007.

[7] G. de Vahl Davis and I. Jones, "Natural convection in a square cavity: a comparison exercise," *International Journal for numerical methods in fluids*, vol. 3, no. 3, pp. 227–248, 1983.

[8] Barcelona Supercomputing Center - Centro Nacional de Supercomputación, "Marenostrum," https://www.bsc.es/marenostrum/marenostrum, [Online] Accessed on June 2021.

[9] F. M. White and J. Majdalani, *Viscous fluid flow*. McGraw-Hill New York, 2006, vol. 3.

[10] Wikipedia, the free encyclopedia, "Prandtl number," https://en.wikipedia.org/wiki/Prandtl_number, [Online] Accessed on July 2021.

[11] Wikipedia, the free encyclopedia, "Péclet number," https://en.wikipedia.org/wiki/Péclet_number, [Online] Accessed on July 2021.

[12] Wikipedia, the free encyclopedia, "Grashof number," https://en.wikipedia.org/wiki/Grashof_number, [Online] Accessed on July 2021.

[13] Wikipedia, the free encyclopedia, "Nusselt number," https://en.wikipedia.org/wiki/Nusselt_number, [Online] Accessed on July 2021.

[14] F. Trias, O. Lehmkuhl, A. Oliva, C.-D. Pérez Segarra, and R. Verstappen, "Symmetry-preserving discretization of navier–stokes equations on collocated unstructured grids," *Journal of Computational Physics*, vol. 258, p. 246–267, 02 2014.

[15] R. Verstappen and A. Veldman, "Symmetry-preserving discretization of turbulent flow," *Journal of Computational Physics*, vol. 187, no. 1, pp. 343–368, 2003. [Online]. Available: https://www.sciencedirect.com/science/article/pii/S0021999103001268

[16] Centre Tecnològic de Transferència de Calor - CTTC, "Introduction to the fractional step method," 2015.

[17] Guilherme Caminha, "The cfl condition and how to choose your timestep size – Simscale." [Online]. Available: https://www.simscale.com/blog/2017/08/cfl-condition/

[18] A. Hadjidimos, "Successive overrelaxation (sor) and related methods," *Journal of Computational and Applied Mathematics*, vol. 123, no. 1, pp. 177–199, 2000, numerical Analysis 2000. Vol. III: Linear Algebra. [Online]. Available: https://www.sciencedirect.com/science/article/pii/S0377042700004039

[19] R. H. Refsnæs, "A brief introduction to the conjugate gradient method," 2009.

[20] M. Anjum, "One-minute derivation of the conjugate gradient algorithm," 08 2016.

[21] S. B. Pope, "Turbulent flows," 2001.

[22] J. Tu, G. H. Yeoh, and C. Liu, *Computational fluid dynamics: a practical approach*. Butterworth-Heinemann, 2018.

[23] E. Houghton and P. Carpenter, *Aerodynamics for Engineering Students*. Elsevier Science, 2003. [Online]. Available: https://books.google.es/books?id=4YCThwzeTBQC

[24] P. Sagaut, *Large eddy simulation for incompressible flows: an introduction*. Springer Science & Business Media, 2006.

[25] Centre Tecnològic de Transferència de Calor - CTTC, "Large-eddy simulation of turbulent incompressible flows," 2015.

[26] F. Trias, D. Folch, A. Gorobets, and A. Oliva, "Building proper invariants for eddy-viscosity subgrid-scale models," *Physics of Fluids*, vol. 27, p. 065103, 06 2015.

[27] J. Luque, "Numerical study of the Navier-Stokes equations using the Fractional Step Method. Application to the laminar flow around a square cylinder," Bachelor's Thesis, 06 2019.

[28] J. DeBonis, "Solutions of the taylor-green vortex problem using high-resolution explicit finite difference methods," 01 2013.

[29] Tusalario.es, "Compara tu salario." [Online]. Available: https://tusalario.es/salario/comparatusalario?job-id=2141010000000#

[30] Mathworks, "Pricing and licensing." [Online]. Available: https://es.mathworks.com/pricing-licensing.html?prodcode=ML&intendeduse=edu

[31] CNMC - Comisión Nacional de los Mercados y la Competencia, "Listado de informes de etiquetado de electricidad." [Online]. Available: https://gdo.cnmc.es/CNE/resumenGdo.do?anio=2019

[32] European Environmental Agency, "CO_2 emissions from new passenger cars." [Online]. Available: http://co2cars.apps.eea.europa.eu/

[33] Wikipedia, the free encyclopedia, "Navier-Stokes Equations," https://en.wikipedia.org/wiki/Navier-Stokes_equations, [Online] Accessed on June 2021.